FORMATION RATE OF NATURAL GAS HYDRATE

Reactor Experiments and Models

Marit Mork

A thesis submitted in partial fulfillment
of the requirements for the
degree of Doktor Ingeniør of the
Norwegian University of Science and Technology
Deparment of Petroleum Engineering and Applied Geophysics

July 2002

URN:NBN:no-3342

URN:NBN:no-3342

Abstract

The rate of methane hydrate and natural gas hydrate formation was measured in a 9.5 litre stirred tank reactor of standard design. The experiments were performed to better understand the performance and scale-up of a reactor for continuous production of natural gas hydrates. The hydrate formation rate was measured at steady-state conditions at pressures between 70 and 90 bar and temperatures between 7 and 15 °C. Between 44 and 56 % of the gas continuously supplied to the reactor was converted to hydrate.

The experimental results show that the rate of hydrate formation is strongly influenced by gas injection rate and pressure. The effect of stirring rate is less significant, and subcooling has no observable effect on the formation rate. Hydrate crystal concentration and gas composition do not influence the hydrate formation rate. Observations of produced hydrate crystals indicate that the crystals are elongated, about 5 μm in diameter and 10 μm long. Analysis of the results shows that the rate of hydrate formation is dominated by gas-liquid mass transfer.

A mass transfer model, the bubble-to-crystal model, was developed for the hydrate formation rate in a continuous stirred tank reactor, given in terms of concentration driving force and an overall mass transfer coefficient. The driving force is the difference between the gas concentration at the gas-liquid interface and at the hydrate crystal surface. These concentrations correspond to the solubility of gas in water at experimental temperature and pressure and the solubility of gas at hydrate equilibrium temperature and experimental pressure, respectively. The overall mass transfer coefficient is expressed in terms of superficial gas velocity and impeller power consumption, parameters commonly used in studies of stirred tank reactors.

Experiments and modeling show that the stirred tank reactor has a considerable potential for increased production capacity. However, at higher hydrate production rates the capacity will be limited by heat transfer in the reactor. For a higher production capacity and in scale-up of the hydrate production process, the upstream gas supply system and the downstream separator must be increased in proportion to the reactor capacity.

URN:NBN:no-3342

Acknowledgements

First of all, I would like to thank Professor Jon Steinar Gudmundsson for being my supervisor and for giving me the opportunity to study for the Dr.Ing. degree. Your guidance and suggestions and the fruitful discussions have been invaluable to me throughout.

The financial support from the Research Council of Norway through the Natural Gas programme, project 125482/212, is highly appreciated.

Special thanks go to Dr.Ing. Vibeke Andersson for showing me how to operate the NTNU hydrate laboratory, and to Dr.Ing. Odd Ivar Levik and Professor Mahmut Parlaktuna for helping me solving technical problems in the laboratory.

The technical staff at the Department of Petroleum Engineering and Applied Geophysics have been indispensable in maintenance and repair of the laboratory. Furthermore, I am grateful to the departmental office staff for being very kind and helpful.

I thank Professor Jean-Pierre Monfort (Institut National Polytechnique in Toulouse), Dr. Carl B. Argo (BP Exploration) and Professor Didrik Malthe-Sørensen (NTNU) for serving on my Dr.Ing. committee.

Thanks are due to Professor Hugo A. Jakobsen and Professor Arne Grislingås at the Department of Chemical Engineering for discussions about stirred tank reactors.

Thanks to André, Lill-Tove, Bengt, Øyvind, Janet, Alf, Therese and other fellow students for making my time as a Dr.Ing. student a very pleasant one.

Finally, to my very best friend Åsmund, thank you for all your support and encouragement.

URN:NBN:no-3342

Contents

URN:NBN:no-3342

URN:NBN:no-3342

List of tables

URN:NBN:no-3342

URN:NBN:no-3342

List of figures

URN:NBN:no-3342

Nomenclature

Roman letters

A	constant ($cm^3 cm^{-2} min^{-1} bar^{-1}$), constant ($J\ mol^{-1}$)
$A_{(g\text{-}l)}$	gas-liquid interfacial area (m^2)
A_R	reactor cross sectional area (m^2)
a	gas-liquid interfacial area per unit liquid volume ($m^2\ m^{-3}$)
a_c	hydrate crystal surface area per unit liquid volume ($m^2\ m^{-3}$)
a_s	gas-liquid interfacial area (cm^2)
a_p	particle surface area (m^2)
B	baffle width (m)
B_I	primary nucleation rate (number of nuclei $m^{-3}s^{-1}$)
b, b_1, b_2, b_3	constants (-)
C	clearance between impeller and bottom of reactor (m)
C_b	gas concentration in liquid bulk ($mol\ m^{-3}$)
C_{eq}	gas concentration at hydrate crystal surface given by gas solubility at experimental pressure and equilibrium temperature ($mol\ m^{-3}$)
C_i	gas concentration at liquid-crystal interface ($mol\ m^{-3}$)
C_{int}	gas concentration at gas-liquid interface ($mol\ m^{-3}$)
C_{sol}	gas concentration at gas-liquid interface given by gas solubility at experimental pressure and temperature ($mol\ m^{-3}$)
C_{w0}	initial concentration of water molecules ($mol\ m^{-3}$)
c	correction factor (-)
c_p	specific heat capacity ($J\ mol^{-1}K^{-1}$)
D	impeller diameter (m)
D_L	gas diffusivity (m^2s^{-1})
d	constant (-)
E	constant ($J\ mol^{-1}$)
E_i	energy of component *i* ($J\ mol^{-1}$)
E_{sys}	total energy of system (J)
F_i	molar flow rate of component *i* out of reactor ($mol\ s^{-1}$)
F_{i0}	molar flow rate of component *i* into reactor ($mol\ s^{-1}$)
Fr	impeller Froude number $\frac{N^2D}{g}$
f, f_i	gas fugacity (MPa), (bar)
f_{eq}	equilibrium fugacity at experimental temperature (MPa)

f_g^V	gas phase fugacity (MPa)
G	crystal growth rate (m s^{-1})
g	acceleration of gravity (m s^{-2})
g_c	graviational constant (-)
H	Henry's law constant (bar)
H_i	enthalpy of component *i* out of reactor (J mol^{-1})
H_{i0}	enthalpy of component *i* into reactor (J mol^{-1})
H_R	liquid height (m)
h	convective heat transfer coefficient (W $K^{-1}m^{-2}$)
J_p	nucleation rate (mol s^{-1})
K^*	rate constant (mol m^{-2} $MPa^{-1}s^{-1}$) in Equation 2.2
K, K_1	constants
k	rate constant in empirical model ($m^{3-\alpha}s^{\alpha-1}bar^{-1}W^{-\beta}$) in Equation 7.4
k_1	nucleation rate constant in Equation 2.10
k_d	mass transfer coefficient around hydrate particle (mol m^{-2} $MPa^{-1}s^{-1}$)
k_g	growth rate constant (cm^4 $mol^{-1}s^{-1}$)
k_L	liquid side gas-liquid mass transfer coefficient (m s^{-1})
k_La	volumetric gas-liquid mass transfer coefficient (s^{-1})
k_{p0}	constant in Equation 2.5
k_R	rate constant for surface integration (m s^{-1})
k_r	"reaction" rate constant (mol m^{-2} $MPa^{-1}s^{-1}$)
k_S	liquid-solid mass transfer coefficient (m s^{-1})
L	hydrate crystal size (m)
M, M_g	molar mass of gas (kg mol^{-1})
M_{H_2O}	molar mass of water (0.01802 kg mol^{-1})
m, m'	exponents (-)
m_b	mass of gas bottle (kg)
m_g	mass of gas in gas bottle (kg)
N	stirring rate (s^{-1})
N_p	impeller power number (-)
N_Q	impeller flow number (-)
N_{QG}	impeller gas flow number $\frac{Q_G}{ND^3}$
$N_{QG,F}$	gas flow number at transition from flooded to loaded flow condition
$N_{QG,CD}$	gas flow number at transition from loaded to complete dispersion
$N_{QG,R}$	gas flow number at transition from complete disp. to recirculation
N_{Re}	impeller Reynolds number $\frac{\rho ND^2}{\mu}$
n, n_i	amount of gas (mol)

n_{diff}	amount of gas leaving gas bottle in a time interval (mol)
n_h	hydration number (-)
n_{hyd}	amount of hydrate (mol)
$n_{i,vent}$	number of sampled gas vent rate measurements (-)
$\left(\frac{dn}{dt}\right)_p$	growth rate per particle (mol s^{-1})
P	impeller power consumption (W)
P_g	gassed power consumption, power cons. in gas-liquid reactor (W)
P_o	additional power consumption (W)
p	pressure (bar)
p_{nc}	pressure at normal conditions (1 atm)
Q	pumping capacity of impeller (m^3s^{-1})
Q_{cons}	gas consumption rate (Nl min^{-1})
Q_G	volumetric gas flow rate (m^3s^{-1})
Q_{inj}	gas injection rate (Nl min^{-1})
Q_{meas}	measured gas vent rate without correction factor (Nl min^{-1})
Q_{vent}	gas vent rate (Nl min^{-1})
$\dot{Q}$	heat flow (W)
q	gas consumption rate in empirical model (m^3s^{-1})
q_{Vys}	gas consumption rate in Vysniauskas & Bishnoi model (cm^3 min^{-1})
R	gas constant (8.314 J $mol^{-1}K^{-1}$)
R_{G-L}	maximum gas-liquid mass transfer rate (mol s^{-1})
R_{Mon}	gas consumption rate in Monfort *et al.* model (mol min^{-1})
R_{tot}	overall mass transfer rate (mol s^{-1})
r	gas absorption rate (mol $m^{-3}s^{-1}$)
r_{hyd}	hydrate formation rate (mol $m^{-3}s^{-1}$)
$r_y(t)$	global formation rate in Englezos *et al.* model (mol $m^{-3}s^{-1}$)
r_1, r_2, r_3	mass transfer rates (mol $m^{-3}s^{-1}$)
$(-r_i)_{out}$	rate of reaction of component i at outlet conditions (mol $s^{-1}m^{-3}$)
r_p	radius of spherical particle (m)
S	supersaturation (-)
s	slope in Clausius-Clapeyron plot (K)
$s_{Q_{vent}}$	standard deviation of averaged gas vent rate (Nl min^{-1})
s_{vent}	mean standard deviation of averaged gas vent rate (Nl min^{-1})
T	temperature (K)
T_b	liquid bulk temperature (K)
T_{eq}	temperature at hydrate crystal surface (K)
T_{exp}	experimental temperature (°C), (K)

T_g	gas temperature (K)
T_i	temperature at solid-liquid interface (K)
T_{nc}	temperature at normal conditions (0 °C)
T_R	tank diameter (m)
T_{sol}	temperature at gas-liquid interface (K)
t	time (s)
u	liquid velocity (m s^{-1})
V	reactor volume (m^3)
V_b	gas bottle volume (m^3)
$\bar{V}$	linear growth rate (µm s^{-1})
V_G	total volume of gas in reactor (m^3)
V_L	total volume of liquid in reactor (m^3)
V_{nc}	gas volume at normal conditions (m^3) (1 atm, 0 °C)
v_{sg}	superficial gas velocity (m s^{-1})
W	impeller blade width (m)
$\dot{W}$	work (W)
$\dot{W}_s$	shaft work (W)
X	conversion of gas (-)
x, x_i	mole fraction solubility (-)
x_b	mole fraction of gas in bulk water phase (-)
x_{int}	mole fraction of gas in water at gas-liquid interface (-)
$x_{mixture}$	weighted mole fraction solubility of gas mixture (-)
y_i	mole fraction of component *i* in gas phase (-)
z	gas compressibility factor (-)

Greek letters

ΔE_a	activation energy (kJ mol^{-1})
Δf	fugacity driving force (bar)
ΔH, ΔH_{Rx}	heat/enthalpy of formation (J mol^{-1})
ΔH_{diss}	enthalpy of dissociation (J mol^{-1})
ΔT	subcooling (K), (°C)
α	constant (-), (K^{β}), exponent (-)
β	exponent (-)
γ	constant (-)
δ	constant in Equation 8.10
ε_a	absolute error

ε_G	gas holdup (-)
ϕ_i	fugacity coefficient of component *i* (-)
λ	exponent (-)
μ	viscosity (Pa s)
μ_L	liquid viscosity (Pa s)
μ_{Sl}	viscosity of homogeneous slurry (Pa s)
μ_2	second moment of particle size distribution (m^2 m^{-3})
ω	stirring rate (min^{-1})
ρ	density (kg m^{-3})
ρ_{H_2O}	density of water (kg m^{-3})
θ_c	circulation time (s)
θ_m	mixing time (s)
σ	surface tension (Pa m)

Abbreviations

BPR	Back Pressure Regulator
CSTR	Continuous Stirred Tank Reactor
g	gas
h	hydrate
MSMPR	Mixed-Suspension Mixed-Product Removal
NGH	Natural Gas Hydrate
Nl	Normal litre (1 atm, 0 °C)
NTNU	Norwegian University of Science and Technology
NTP	Normal Temperature and Pressure (1 atm, 0 °C)
PVT	Pressure-Volume-Temperature
RPM	Revolutions Per Minute
Sm^3	Standard Cubic Meters (1 atm, 15 °C)
sI	structure I hydrate
sII	structure II hydrate
sH	structure H hydrate
THF	TetraHydroFuran
w	water
Å	Ångstrøm (1 Å = 10^{-10} m)

1

Introduction

In the petroleum industry, safe and cost-effective ways of transporting produced oil and gas are required. Natural gas hydrates can be used to transport natural gas in bulk carriers and mixed with an oil phase in pipelines. To make that possible, reactors providing efficient and continuous production of natural gas hydrates are needed. The hydrate formation process is complex, involving gas, liquid and solid at low temperature. Hence, experimental data and modeling are required in design of a reactor system that will be suitable for the production of hydrates in land-based and offshore-based processes.

1.1 Background

Natural gas hydrate (NGH) technology for the storage and transport of natural gas is currently under development at the Norwegian University of Science and Technology (NTNU). A lot of the remaining oil and gas reserves world-wide are medium to small in size. To develop such marginal reserves in the future, cost-effective methods for gas transport to the market will be required. NGH technology is found especially suitable for handling associated gas in offshore oil production and for bulk transport of natural gas from remotely located small and medium sized gas fields (Gudmundsson *et al.*, 1998, Gudmundsson *et al.*, 1999).

The NGH technology includes production, transport and regasification of natural gas hydrates. The production process is based on standard reactors, pumps,

URN:NBN:no-3342

separators and heat exchangers. The formation of hydrates in reactors is the subject of this doctoral work. Gudmundsson and Børrehaug (1996) found that the hydrate production process is technically feasible, and suggested a process where natural gas and water are contacted in stirred tank reactors at typically 65 bar and 10 °C.

Natural gas hydrate contains up to 182 standard volumes of gas per volume of hydrate. Gudmundsson, Parlaktuna and Khokhar (1992, 1994) concluded that produced hydrates can be transported and stored at atmospheric pressure and temperatures below 0 °C, typically at -15 °C, without significant loss of gas. The storage capacity and the stability of hydrates at atmospheric pressure, make NGH technology a safe and economic method for handling natural gas. The development of NGH technology at NTNU stems from Norwegian Patent 172080 where the stability of frozen hydrates was proposed for cost-effective storage and transport of natural gas (Gudmundsson, 1990).

Two concepts, the dry hydrate concept and the hydrate slurry concept, are being developed at NTNU. In the dry hydrate concept, natural gas hydrates are produced in stirred tank reactors with water. After being produced, the hydrates are separated from the water, and simultaneously frozen and depressurized to low temperature and atmospheric pressure. Hydrate crystals are then available for transport by bulk carriers to the market. In the hydrate slurry concept, the gas hydrates are first produced in a water continuous phase and then in an oil continuous phase. The final product is a hydrate-oil slurry with no free water, pumpable in pipelines to shore or transportable in shuttle tankers (Gudmundsson *et al.*, 1998). In both concepts, gas hydrates are produced by contacting water with natural gas in a chain of stirred tank reactors.

1.2 Scope of work

Research has been on-going at NTNU since 1990 to answer fundamental questions in the development of NGH technology. A natural gas hydrate laboratory was built for studying the production of hydrates, as well as for the determination of rheological properties of hydrate slurries and physical properties of hydrates. A 9.5 litre stirred tank reactor of standard design with gas and liquid inlets and outlets was chosen for the production process. The NTNU hydrate laboratory has been used in the experimental work.

Natural gas hydrates have not yet been produced commercially, and there exists limited experience in operating a hydrate reactor. The hydrate formation process has some special features. A hydrate reactor is a three-phase slurry reactor as the production involves gas, water, and solid hydrates. Natural gas hydrate floats because water is slightly denser than the hydrate. The kinetics of hydrate formation is poorly understood, and mass and heat transfer effects are believed to be important for the overall rate of hydrate formation. Most of the reported studies of hydrate formation have been carried out in small scale batch or semi-batch reactors and not in continuous stirred tank reactors (CSTRs) as needed in a commercial process. Models based on reported reactor experiments seem to be system specific. On the other hand, operation of stirred tank reactors in general is extensively described in the literature, and by studying the hydrate formation process in this type of reactor, established knowledge can provide valuable information in understanding the process.

Hydrate formation is an exothermic process. By producing in a water continuous system such as a stirred tank reactor, the water phase acts as a heat sink for the heat of hydrate formation, so that the temperature in the reactor can be controlled. The upper temperature in hydrate production is restricted by the equilibrium temperature for the existence of hydrates.

The primary objective of this work is to obtain a better understanding of the processes occurring during hydrate formation in a continuous stirred tank reactor. Such knowledge is necessary for efficient operation of a hydrate production process and for design of commercial reactors, initially for the scale-up from laboratory to pilot plant size. The hydrate production rate will determine the size and thereby the costs of the reactor equipment. Therefore, the experimental work was concentrated around measuring the rate of hydrate formation under different experimental conditions, and identifying which experimental parameters that are most important for the formation rate. An investigation of the hydrate crystal size and morphology was also included in the experimental study of the reactor performance.

The experimental work benefited from the work by Parlaktuna and Gudmundsson (1998a, 1998b), who carried out systematic measurements of the rate of hydrate formation in the NTNU laboratory. One of the aims of the present experimental work was to carry out experiments at conditions closer to the conditions in industrial stirred tank reactors, which included increasing the hydrate formation rate.

An important issue in studying the hydrate reactor was to correlate experimental parameters to common parameters used for describing the performance of standard stirred tank reactors. Experimental results and the results of Parlaktuna and Gudmundsson (1998a, 1998b) were to be modeled using such typical parameters. A model can be used to investigate the performance of the reactor, and the development of a model gives a method for analyzing experimental results from a large scale reactor.

1.3 Organization of thesis

A literature survey in Chapter 2 presents studies of the rate of hydrate formation and formation mechanisms. The survey focuses on the macroscopic studies of hydrate formation in stirred systems. In Chapter 3, relevant theory and literature on stirred tank reactors with focus on gas-liquid systems, liquid-solid systems and gas-liquid-solid systems are presented.

The NTNU hydrate laboratory, the experimental procedures and the method for analyzing the experimental results are described in Chapter 4. The experimental conditions and the experimental results are presented in Chapter 5. Some of the results of Parlaktuna and Gudmundsson (1998a, 1998b) are included in a separate section because they were used in subsequent modeling. A study of the hydrate crystal size and morphology was independent of the other experiments, and the topic is therefore treated separately in Chapter 6.

An empirical model and a mass transfer model were developed based on the present experimental results and the results of Parlaktuna and Gudmundsson. The empirical model is presented in Chapter 7. The relative importance of the different experimental parameters is identified. In Chapter 8, the mass transfer model is presented and compared with literature data.

Based on the experimental results and the two models, the dominating effects in the process are discussed in Chapter 9. Operation of the reactor with respect to mass transfer is discussed. An energy balance presented in Appendix D is discussed in relation to the findings from the experimental results and the models. The implications of the results on scale-up of the reactor are considered. Finally, conclusions are presented and further work suggested.

Appendix A presents the results of each experiment. Appendix B describes the calculation of the overall error in the hydrate formation rate. Appendix C describes the calculation of the solubility of gas in water, which is used in the mass transfer model in Chapter 8. Mass and energy balances for the reactor provide tools for simulation of the reactor performance and are presented in Appendix D.

A list of the articles and reports written during the doctoral period is provided in Appendix E. Four articles are concerned with reactor specific topics, such as results from reactor experiments, mass transfer model, empirical model and experimental results related to hydrate formation in subsea pipelines. Topics related to the NGH technology in general have been published in four articles, including process design, cost-estimates of the hydrate slurry concept and comparison with other technologies. Two literature studies have been written, one about stirred tank reactors and one about hydrate nucleation and growth. For the hydrate slurry concept, a report about properties of crude oil at low temperatures has been written.

2

Review of gas hydrate formation

Researchers have usually studied the hydrate formation process to better understand the performance of kinetic inhibitors. However more recently, hydrate formation has been in focus in the production of hydrates for storage and transport of natural gas, gas separation, exploitation of gas hydrate deposits and depositing of CO_2 hydrates on the sea floor. The increasing number of published articles on hydrate formation in the four consecutive international gas hydrate conferences (Sloan, Happel and Hnatow, 1994, Monfort, 1996, Holder and Bishnoi, 2000, Mori, 2002) illustrates the large interest in hydrate formation issues.

This chapter is intended to give a review of hydrate formation studies with emphasis on the rate of gas hydrate formation in water continuous systems under stirred conditions. With some exceptions, the review is limited to systems where the hydrate forming components are hydrocarbons. The macroscopic studies of hydrate formation, which are most relevant to the present work, are stressed.

The two first sections give an introduction to the microscopic structures of gas hydrates and to the thermodynamic conditions where hydrates may form. The fundamental mechanisms of hydrate formation are reviewed in Section 2.3. The driving force for hydrate formation is discussed in Section 2.4. Experimental studies of the rate of methane, ethane and propane hydrate formation are presented

URN:NBN:no-3342

in Section 2.5. Some experimental results are compared in Section 2.6. Studies of hydrate crystal size are reviewed in Section 2.7. Many of the experimental studies have resulted in mechanistic models and correlations, which are reviewed in Section 2.8.

In most studies, results on hydrate formation rates are reported for a pure water phase or a water phase with an additive for hydrate inhibition. Recently, some researchers have focused on promoting the formation process by accelerating the formation rate. This topic is reviewed in Section 2.9. Along with the development of hydrate technologies for storage and transport of natural gas, gas separation and depositing of CO_2-hydrates, different methods for hydrate production are being developed. They are briefly reviewed in Section 2.10.

2.1 Hydrate structures

Gas hydrates are crystalline solids. They are more properly called clathrate hydrates to distinguish them from stoichiometric hydrates found in inorganic chemistry. The crystalline structure is composed of polyhedra of hydrogen-bonded water molecules. The polyhedra form cages that contain at most one guest molecule each. The cages are stabilized by van der Waals forces between the water molecules and the enclatherated guest molecule. In extraordinary situations, two guest molecules may enter the same cage (Sloan, 1998).

Only a few kinds of cages may form depending on the size of the guest molecule. These cages arrange into different hydrate structures known as structure I (sI), structure II (sII) and structure H (sH) (Sloan, 1998). Recently, Udachin and Ripmeester (1999) discovered a new and complex hydrate structure consisting of alternating stacks of sH and sII. Methane gas forms sI hydrates, while natural gas usually forms sII hydrates. sI and sII hydrates will be discussed further.

sI consists of two different cages. In a unit cell, 2 small and 6 large cages appear. The small cage, the pentagonal dodecahedron labeled 5^{12}, has 12 pentagonal faces with equal edge lengths and equal angles. The large cage, the tetrakaidecahedron, is called $5^{12}6^{2}$ because it has 12 pentagonal and 2 hexagonal faces. One sI unit cell has 46 water molecules and fits into a 12 Å cube. sII consists of 16 small cages and

8 large cages. Also, sII has the pentagonal dodecahedron (5^{12}) as the small cage. The large cage, the hexakaidecahedron, has 12 pentagonal and 4 hexagonal faces and is therefore labeled $5^{12}6^{4}$. One sII unit cell has 136 water molecules and fits into a 17.3 Å cube (Sloan, 1998).

Generally, molecules between 3.8 Å and 6.5 Å in diameter can form sI and sII hydrates if they do not contain hydrogen bonding group(s). Depending on the size of the guest molecules, only the large cages of each structure can be occupied or both types of cages can be occupied. The small cages are never occupied alone as this is not enough to stabilize either sI or sII. However, if the small cages can be filled, the molecule will also enter the large cages as a simple hydrate species. Simple hydrates are hydrates with only one guest species (Sloan, 1998).

The large cages in sI ($5^{12}6^{2}$) are large enough to contain molecules up to 6.0 Å in diameter, in which only ethane and carbon dioxide of the natural gas components stabilize as simple hydrates. The large cages in sII can contain molecules as large as 6.6 Å. This means that propane and iso-butane will stabilize the large cages, but leave the small cages of sII vacant. Alternatively, the small cages are filled with methane, which means that natural gas with propane or iso-butane typically forms sII hydrates. Methane will form sI hydrate by filling both the large and the small cages, but not sII because the molecules are too small to stabilize the large cages in sII.

Based on the knowledge about the hydrate structure for a given gas composition, it is possible to calculate the relative water/guest ratio known as the ideal hydration number. Pure methane will occupy the 2 small and the 6 large cages of sI. With 46 water molecules in a unit cell, the ideal hydration number becomes 5.75. For an natural gas mixture of methane, ethane and propane, where propane and ethane stabilize the 8 large cages of sII, methane enter the 16 small cages, and the unit cell has 136 water molecules, the ideal hydration number becomes 5.67.

If all the cages of sII had been filled, each volume of hydrate would have contained 182 standard volumes of gas (1 atm, 15 °C). In reality however, it is impossible to obtain a perfect crystal where all the cages are filled, which means that the real hydration number is higher than the ideal hydration number. The degree of filling depends on the system conditions. This variation in filling degree demonstrates why hydrates are non-stoichiometric clathrate compounds.

2.2 Hydrate equilibrium conditions

At hydrate equilibrium conditions, solid hydrate may exist in equilibrium with liquid water or ice, gas and some additive. Such temperature and pressure conditions are defined by the hydrate equilibrium curve for a given gas and water composition. Hydrates can only form at temperatures lower than the equilibrium temperature and simultaneously at pressures higher than the equilibrium pressure. The distance from the equilibrium conditions is the driving force for hydrate formation (discussed in Section 2.4). Hence, the hydrate equilibrium curve represents the pressure and temperature conditions where the hydrates dissociate. The hydrate equilibrium curves for methane and a natural gas mixture (92 % methane, 5 % ethane and 3 % propane) are shown in Figure 5.5. In the present experiments, methane and this natural gas mixture were used.

Hydrate equilibrium curves can be predicted from statistical thermodynamics using the van der Waals and Platteeuw model with some modifications, which is thoroughly explained by Sloan (1998). Also, other simpler methods based on hand calculation and phase diagrams exist (Sloan, 1998). Available computer programs based on statistical thermodynamic models, such as CSMhyd (1998) or PVTsim (2001) can predict hydrate equilibrium conditions.

The hydrate equilibrium temperature at 1 atm is -73 °C for methane gas and -36 °C for natural gas mixture (PVTsim, 2001). At these temperatures, hydrates are thermodynamically stable. On the other hand, Gudmundsson, Parlaktuna and Khokhar (1992) observed that the natural gas concentration in hydrate samples remained almost unchanged when stored at atmospheric pressure and at -18 °C for periods of 10 days. This behavior was explained by the formation of an ice layer around the hydrate crystals. The self-preserving effect is utilized in the NGH process for atmospheric and adiabatic storage of natural gas hydrates.

2.3 Mechanisms of gas hydrate formation

The thermodynamic behaviour of hydrate systems forms the basis for understanding the mechanisms of hydrate formation. The time-dependent phenomenon of hydrate formation kinetics is described by applying crystallization theories including nucleation, growth, agglomeration and breakage. So far, the most studied phenomena of gas hydrate formation are the nucleation and growth processes.

Nucleation is a microscopic stochastic phenomenon where gas-water clusters (nuclei) grow and disperse until some nuclei have grown to a critical size. Nucleation may occur spontaneously (homogeneous nucleation), or it may be induced around impurities (heterogeneous nucleation). In contrast to primary nucleation, where nucleation commences without crystals present, secondary nucleation occurs in the vicinity of already growing crystals in the system.

The time from the first gas-liquid contact to the first detection of a hydrate phase is called the induction time. In macroscopic studies, the induction time has been used as a measure of the nucleation period (Skovborg *et al.*, 1993, Monfort and Nzihou, 1993, Yousif, 1994, Natarajan, Bishnoi and Kalogerakis, 1994). These studies indicate that the induction time increases dramatically when the driving force for hydrate formation (Section 2.4) approaches zero.

In 1991, Sloan and Fleyfel presented a molecular mechanism for gas hydrate nucleation from ice. The mechanism is based on observations of methane and krypton hydrate formation from ice, where induction times were clearly observed, and ethane hydrate formation, where no induction time was observed. Sloan and Fleyfel suggested that on an ice surface, free water molecules rearrange around a guest molecule to form an unstable 5^{12} cage. Methane and krypton molecules, which enter this cage, oscillate between the 5^{12} cages of sI and sII before the cages reach a stable nuclei size. Ethane does not experience the induction time because ethane stabilizes the large cages of sI, and hence, ethane does not induce oscillation between the small cages. Yousif (1994) argued that hydrate formation always starts by stabilizing the large cages of sI and sII regardless of the size of the guest molecule.

Christiansen and Sloan (1994) extended the mechanism of Sloan and Fleyfel (1991) to explain hydrate formation in liquid water. They suggested four stages: molecular species, labile clusters, metastable agglomerates and stable nuclei. As gas dissolves in water, hydrogen-bonded water molecules gather around the apolar guest molecule to form labile clusters. Depending on the guest size, the number of water molecules in each cluster, defined by a coordination number, varies. Because the guest molecules inside the clusters are attracted to each other, the labile clusters agglomerate. However, two different coordination numbers of each hydrate structure are required to form agglomerates, or else the nucleation is inhibited until the clusters transform to fulfill the coordination number requirement. The agglomerates are in quasi equilibrium with each other and other labile clusters until they exceed the critical size for stable nuclei. Stable growth begins.

In contrast to Christiansen and Sloan (1994), who assumed hydrate nucleation in the liquid water phase, Rodger (1990) developed a model based on nucleation at a surface. Rodger suggested that the hydrate forming molecules are adsorbed on a water or ice surface and condensed water molecules orient around the guest molecules to form cages. Some cages may rearrange to form liquid water and free guest molecules, others may grow to eventually form stable nuclei.

Kvamme (1994) critically reviewed the mechanisms of Christiansen and Sloan (1994) and Rodger (1990). He stated that the main difference is that Christiansen and Sloan relate nucleation to the liquid phase or at least the liquid side of the gas-liquid interface, while Rodger relates it to the gas side of the gas-liquid interface. Kvamme noted that the mechanism of Christiansen and Sloan contained no element of randomness or probability. Considering the mechanism of Rodger, non-hydrate formers may adsorb on the surface and cause inhomogeneous hydrate-forming properties of the surface. This introduces an element of probability that can explain observed variety of induction times in parallel experiments.

In 1996, Kvamme proposed a new hydrate formation theory based on the hypothesis that initial hydrate formation takes place at the gas-liquid interface towards the gas side (Rodger, 1990). The theory was modeled and compared to experimental data. Kvamme (2000) published a revised version of the model where evaluation of cluster distribution and cluster stability analysis are included. An extended diffusive interface theory models the growth rates of the metastable clusters. Comparison of modeled growth rates towards the gas side and towards the liquid side of the gas-liquid interface indicates that the gas side growth rates are two orders of magnitude higher than the liquid side growth rates (Kvamme, 2002).

Mechanisms to describe growth have received less attention. Sloan (1998) considered growth to be a combination of mass transfer of components to the growing surface and growth at the hydrate surface. He suggested a hypothesis adopted from

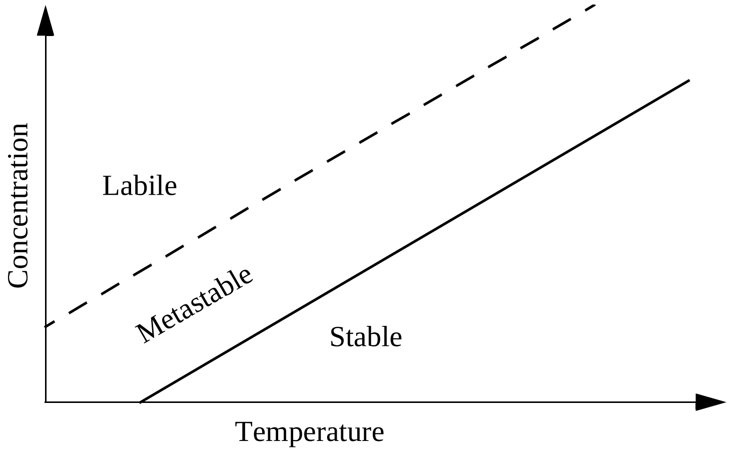

Figure 2.1 A generalized solubility-supersolubility diagram after Mullin (1993). The continuous line is the solubility curve and the broken line is the supersolubility curve.

classical crystallization including adsorption of the cluster at the hydrate surface, diffusion over the surface and integration of the cluster into a kink.

2.4 Driving forces for gas hydrate formation

Mullin (1993) defines the driving force for crystallization in terms of supersaturation. Spontaneous (homogeneous) nucleation will only occur in a supersaturated solution in the labile zone limited by the supersolubility curve (Figure 2.1). In the metastable zone, spontaneous nucleation cannot occur, but growth of crystals is possible. For instance, the driving force for nucleation and growth can be defined by the supersaturation ratio: the concentration of the supersaturated solution to the equilibrium concentration at the solubility curve, both at the same temperature.

Sloan (1998) suggested an analogy to hydrate formation where concentration is replaced by the logarithmic pressure giving the hydrate equilibrium curve. A corresponding supersolubility curve has not yet been defined in hydrate kinetic studies. Several driving forces have been used in modeling of hydrate formation kinetics, and those most frequently used in experimental studies are related to the hydrate equilibrium curve.

Vysniauskas and Bishnoi (1983, 1985) used subcooling (sometimes also called supercooling) as the driving force for nucleation and growth. Subcooling is defined as the difference between the hydrate equilibrium temperature at the experimental pressure and the experimental temperature. Subcooling is easily determined by measuring the experimental temperature and calculating the hydrate equilibrium temperature using a thermodynamic model.

Alternatively, the distance from the hydrate equilibrium curve in terms of pressure or fugacity can be used. Englezos *et al.* (1987a) used the difference in fugacity of the dissolved gas and the hydrate equilibrium fugacity at the experimental temperature as the driving force in their hydrate formation model. Similarly, Natarajan, Bishnoi and Kalogerakis (1994) used $f_g^V/f_{eq} - 1$, where f_g^V is the gas phase fugacity, as driving force for nucleation.

Sloan (1998) pointed out that a pressure or fugacity difference as a driving force does not represent physical reality. If there is no net force working on the system, the pressure everywhere in the system must be equal. In multi-phase systems, pressure equilibrium times are orders of magnitude shorter than thermal equilibrium times. Moreover, the temperature at the hydrate surface must be higher than the experimental temperature as heat is released upon hydrate formation. Therefore, subcooling is a better driving force (Sloan, 1998).

Skovborg and Rasmussen (1994) used the difference in gas mole fraction at the gas-liquid interface and in the liquid bulk phase as the driving force. They maintain that the formation rate is controlled by gas-liquid mass transfer rather than crystal growth, and therefore, the driving force is not related to the hydrate equilibrium curve or the hydrate crystal surface. In their study of induction times, Skovborg *et al.* (1993) expressed the driving force as the difference in the chemical potential of water in the hydrate phase and water in the liquid phase at the experimental pressure and temperature.

Similarly, Herri *et al.* (1999) expressed the driving force for gas dissolution in water as the difference in the gas concentration at the gas-liquid interface and in the liquid bulk. For growth of the hydrate crystals, the driving force is the difference in bulk concentration and gas concentration in the presence of a hydrate phase.

The driving force for hydrate formation depends on the gas concentration in the liquid (Skovborg and Rasmussen, 1994, Herri *et al.*, 1999). As shown in Figure 2.1, the gas concentration at the solubility curve, that is, the solubility of gas in water, determines the driving force. The solubility of methane, ethane and propane in water is used to calculate the driving force in the present model, and therefore, the solubility of these components is reviewed in Section 8.2.

2.5 Rate of gas hydrate formation

Several researchers have measured the rate of hydrate formation after nucleation, that is, the hydrate growth stage. The rate of formation is typically expressed in terms of gas consumption rate. Studies performed under stirred conditions in liquid water, usually batch reactor studies, are reviewed in this section.

Knox *et al.* (1961) studied the formation rate of propane hydrate for development of a desalination process. They produced hydrates continuously by recycling the water phase and venting the excess gas. They observed that the liquid residence time and the subcooling affected the yield from the reactor.

Also for desalination of seawater, Pangborn and Barduhn (1970) studied the formation rate of methyl bromide hydrate in a continuous stirred tank reactor (CSTR) of 3.8 litre. The reactor was baffled and had a downward pumping impeller. They found that an increase in subcooling yields a higher hydrate formation rate. Increasing the impeller power input (calculated from the stirring rate) caused an increased rate, however, at a certain power input no further increase in rate occured. This was interpreted as a strong evidence that above a certain power input, heat and mass transfer are no longer limiting factors on the formation rate. They did not expect that the liquid residence time influences the formation rate, however, they found that the rate decreases as the slurry thickens, especially at the lowest stirring rates. Experiments carried out with liquid methyl bromide resulted in higher formation rates than experiments carried out with gaseous methyl bromide.

In 1983, Vysniauskas and Bishnoi initiated a systematic research on hydrate formation. They measured the rate of methane hydrate formation (in terms of gas consumption rate) in a semi-batch reactor, and found that the rate depends on the gas-liquid interfacial area, pressure, temperature and subcooling. Also, the effect of water memory was investigated, and it was found not to affect the gas consumption rate after nucleation. They concluded that the gas-liquid interface is the most likely place for hydrate formation to take place, because in liquid bulk, the methane concentration is too low. Experiments with ethane (Vysniauskas and Bishnoi, 1985) confirmed the observed effects.

Later, Englezos *et al.* (1987a) measured the rate of methane and ethane hydrate formation in the early growth stage before agglomeration commenced. They observed that the formation rate is a strong function of the driving force and that formation is not restricted to the interface, but also occurs in the liquid phase. Englezos *et al.* (1987b) measured the formation rate from mixtures of methane and ethane and found that the gaseous mixture composition has a significant effect on the formation rate, mainly because the composition alters the magnitude of the driving force. It should be noted, however, that no true comparison of formation rates for different gas mixtures is possible because the experimental conditions (driving forces or pressures) will never be equal.

As a part of the research at NTNU on NGH technology, Parlaktuna and Gudmundsson (1996) measured the formation rate of methane and natural gas mixture in a batch reactor of 0.62 litre. The volumetric gas consumption rates were calculated from the initial slope of pressure drop curves. They identified the subcooling and stirring rate as important parameters, and they did not observe any water memory effect. Narita and Uchida (1996) performed comparable experiments in a 0.23 litre batch reactor with methane and observed similar effects of subcooling and stirring. As an extension of the work of Narita and Uchida, Arai *et al.* (2000) performed constant pressure experiments in a 1.2 litre batch reactor. They found that the formation rate is also proportional to the system pressure.

In 1994, Happel, Hnatow and Meyer investigated the rate of methane and nitrogen hydrate formation for development of a process for separation of nitrogen from methane. Experiments were performed in a 1 litre continuous stirred tank reactor (CSTR) where gas entered the CSTR upward countercurrently to a recycled water stream. They found that their measured methane formation rates were much higher than those reported by Bishnoi and coworkers (Vysniauskas and Bishnoi, 1983, 1985, Englezos *et al.*, 1987a, 1987b). Contrary to Bishnoi and coworkers, Happel *et al.* used a baffled tank and employed higher stirring rates. Formation rates from different studies are compared and discussed in more detail in Section 2.6.

Some researchers have studied the rate of hydrate formation in the presence of liquid hydrocarbons. Bourgmayer, Sugier and Behar (1989) measured the formation rate of methane and ethane mixtures in a semi-batch reactor in the presence of a condensate. They observed that hydrates form both at the gas-water interface and at the gas-hydrocarbon interface. As Vysniauskas and Bishnoi (1983), they identified the interfacial area, subcooling and pressure as important. In addition, they found that the formation rate increases five times when condensate is present. In contrast, Skovborg (1993) discovered that a hydrocarbon liquid phase does not affect the hydrate formation rate significantly. Therefore, he suggested that the transport of gas to the water phase through a liquid water film dominates the formation rate.

From experiments with a flow loop with liquid hydrocarbon, water and dissolved gas, Gaillard, Monfort and Peytavy (1999) concluded that the transport of dissolved gas in the hydrocarbon phase to the water phase is the rate-determining step in the overall hydrate formation process. The formation rate increases as the liquid flow rate increases because of turbulence.

Østergaard *et al.* (2000) measured, in a rocking cell, the hydrate formation rate from gas dissolved in a North Sea black oil to investigate the possibilities of separating gas from oil by producing hydrates. They found that the memory effect of water and the hydrodynamic conditions greatly influence the formation rate. Also, they pointed out that better design of the reactor will significantly improve the rate, and thus, reduce the required volume of the reactor. In the same equipment, Tohidi *et al.* (1996) studied the rate of sH hydrate formation from pressure drop measurements at constant temperature. sH hydrates were made from methane, methylcyclohexane and water.

2.6 Comparison of experimental results

In a discussion of results of Bishnoi and coworkers (Vysniauskas and Bishnoi, 1983, 1985, Englezos *et al.*, 1987a, 1987b), Happel, Hnatow and Meyer (1994) stated that “Applying such information (batch reactor results) to the design of a continuous hydrate former could prove difficult”. For an order of magnitude comparison of different reactor systems, reported rates of hydrate formation are presented in Table 2.1. The selected rates of formation are presented in terms of gas consumption rate at similar temperature and pressure conditions. The units of the measured gas consumption rates were inconsistent, hence, some of the rates were recalculated.

For the comparison it should be noted that the effect of a stirring rate of 400 RPM highly depends on the size of the reactor and the impeller, the placing of the impeller and the reactor geometry. Impeller power consumption (Section 3.2) is a better parameter for comparison, but not enough data were available for the calculation.

The gas consumption rates in Table 2.1 differ with about two orders of magnitude. The consumption rate reported by Happel, Hnatow and Meyer (1994) is one to two orders of magnitude higher than the rates measured in the semi-batch or the batch reactors (except from the result of Takaoki *et al.* (2002)). Unfortunately, Happel *et al.* did not report the exact stirring rate, but the selected consumption rate was the lowest of the ones reported, and is therefore believed to represent a stirring rate substantially lower than 2250 RPM. It should be noted that the temperature in the experiment of Happel *et al.* is higher than in the experiments of others.

The geometry of the CSTR of Happel *et al.* had some important features compared to the batch reactors. Gas was bubbled through the liquid countercurrent to the liquid phase, giving a larger gas-liquid interfacial area than in the batch reactors where gas was injected into a gas pocket at the top of the reactors. In addition, the CSTR was equipped with baffles and a turbine impeller. Happel *et al.* found that the consumption rate could not be increased by increasing the subcooling because then the rate was limited by the increased heat of formation. Thus, for experiments with methane-nitrogen mixtures, Happel *et al.* modified the geometry by installing a sparger and disc-and-doughnut baffles and obtained 25-fold improvement of the reactor throughput. The work of Happel *et al.* indicates that the geometry has a large effect on the gas consumption rate, probably because of increased gas-liquid interfacial area.

Table 2.1. Methane gas consumption rates reported in the literature. Consumption rates are given at normal temperature and pressure (1 atm, 0 °C) per volume of water.

Reference	Reactor	Liq. vol. (dm^3)	Pres. (bar)	Temp. (°C)	Stirring rate (RPM)	Gas cons. rate (dm^3(NTP) $min^{-1}dm^{-3}$)
Vysniauskas and Bishnoi (1983)	Semi-batch	0.3	55	1.2	400	0.23
Englezos *et al.* (1987a)	Semi-batch	0.3	58.2	3	400	0.076
Happel, Hnatow & Meyer (1994)	CSTR	1	54	6	up to 2250	1.3
Parlaktuna and Gudmundsson (1996)[a]	Batch	0.1	71	2	400	0.17 0.78 (initial rate)
Herri, Gruy & Cournil (1996b)	Batch	1	30	1	400	0.020
Arai *et al.* (2000)	Semi-batch	0.6	70	7	700	0.21
Takaoki *et al.* (2002)	Semi-batch(?)	5.5[b]	53	3	914 [c]	1.8

---

a. Published rates are higher than the rates originally reported by Parlaktuna and Gudmundsson (1995). The data from this report is used for the comparison.

b. The reactor volume was 10 litre, but it was filled with about 5.5 kg of water.

c. Mixing Reynolds number reported instead of stirring rate. Stirring rate calculated by assuming an impeller diameter of 9 cm.

Takaoki *et al.* (2002) obtained a high gas consumption rate even though they used a batch reactor. The reactor was especially manufactured for high rate production of hydrates and had a volume of 10 litre. No details about the reactor are reported, but it is believed that its internal geometry was designed for efficient production. A high stirring rate may also explain the high consumption rate. However, a large volume does not suffice to obtain a high rate because the reactor of Happel *et al.* had the same volume as the batch reactor of Herri, Gruy and Cournil (1996b).

Vysniauskas and Bishnoi (1983) and Englezos *et al.* (1987a) performed experiments in the same reactor, but Vysniauskas and Bishnoi measured the formation rate for 10 minutes while Englezos *et al.* continued for about 85 minutes. The results of Vysniauskas and Bishnoi and Parlaktuna and Gudmundsson (1996) show that in a batch reactor, the initial gas consumption rate is higher than the rate after a longer period of time.

The comparison indicates that the consumption rate depends on the geometry of the reactor. Improvements in design affecting the gas-liquid interfacial area may enhance the formation rate by at least one order of magnitude. This means that hydrate formation experiments are highly system dependent and that models developed for one system, may not be applicable for other systems. The system dependence of such experiments is one of the motivations for the present experimental work.

2.7 Size of hydrate crystals

Englezos *et al.* (1987a) developed a model for the rate of hydrate formation including the total surface area of all hydrate crystals, which is found from *in situ* measurements of the particle size distribution. Englezos *et al.* could not measure the distribution in their experiments, so they calculated the surface area based on estimates of the critical nuclei size. However, this model initiated studies on methods to measure hydrate crystal sizes. Models and correlations are reviewed in Section 2.8.

Nerheim, Svartaas and Samuelsen (1992) used a laser light scattering technique to measure the size of nuclei in a static system during the nucleation period. They found that the critical nuclei sizes are in the range 5-30 nm, which correspond well with the calculated nuclei sizes of Engelzos *et al.* (1987).

Monfort and Nzihou (1993) measured the particle size distribution using laser light scattering during cyclopropane hydrate formation. Crystals in the range 5.6 to 564 μm could be measured. The measured size evolution with time showed that the size of small crystals rapidly increases due to crystal growth and agglomeration. Monfort *et al.* (2000) found the particle size distribution during growth of ethane and propane hydrates and calculated the growth rates. The calculated maximum growth rates for ethane and propane were 0.35 and 0.045 µm/s, respectively.

Bylov (1997) tested another laser light technique, which is able to measure larger crystals than the system of Nerheim *et al.* (1992). He found that in the first part of the experiments the mean diameter of methane, ethane and natural gas hydrate crystals grows from about 7 to 12 µm.

Herri *et al.* (1996a) developed a method for determination of particle size distribution using an optical sensor for measurement of the turbidity spectrum. This equipment was used to investigate the influence of stirring on the particle size distribution during methane hydrate formation. During the experiments the crystals had a mean diameter between 10 and 22 µm (Herri *et al.*, 1999). Herri, Gruy and Cournil (1996b) observed that at a low stirring rate (250 RPM), the mean diameter increases, while it is constant at an intermediate stirring rate (400 RPM) and decreases at a high stirring rate (600 RPM). The total number of crystals increases most rapidly with time at the highest stirring rates. At about 500 RPM, the total amount of crystals increases at a constant rate. They found that the gas consumption rate increases linearly with stirring rate but approaches zero at about 250 RPM. Below 250 RPM they did not observe hydrate formation because the induction time was too long.

In addition to studies of crystal sizes, the macroscopic morphology of hydrates has received some attention. Makogon (1997) reported the morphology of methane, ethane and propane hydrates during growth at both static and stirred conditions. He characterized the morphology by defining three types of crystals. Massive crystals start to form at the free gas-liquid interface and growth continues primarily in the gas phase. Massive crystals form at a low subcooling. Whiskery crystals are tread-like crystals and form at increased subcooling. Whiskery crystals can grow in the liquid and in the gas phase. Gelly crystals form in the water phase and where the gas is supplied from dissolved gas. Makogon, Makogon and Holditch (1999) observed that high porosity gel-like hydrate structures and microcrystals covered with a layer of water form in stirred conditions.

2.8 Gas hydrate formation models

Several hydrate formation models have been published on the basis of experimental results from batch or semi-batch reactors. All the models require fitting of experimental data to obtain empirical constants. The experimental results, on which the models rest, were reviewed in Section 2.5.

The semi-empirical model of Vysniauskas and Bishnoi (1983) represents the first attempt to describe quantitatively the rate of hydrate formation. In their model, the rate of gas consumption is correlated against total gas-liquid interfacial area, temperature, subcooling and pressure:

$$q_{Vys} = A a_s \exp\left(-\frac{\Delta E_a}{RT}\right) \exp\left(-\frac{\alpha}{\Delta T^{\beta}}\right) p^{\gamma} \tag{2.1}$$

The constants A, α, β, γ and the activation energy ΔE_a, were determined by fitting the measured methane gas consumption rates to the model. The value of γ is about three, which suggests an overall order of formation of about three with respect to pressure. The gas-liquid interfacial area was determined by measuring the contour of the vortex induced by the impeller for different stirring rates at atmospheric pressure. Vysniauskas and Bishnoi reported that the model predicts the rate of hydrate formation within ±10 % of the measured formation rate.

Englezos *et al.* (1987a) presented a growth model with a single adjustable parameter for the formation of methane and ethane hydrates. They included two steps for the growth: the diffusion of dissolved gas molecules from the liquid bulk to the crystal surface, and the integration of the gas molecules at the surface. For a single crystal, the following expression was proposed for the growth rate:

$$\left(\frac{dn}{dt}\right)_p = K^* a_p (f - f_{eq}) \qquad \frac{1}{K^*} = \frac{1}{k_r} + \frac{1}{k_d} \tag{2.2}$$

The driving force is the difference in fugacity of the dissolved gas and the three-phase equilibrium fugacity (discussed in Section 2.4). To obtain the overall formation rate for all the hydrate crystals, Englezos *et al.* defined the surface area of the crystals using the second moment of the particle size distribution μ_2. By integrating over all the crystals of any size, the overall formation rate emerged:

$$r_y(t) = 4\pi K^* \cdot \mu_2(f - f_{eq}) \tag{2.3}$$

In addition, they combined a two-film theory with Equation 2.3 to describe the gas-liquid transport. Also, they added a population balance to calculate the second moment of the particle size distribution. The single adjustable rate constant was fitted to the experimental data for each stirring rate. Based on the observation that the rate constant is independent of the stirring rate above 400 RPM, they concluded that the mass transfer resistance around the hydrate crystals is eliminated and K^* is the intrinsic rate constant.

Skovborg and Rasmussen (1994) thoroughly analyzed the model of Englezos *et al.* (1987a). They used the model to calculate the amount of gas consumed for an extended time scale, and found that the consumption rate increases with time, which is in contrast to the measured consumption rate that decreases with time. Skovborg and Rasmussen suggested that the decrease in measured rate is observed because the consumption rate does not depend on the total surface area, or because the consumption rate is controlled by transport phenomena rather than integration into the crystal structure. By changing the values of the intrinsic rate constant and the gas-liquid mass transfer coefficient, they obtained a better fit between the model and the experimental data. However, the new parameter values imply that the formation is in a region where gas-liquid mass transfer is the rate-determining step in the overall formation process.

On the basis of the analysis, Skovborg and Rasmussen (1994) proposed a simplified model where the gas consumption rate only depends on the transport of gas from the gas phase to the liquid bulk phase:

$$\frac{dn}{dt} = k_L A_{(g-l)} C_{w0}(x_{int} - x_b) \tag{2.4}$$

The consumption rate is a function of the gas-liquid mass transfer coefficient, the gas-liquid interfacial area and the mole fraction driving force. Using the data of Englezos *et al.* (1987a) to obtain the combined mass transfer coefficient, they found that the average absolute deviation between measured and calculated consumption rates is 22 % for methane and 14 % for ethane. The model was extended to more than one hydrate-forming component by assuming that the transport of the components are independent, however, this implies that all the components have the same mass transfer coefficient.

That the rate of hydrate formation may be mass transport-limited does not imply that measurements of particle size distributions are redundant. Herri *et al.* (1999) pointed out that information about the particle size distribution is not accessible with measurements of the gas consumption rate only.

On the basis of experimental results, Lekvam and Ruoff (1993) presented a reaction kinetic model for methane hydrate formation with pseudoelementary reaction steps. The initial reactants are gaseous methane and liquid water and the final product is hydrate. Reaction intermediates are dissolved methane and hydrate precursor species. The dynamic elements include gas dissolution in water phase, buildup of the precursor and growth of methane hydrate by an autocatalytic process. Rate constants were estimated for each of the five pseudoelementary reactions. The effect of stirring rate on the formation rate is modeled when gas dissolution is selected as the rate-determining step.

Gaillard, Monfort and Peytavy (1996) modeled nucleation, growth and agglomeration in their hydrate loop (with liquid hydrocarbons) applying crystallization theory and methane gas consumption measurements. They proposed a population balance for the hydrate crystals in the system and expressed the nucleation, growth and agglomeration rates by empirical correlations. Experiments showed no induction time and the rate of heterogeneous nucleation was expressed as:

$$J_p = k_{p0} \exp\left(-\frac{A}{RT}\right)(f-f_{eq})^m u^{m'} \tag{2.5}$$

where u is the liquid velocity, f-f_{eq} is the driving force (Englezos *et al.*, 1987a), and k_{p0}, A, m and m' are constants. For the growth rate, the following empirical correlation was adopted:

$$G = K \exp\left(-\frac{E}{RT}\right)(f-f_{eq})^m u^d L^b \tag{2.6}$$

where L is the crystal size and K, E, m, d and b are constants. In the model employed for the rate of agglomeration, the rate of agglomeration is proportional to the collision probability of two crystals and their sticking probability. Gaillard *et al.* could not measure the particle size distribution due to the presence of the liquid hydrocarbon phase, but they still managed to predict consumption rates in agreement with the experimental consumption rates. Similar to the conclusion of Skovborg and Rasmussen (1994), this may indicate that the rate of hydrate formation is insignificantly affected by the particle size distribution. In 1999, Gaillard, Monfort and Peytavy presented an expression for the maximum gas consumption rate without the population balance.

For their results from a semi-batch reactor, Monfort *et al.* (2000) proposed a semi-empirical model with two driving forces for the ethane and propane gas consumption rates:

$$R_{Mon} = K(\Delta T^2 + \Delta f^2)^{b_1}\omega^{b_2}a_s^{b_3} \qquad (2.7)$$

The exponents b_1, b_2 and b_3 for propane are 0.54, 0.97 and 0.15, respectively, meaning that the stirring rate ω has the strongest influence on the consumption rate, while the combined driving force has less influence and the gas-liquid interfacial area a_s has the least influence. With an on-line particle sizer, Monfort *et al.* measured the mean growth rate of the crystals and correlated the results to driving force and stirring rate:

$$\bar{V} = K\exp\left(-\frac{\Delta E_a}{RT}\right)\omega^d \Delta f^m \qquad (2.8)$$

Using the correlations, Monfort *et al.* estimated the consumption rate and the growth rate within ±10 % of the measured value.

Herri *et al.* (1999) followed up the development of a set-up for *in situ* determination of the particle size distribution (Herri *et al.*, 1996a) by presenting a model including gas absorption, primary and secondary nucleation, growth, agglomeration and breakage. The main objective was to describe the influence of stirring rate on the mean hydrate particle diameter and the total number of hydrate particles.

Herri *et al.* (1999) verified that the gas absorption follows a first-order relationship:

$$r = k_L a(C_{int} - C_b) \qquad (2.9)$$

where the driving force is the difference between the methane concentration at the gas-liquid interface and in the liquid bulk.

The model contains a population balance including a birth and a death term. A mass balance for the gas in the bulk zone describes the change in methane concentration in bulk with time. The mass balance contains the second moment of the particle size distribution. To explain the increase in initial mean diameter as stirring rate increases (Section 2.7), but also the decrease in the number of crystals, they concluded that the gas-liquid interface has to be a continuous source of nuclei, but that primary nucleation also can occur in the liquid bulk. The rates of primary nucleation at the interface and in the liquid bulk are calculated from two versions of the expression:

$$B_I = k_1 \exp\left(-\frac{B}{\log^2 S}\right) \qquad S = \frac{C_b}{C_{int}} \tag{2.10}$$

The growth rate is expressed as:

$$G = k_g(C_b - C_{eq}) \tag{2.11}$$

where k_g includes gas transport from the bulk to the surface and integration into the hydrate structure. Herri *et al.* assumed that the integration is not the rate-determining step, which contradicts the conclusions by Englezos *et al.* (1987a).

Herri *et al.* included an agglomeration term presented by Randolph and Larson (1988) to obtain an evolution of total number of particles in the reactor with time in accordance with the experimental results. An observed increasing rate of total number of particles with time for high stirring rates is accounted for by introducing secondary nucleation in the population balance. Four different equations for secondary nucleation were tested, and the one representing attrition was found to describe the experimental results. Later, Pic, Herri and Cournil (2000) presented a simplified version of the model including only primary nucleation and growth to investigate the effects of kinetic inhibitors.

The reviewed hydrate formation models strive to describe the process in terms of mass transfer concepts and crystallization theory, and to determine which step or combination of steps that are the rate-determining. Hydrate formation releases heat. Heat transfer may as well limit the formation rate, however, it is not included in any of the above models.

As far as observed, the only suggested model for the rate of hydrate formation in terms of heat transfer concepts, was recently published by Varaminian (2002). He combined an energy balance for a single crystal with an expression for the molar growth rate of a spherical particle giving the hydrate formation rate:

$$\frac{dn_{hyd}}{dt} = -\frac{4\pi h}{\Delta H} r_p^2 (T_i - T_{\mathrm{exp}}) \tag{2.12}$$

The temperature difference between the temperature at the solid-liquid interface and the experimental temperature, is the driving force. An overall hydrate formation rate was developed by introducing a density function for the total crystal surface area. The model was fitted to the experimental data for a stirred batch reactor of Englezos *et al.* (1987a).

2.9 Promoters for hydrate formation

Some surfactants are found to promote hydrate formation, by increasing the gas content and the formation rate. Tohidi *et al.* (1996) observed that the methane hydrate formation rate increases when liquid methylcyclohexane is added. Structure H hydrates form when adding methylcyclohexane to a methane-water system. In fact, they found that the rate depends on the amount of methylcyclohexane added, which means that the liquid can act as a promoter for hydrate formation.

Zhong and Rogers (2000) reported that by adding 284 ppm of sodium dodecyl sulfate to dissolve in the water phase, the rate of ethane hydrate formation is about 700 times higher than the rate for ethane hydrate formation in pure water. Similar behaviour was observed using natural gas. In addition, they noticed that interstitial water continues to convert to hydrate after agglomeration. The experiments were performed in an unstirred reactor. It should be noted, however, that the heat of hydrate formation released faster than it could be removed from the reactor. Rogers, Kothapalli and Lee (2002) found that biosurfactants increase the natural gas hydrate formation rates in porous media up to 16 times.

Applying sodium dodecyl sulfate in a stirred reactor, Han *et al.* (2002) observed that the rate of hydrate formation increased considerably. They suggested that the surfactant reduces the gas-liquid interfacial tension so that gas-liquid mass transfer is improved. In the reactor, the hydrates formed at the gas-liquid interface moved towards the reactor wall and thereby preventing blocking of the gas-liquid interface by a hydrate layer.

Karaaslan and Parlaktuna (2000) studied the influence of three commercial surfactants on the natural gas consumption rate, and found that an anionic surfactant promotes hydrate formation at concentrations between 0.005 and 1 wt %. Compared to the initial rate of hydrate formation with pure water, the initial rate with 0.01 wt % of the anionic surfactant is about threefold.

Irvin *et al.* (2000) suggested to use water-in-oil microemulsions to create a very large gas-liquid interfacial area. Such microemulsions are stabilized by a surfactant. They used the anionic surfactant bis(2-etyl) sodium sulfosuccinate and observed a very rapid ethylene hydrate formation rate in the presence of the surfactant. The use of microemulsions to promote hydrate formation presupposes that a liquid hydrocarbon is available.

Promoters may offer a potential improvement in the economy of developing technologies where hydrate production is a crucial step. However, the efficiency of such promoters cannot be quantified unless the rate of hydrate formation in pure water is determined.

2.10 Hydrate production methods

There are two main methods to produce gas hydrates:

- to introduce gas bubbles in water continuous phase, or
- to introduce water droplets in gas continuous phase.

In water continuous systems, due to the large heat capacity of water, heat of hydrate formation can efficiently dissipate in the water phase, however, large amounts of water may remain unconverted. In gas continuous systems, gas is readily available for hydrate formation, however, a hydrate film may cover the water droplets leaving free water within the hydrate crystals. In this section, large scale production methods are briefly reviewed.

The natural gas hydrate technology for storage and transport of natural gas under development by Gudmundsson and coworkers (Gudmundsson and Børrehaug, 1996, Gudmundsson *et al.*, 1998) includes production of hydrates in continuous stirred tank reactors. The gas bubbles through the liquid phase and is dispersed by an impeller. The reactor is described in detail in Section 4.2 and a brief overview of the technology was given in Section 1.1. For the same application, Mitsui Engineering and Shipbuilding (Takaoki *et al.*, 2002) recently built a 10 litre stirred batch reactor connected with equipment to make hydrate pellets.

Mitsubishi Heavy Industries (Miyata *et al.*, 2002) proposed an alternative spray method, also for storage and transport of gas. From the top of a reactor, water is sprayed into the gas phase. Formed hydrate slurry is withdrawn from the reactor and filtrated. Miyata *et al*. found that the production rate increases with pressure, subcooling and the total surface area of the water droplets. Due to limitations in the spray head and because a smaller droplet size implies a reduced water flow rate, they concluded that increased gas-liquid area is more efficiently attained by increasing the flow rate rather than reducing the droplet size.

Takahashi, Oonari and Yamamoto (2002) proposed to use a patented microbubble technology for gas hydrate production. The microbubble equipment produces gas bubbles smaller than 50 μm at atmospheric pressure. Hydrate formation is enhanced by providing a very large gas-liquid interfacial area and slow rising bubbles. So far, only small scale tests at atmospheric pressure have been reported.

Larsen *et al.* (2001) developed a concept for suppressing hydrate deposition in deep water production of oil and gas. Produced water from the well stream is completely converted to hydrate and thus eliminating free water available for further hydrate formation. A cooled fluid stream containing a large amount of dry hydrate crystals is injected into the well stream to provide cooling and seeds for crystal growth. Water droplets dispersed in the oil cover the seed crystals with a liquid water film, the stream is cooled further into hydrate forming conditions, and the liquid water film converts to hydrate. Larsen *et al.* suggest that the water content in the well stream should not exceed 10 vol %, which ensures that the stream is a water-in-oil emulsion. Experiments in a vertical hydrate reactor, which was essentially a 4” pipe, indicated that at least 0.3 vol % of dry hydrate crystals in the cooled fluid stream is necessary to convert free water to hydrate.

Takano *et al.* (2002) studied the performance of a fluidized bed reactor for production of CO_2-hydrates. Water and liquid CO_2 are supplied from the bottom of the reactor and recycled hydrate seed crystals are supplied from the lower part. Hydrate crystals exceeding the fluidization limit concentrate at the bottom and are recovered. It should be noted that CO_2-hydrates are denser than water and settles easily (density 1.13 kgm^{-3}), while the density of methane hydrates is slightly less than the density of water.

2.11 Important findings

- Initial hydrate formation takes place at the gas-liquid interface. Growth of hydrate crystals is not restricted to the interface, but may also occur in the bulk.
- The rate of gas hydrate formation is governed by the hydrodynamic conditions and the driving force for hydrate formation. Most studies indicate that the transport of gas from the gas phase to the liquid phase limits the rate of hydrate formation.
- Experimental results depend on the system where they were conducted, which means that results from batch reactors may not be valid for other reactors of different size, geometry or operation.
- Techniques to measure particle size distributions, such as laser light scattering and turbidimetry, are available, however, their use is limited to the nucleation or early growth steps where the hydrate crystal concentration is low.
- Comprehensive hydrate formation models based on mass transfer concepts and crystallization theory exist. None, except from one, include heat transfer effects. All the models are fitted to experimental data, which means that they are system specific.
- Substantial increase in the rate of hydrate formation may be achieved by changing the hydrodynamic conditions (Happel *et al.*, 1994) or adding hydrate promoters (Zhong and Rogers, 2000).

3

Stirred tank reactors

Stirred tank reactors are applied for different mixing applications: homogenization of miscible or immiscible liquids, dissolution of gas in liquid and suspension of solids. In all processes operated in stirred tank reactors, a liquid phase is the carrying fluid. Design of stirred tank reactors usually involves determination of geometry and size of tank, impeller type and heat transfer equipment. The need for internal equipment such as baffles and spargers must also be considered.

In scale-up of a process from laboratory scale to industrial plant scale, it is of crucial importance to gain knowledge about the mixing conditions in the reactor, especially if mass and heat transfer dominate the reaction rate. The experimental studies of mixing phenomena are usually concentrated around a standard geometry stirred tank where the phases are stirred with a standard impeller.

For the NTNU hydrate laboratory, a continuous stirred tank reactor (CSTR) was chosen for production of hydrates. The term *continuous* is used when the reactor operates in continuous mode so that all phases are supplied and withdrawn. An underlying assumption in modeling is that the CSTR provides perfect mixing, however, in reality mixing is highly dependent on the reactor design. In crystallization theory, an analogy to the CSTR is the continuous mixed-suspension mixed-product removal (MSMPR), which is an ideal reactor model for determination of crystal nucleation and growth rates.

URN:NBN:no-3342

Production of hydrates in a stirred tank reactor includes a gas, a liquid and a solid phase. The introduction of gas and solid complicates the mixing performance, however, in contrast to most three-phase stirred tank reactors, the density of the solid phase is close to the density of the carrying liquid. Therefore, in this chapter, gas-liquid interactions are emphasized rather than liquid-solid interactions as in an MSMPR approach.

The chapter gives an introduction to the design and the performance of stirred tank reactors. The first three sections on tank and impeller geometry, power consumption and turbulent mixing are based on the book by Oldshue (1983) and the comprehensive review by Tatterson (1991). Only turbulent mixing with radial flow impellers, as used in this work, will be considered. Mixing characteristics in the presence of gas and gas-liquid mass transfer are reviewed in Section 3.4 and Section 3.5, respectively. Scale-up of stirred tank reactors is discussed in Section 3.6.

3.1 Tank geometry and impellers

For a certain process, there is not one unique or optimal design of the reactor, and several selections can normally satisfy the process specifications (Oldshue, 1983). To simplify design and minimize costs, standard reactor designs are usually considered good enough for most processes. If not, the standard design can be viewed as a reference geometry and as a point of departure for further studies (Tatterson, 1991).

A standard design reactor for turbulent mixing of low viscosity fluids is shown in Figure 3.1. Characteristic dimensions are reactor diameter, liquid height, impeller diameter, impeller blade width, baffle width and clearance between the impeller and the tank bottom. Relative characteristic dimensions are determined based on experience. The standard reactor includes four baffles placed 90° apart. With relevance to the present work, it should be noted that a standard design implies that the liquid height is equal to the reactor diameter. In the present work, the reactor height is twice the reactor diameter.

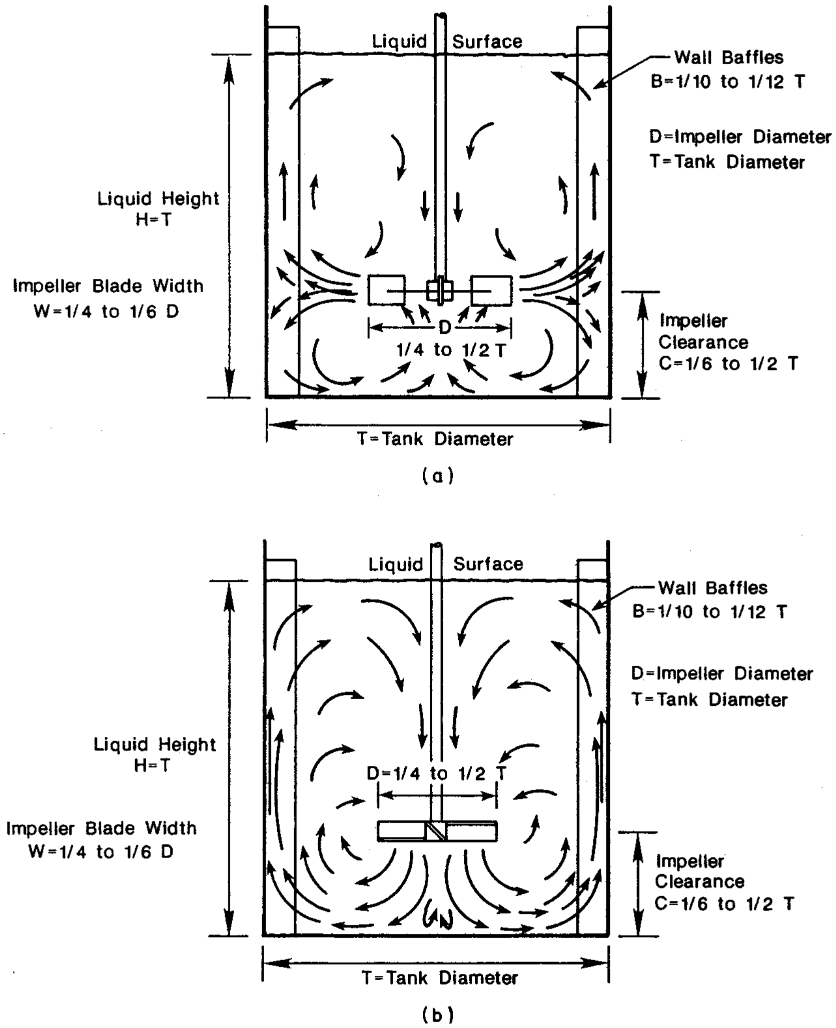

Figure 3.1 Flow patterns in a standard stirred tank reactor induced by turbulent impellers (Tatterson, 1991). (a) Flow pattern with radial flow impeller. (b) Flow pattern with axial flow impeller. In equations and nomenclature, liquid height H is called H_R *and tank diameter T is called* T_R.

Two types of impellers induce turbulent mixing (Figure 3.2). Radial flow impellers discharge fluid to the tank wall in a horizontal or radial direction. Examples of radial flow impellers are Rushton turbines (used in the present work) and curved blade impellers. These impellers are excellent for dispersion of gas in liquid. Axial flow impellers discharge material mainly axially. Examples of axial

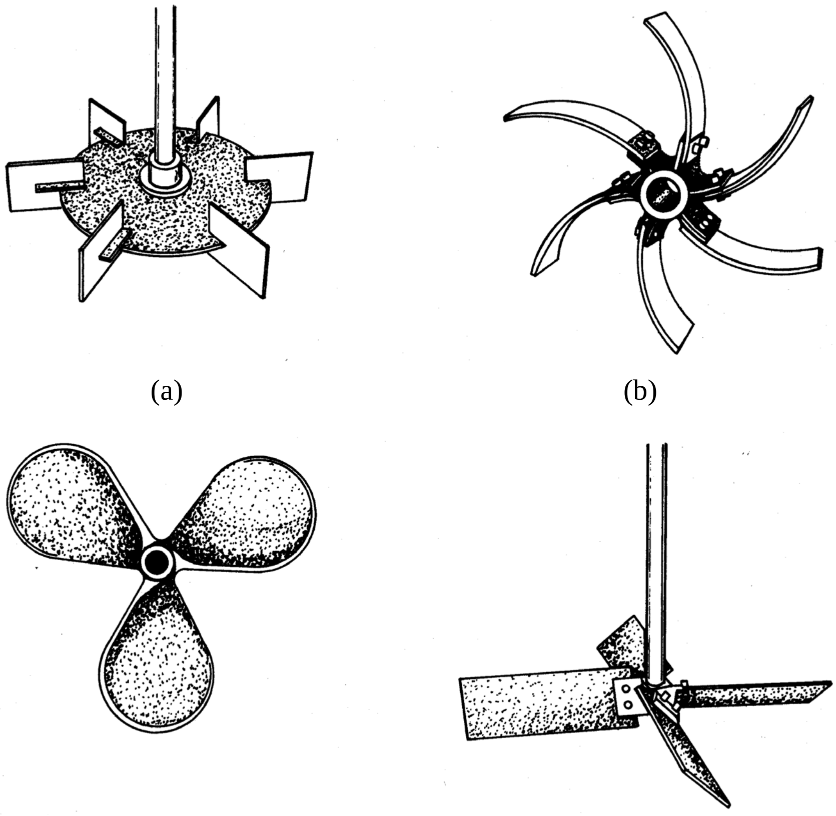

(a) (b)

(c) (d)

Figure 3.2 Turbulent impellers (Tatterson, 1991). (a) Disk style flat blade turbine, also called Rushton turbine. Radial flow impeller. (b) Curved blade turbine. Radial flow impeller. (c) Propeller. Axial flow impeller. (d) Pitched blade turbine. Axial flow impeller.

flow impellers are propellers and pitched blade turbines. These impellers are used to blend liquids and suspend solid material in liquid. Axial flow impellers may pump upward or downward.

Baffles are provided to avoid unwanted phenomena limiting mixing such as solid body rotation and development of a central vortex. In reactors without baffles at high stirring rates, a central vortex reaches down to the impeller resulting in surface gas entrainment. This may occur in laboratory scale batch reactors without baffles. Baffles mounted vertically at the tank wall are most common, however,

URN:NBN:no-3342

bottom baffles, floating surface baffles and disk baffles at the impeller shaft are possible. To avoid dead zones in the reactor, vertical baffles may be mounted at a certain distance from the tank wall. Unfortunately, the presence of baffles increases impeller power draw, however, they assure a more stable power draw and a more uniform radial shaft load, which allows longer shaft lengths (Oldshue, 1983).

In stirred tank reactors of large volumes, especially where the liquid height to tank diameter ratio is larger than one, multiple impellers provide a better top-to-bottom circulation of the bulk fluid. By using axial flow impellers, fluid can be pumped upward or downward into another impeller’s flow area, however, if they are placed less than one diameter spacing apart, they may behave as a single larger impeller. Radial flow impellers should be located at least 1.5 times the impeller diameter apart. A problem with multiple radial flow impellers is the formation of circulation cells, where exchange of mass between these cells can be poor. By using two impellers together, the impeller power consumption may drop to 70 % of the normal power consumption for two single impellers (Oldshue, 1983).

3.2 Power consumption and pumping capacity

The impeller produces flow and shear. In other words, a rotating impeller transports kinetic energy from the impeller blade to the surrounding fluid. Radial flow impellers provide a high shear rate while axial flow impellers predominantly provide a high pumping capacity.

Power consumption or power draw is the power transferred from the impeller to the fluid causing mixing. This power is eventually dissipated and ends up heating the fluid. The time averaged energy dissipation flux is termed power consumption and is equal to power draw at steady state conditions (Tatterson, 1991). The power consumption depends on:

- impeller speed/stirring rate
- impeller diameter and impeller design
- physical properties of fluid
- reactor size and geometry

- impeller location
- baffle design and location

For mixing in a standard reactor, power consumption is:

$$P = N_p \rho N^3 D^5 \tag{3.1}$$

where N_p is the power number, a dimensionless characteristic number including the effects of geometry and flow conditions. The relationship in Equation 3.1 has been verified through experiments. Another approach is to write the power number as a series of dimensionless groups:

$$\frac{Pg_c}{\rho N^3 D^5} = K\left(\frac{\rho N D^2}{\mu}\right)^a \left(\frac{N^2 D}{g}\right)^b \left(\frac{T_R}{D}\right)^c \left(\frac{C}{D}\right)^d \left(\frac{H_R}{D}\right)^e \left(\frac{W}{D}\right)^f \ldots \tag{3.2}$$

where the first dimensionless group on the right hand side is the impeller Reynolds number and the second is the Froude number. The other groups account for the effects of geometry. If a standard geometry is selected and geometric similarity is maintained, Equation 3.2 reduces to:

$$N_p = K(N_{Re})^a \tag{3.3}$$

for turbulent flow with no central vortex. The Froude number is found not to have any effect on the power number at turbulent conditions in a baffled tank (Tatterson, 1991). For different impellers, typical power number-Reynolds number relationships are found from experiments (Figure 3.3). The turbulent region begins at Reynolds numbers between 10^3 and 10^5 depending on the type of impeller. In the laminar region where the Reynolds number is lower than approximately 50, the power number is inversely proportional to the Reynolds number.

A fixed power number for a given Reynolds number is an idealization and questionable in practice. Baffles, location of impeller and tank geometry affect the power number in addition to impeller diameter, stirring rate and fluid properties (Equation 3.2). The following remarks should be considered in determination of the power number and the power consumption (Oldshue, 1983, Tatterson, 1991):

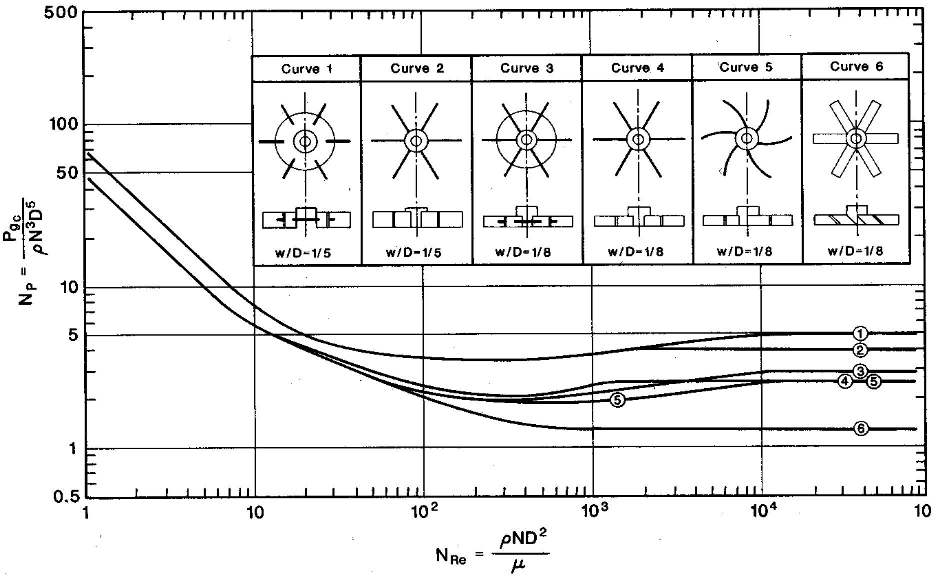

Figure 3.3 Power number versus impeller Reynolds number for Newtonian fluids and different turbulent flow impellers (Tatterson, 1991).

Baffles. Baffled tanks generally have a higher power number than unbaffled tanks. A larger baffle width and more baffles result in increased power consumption.

Impeller. The power number is not affected by an increase in the ratio of impeller to tank diameter. For Rushton turbines, the power number increases with an increased disk thickness and also with increased clearance (the distance from the tank bottom to the impeller). Other types of impellers may cause an opposite effect with respect to clearance. It is worth noticing that an off-center position of the impeller produces the same effect as baffling.

Tank geometry. Closed stirred tank reactors give rise to a higher power number over open tanks of about 5 %. However, in closed tanks the interface between the air and the liquid is eliminated, which reduces the formation of a central vortex and the need for baffling is not that critical. A side entering stream into the tank may cause the power number to increase or decrease depending on the flow rate and the feed height.

The volumetric flow rate passing through an impeller is the pumping capacity:

$$Q = N_Q N D^3 \tag{3.4}$$

where N_Q is the flow number, defined by a combination of dimensionless groups including geometrical groups. Experiments with Rushton turbines show that the flow number decreases with increasing impeller Reynolds number, but for most geometries the flow number is between 0.3 and 6.0. Several empirical correlations are available for calculating the flow number (Tatterson, 1991).

The pumping capacity determines the circulation and mixing times for a certain geometry. The circulation time tells, in average, how fast fluid elements are transported around in the reactor. In general, the circulation time increases with reactor diameter and decreases with impeller diameter, as illustrated by the following empirical correlation for circulation times in a standard tank (Tatterson, 1991):

$$N\theta_c \left(\frac{D}{T_R}\right)^2 = K_1 \tag{3.5}$$

where θ_c is the circulation time and K_1 is 0.85 for turbulent conditions.

Mixing time is the time until a non-uniform system is made uniform or ideally mixed. To be able to mix the bulk fluid in a reactor, several reactor volumes must pass the impeller, and hence, the mixing time should be longer than the average circulation time but shorter than the residence time. The mixing time is usually correlated in the same manner as the circulation time:

$$N\theta_m = K \tag{3.6}$$

where θ_m is the mixing time and K is determined by the geometry of the impeller and the reactor. To approach ideal mixing, a mixing time considerably less than the residence time is desirable. Tracer studies indicate that the mixing time should be less than 5 % of the residence time to obtain less than 5 % deviation in concentration at the exit (Tatterson, 1991). For a reactor in continuous operation, injection of feed may reduce mixing time since this energy contributes to mixing of the reactor volume, however, entering feed streams may also disrupt the flow pattern and cause less efficient mixing.

3.3 Turbulent mixing

When using radial or axial flow turbines for turbulent mixing, the fluid viscosity must be relatively low to ensure turbulent mixing in the whole reactor volume rather than in the impeller zone only. The flow fields generated under turbulent flow conditions are complex, containing high-speed discharge flows, trailing vortices and boundary layers (Tatterson, 1991). Interior structures on different scales, described as macromixing and micromixing, occur. Before micromixing is established, any reactions in the reactor volume may proceed at different rates. High-shear mixing is recommended to avoid an inhomogeneous process, especially for fast reactions. This section is limited to a brief description of flow fields in the discharge flow, near the impeller and in the liquid bulk produced by a Rushton turbine. Micromixing and flow fields in stirred tank reactors are thoroughly reviewed by Tatterson.

Similar to power consumption and pumping capacity, the flow fields in a standard stirred tank reactor depend on the impeller and tank geometry, number of impeller blades and baffles and fluid properties. The discharge flow from a Rushton turbine is characterized by two trailing vortices at the top and the bottom of the impeller blade and a high-velocity radial discharge flow in the middle. The mixing occurs mainly in the flow passing through the vortices and where the discharge flow meets the bulk flow. The maximum velocity in the radial discharge flow is about equal to the impeller tip velocity, and the circumferential velocity in the vortices is about two times the tip velocity, indicating that these flows represent high shear zones in the reactor.

Upon leaving the impeller blade, the trailing vortices turn tangentially and have a short duration time before they break up. The disk on the Rushton turbine splits the discharge flow and causes one circulation cell above the impeller and one below. Mixing between the cells takes place in the discharge flow.

The flow velocities in the bulk are much lower than the discharge flow velocities. The overall flow pattern is indicated in Figure 3.1a. In the liquid bulk, the discharge flow dissipates and turns axially near the reactor wall causing the tangential velocities to decrease. Slightly more than 50 % of the flow circulates towards the top while the rest circulates towards the bottom of the reactor. This produces two regions of low mean velocity. One is located approximately midway between the impeller and the reactor bottom at approximately 70 % of the radius of the reactor, and one halfway between the impeller and the liquid surface, also at about 70 % of the reactor radius (Oldshue, 1983).

3.4 Gas-liquid mixing

Introduction of gas disturbs the flow fields in a stirred tank reactor, and thereby changing the performance of the reactor significantly. Indeed, gas dispersion in liquid is identified as an operation very sensitive to impeller design (Oldshue, 1983). Gas liquid mixing in standard stirred tank reactors with Rushton turbines has been extensively studied. Rushton turbines are most convenient for gas dispersion because the disk disturbs the free rising of gas bubbles through the reactor.

This section includes gas dispersion flow regimes, effect of gas on power consumption and presentation of important parameters in gas dispersion. Gas-liquid mass transfer is treated separately in Section 3.5. With relevance to the present work, it should be noted that the description of gas-liquid mixing in the literature is based on experiments in an open standard reactor at atmospheric pressure. More recently, the effect of pressure on relevant parameters has been investigated. Some relevant studies will be presented.

Different flow regimes in gas-liquid reactors are illustrated in Figure 3.4. The stirring rate and the gas flow rate determine the type of flow regime. At low stirring rates and at high gas flow rates, the impeller is flooded, meaning that the impeller is overwhelmed with gas and the gas is allowed to rise unhindered near the impeller shaft. The gas-liquid interfacial area and the contact time are very low and so is the mass transfer (Whitton, 1992). As the stirring rate increases, the pumping action of the impeller begins to dominate, and the gas bubbles are thrown radially from the impeller towards the wall. The impeller power input is two to three times the power supplied from the gas stream (Oldshue, 1983) and the impeller is in the loaded regime. When stirring rate is increased so that the power input is about five times the gas stream power, the bubbles are swept into the region below the impeller resulting in a completely uniform distribution of the gas

URN:NBN:no-3342

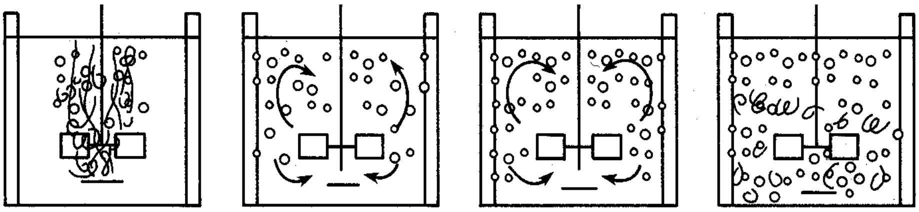

Figure 3.4 Gas dispersion flow regimes (Tatterson, 1991).

in the liquid phase. As power input is further increased, the degree of gas recirculation increases.

A complete dispersion of the gas is no guarantee for good mass transfer, however, the flow regime indicates whether the process is impeller controlled or gas controlled, which is relevant for the validity of empirical correlations and scale-up relationships. Whitton (1992) suggests the correlations of Nienow for estimating the operating conditions where the transition between the flow regimes occurs. For a standard Rushton turbine, the transition from a flooded to a loaded condition is given by:

$$N_{QG,F} = 30\left(\frac{D}{T_R}\right)^{3.5} Fr \tag{3.7}$$

where $N_{QG}=Q_g/ND^3$ is the gas flow number and $Fr=N^2D/g$ is the impeller Froude number. The relationship is reported to work well for reactors up to 2.67 m in diameter, D/T_R ratios from 0.22 to 0.50 and impeller clearances C/T_R between 0.25 and 0.4 (Whitton, 1992). Similarly, the transition between loaded condition and complete dispersion is:

$$N_{QG,CD} = 0.2\left(\frac{D}{T_R}\right)^{0.5} Fr^{0.5} \tag{3.8}$$

and the transition from complete dispersion to recirculation is:

$$N_{QG,R} = 13\left(\frac{D}{T_R}\right)^{5} Fr^{2} \tag{3.9}$$

where both Equation 3.8 and Equation 3.9 are limited by the same range of geometries as Equation 3.7. The degree of gas recirculation (Equation 3.9) depends on the coalescing behaviour because the degree of recirculation increases as the bubble size decreases. Thus, in systems where coalescence is inhibited, the degree of recirculation increases (Whitton, 1992).

Less impeller power is required when gas is present in the reactor (gassed conditions) than when liquid only is present (ungassed conditions). Due to the formation of gas cavities behind the impeller blades, drag and power are reduced. The shape of such cavities impacts the gassed power consumption. The gassed power consumption is used as a correlation parameter in determining gas holdup, gas-liquid interfacial area and mass transfer coefficient.

From experimental data, several correlations between gassed and ungassed power consumption have emerged (Tatterson, 1991), however, the complexity of gas cavities and how they affect the gassed power consumption leads to approximate correlations only. Amongst others, Tatterson provides the correlations of Calderbank for determination of the gassed power consumption:

$$\begin{aligned} \frac{P_g}{P} &= 1 - 12.6 N_{QG} \qquad && \text{for } N_{QG} < 0.035 \\ \frac{P_g}{P} &= 0.62 - 1.85 N_{QG} \qquad && \text{for } N_{QG} > 0.035 \end{aligned} \tag{3.10}$$

Typically, gassed power consumption drops rapidly from 1.0 to between 0.3 and 0.6 times the ungassed power consumption as the gassed flow number approaches 0.035 to 0.05.

The gas holdup determines the maximum liquid volume for a reactor of a given size. The typical gas holdup in industrial reactors ranges from 5 to 15 %. The gas holdup in a reactor is the gas volume to the total volume of the dispersion:

$$\varepsilon_G = \frac{V_G}{V_G + V_L} \tag{3.11}$$

In the literature, measured gas holdup is correlated in terms of the independent parameters stirring rate and volumetric gas flow rate:

$$\varepsilon_G = \alpha N^{\beta} Q_G^{\ \gamma} \tag{3.12}$$

or in terms of the dependent parameters gassed power consumption and superficial gas velocity:

$$\varepsilon_G = \alpha \left(\frac{P_g}{V}\right)^{\beta} v_{sg}^{\ \gamma} \tag{3.13}$$

where the superficial gas velocity is the volumetric gas flow rate per cross sectional area of the reactor. Equation 3.13 has a poor theoretical basis, but seems to correlate experimental data better than the correlation for gas holdup in Equation 3.12. Tatterson (1991) reported that a typical value of β is between 0.20 and 0.53 and for γ between 0.36 and 0.75.

Whitton (1992) concluded in his study of the performance of multiple impellers in tall reactors, that gas holdup is practically independent of reactor geometry and impeller configuration for a given power consumption and superficial gas velocity below flooding conditions. He obtained a maximum holdup of 20 % and observed that the gas holdup tends to level out at high power consumptions and superficial gas velocities.

3.5 Gas-liquid mass transfer

The rate of mass transfer of gas from gas to liquid is determined by the mass transfer coefficient, the interfacial area and the difference between the gas concentration at the interface and in the liquid bulk phase. For sparingly soluble gases in liquid, such as methane, ethane and propane in water, the mass transfer rate is (Froment and Bischoff, 1990):

$$r = k_L a (C_{int} - C_b) \tag{3.14}$$

The mass transfer coefficient and the interfacial area are often combined because these parameters are difficult to measure separately. The combination is called the volumetric mass transfer coefficient.

Many researchers have reported volumetric mass transfer coefficients in stirred tank reactors of standard design (Tatterson, 1991). Likewise to gas holdup, the volumetric mass transfer coefficient has been correlated successfully to the gassed power consumption and the superficial gas velocity:

$$k_L a = \alpha \left(\frac{P_g}{V} \right)^{\beta} v_{sg}{}^{\gamma} \tag{3.15}$$

Others have correlated the volumetric mass transfer coefficient to dimensionless numbers, such as:

$$\frac{k_L a D^2}{D_L} = K \left(\frac{\rho N D^3}{\mu} \right)^a \left(\frac{N^2 D}{g} \right)^b \left(\frac{\mu}{\rho D_L} \right)^c \left(\frac{\mu v_{sg}}{\sigma} \right)^d \left(\frac{ND}{v_{sg}} \right)^e \tag{3.16}$$

where the term on the left hand side is the modified Sherwood number and the terms on the right side are the Reynolds number, the Froude number, the Schmidt number, the reciprocal of a gas number and a modified gas flow number.

In the present work, the reactor system has some special features. The reactor height is twice the reactor diameter, the reactor is operated at high pressure and growing hydrate crystals are present during gas-liquid dispersion. A limited amount of studies on the effect of such departures from gas-liquid dispersion in a standard reactor are published.

Nocentini *et al.* (1993) compared the volumetric mass transfer coefficient in a tall reactor with multiple Rushton turbines with the volumetric mass transfer coefficient obtained in a standard reactor with a single turbine. Experiments were carried out with water and air in a reactor with diameter 0.23 m and a height three times the diameter. The reactor had four turbines. Nocentini *et al.* showed that correlation coefficients in an expression equal to Equation 3.15 agree well with correlation coefficients obtained for standard reactors with a single impeller. Their results show similar good agreement with gas holdup correlations for single impeller standard reactors. Also, the study indicates that the volumetric mass transfer coefficient is close to proportional to the gas holdup.

The effect of pressure on the volumetric mass transfer coefficient can be divided into the effect of pressure on hydrodynamics and the effect on physical properties of the phases present. Maalej, Benadda and Otterbein (2001) studied the effect of pressure and gas flow rate on k_La, k_L and a in an agitated bubble reactor. The reactor was filled with carbonate-bicarbonate solution and the gas was a mixture of nitrogen and CO_2. Experiments were carried out at pressures from 1 to 50 bar. They found that both the interfacial area a and the volumetric gas flow rate k_La decrease with increasing pressure because the bubble diameters and volumes decrease with increasing pressure. On the other hand, because pressure does not influence the physical properties of liquid, the mass transfer coefficient k_L is not a function of pressure. Also, Maalej *et al.* found that a and k_La increase with increasing gas flow rate.

Stegeman *et al.* (1995) measured the interfacial area in a stirred tank reactor at pressures up to 66 bar. They observed that at normal superficial gas velocities, the interfacial area is not influenced by pressure, however, at a high superficial gas velocity (0.02 m/s), the interfacial area increases with increasing pressure. Also, they found that gas holdup is independent of pressure. Maalej *et al.* (2001) pointed out that the studies on mass transfer phenomena at elevated pressure diverge, and that the influence of pressure on the interfacial area and mass transfer coefficient depends on the type of reactor.

In their review on three-phase stirred slurry reactors, Chaudhari and Ramachandran (1980) concluded that solids do not significantly affect the volumetric mass transfer coefficient. Later, Oguz, Brehm and Deckwer (1987) reviewed the literature and found that for some systems and types of particles, the volumetric mass transfer coefficient increases with increasing solid concentration for low concentrations, but begin to decrease at high concentrations. In other systems, the volumetric mass transfer coefficient decreases with increasing solid concentration.

Oguz *et al.* (1987) studied the effect of fine particles in a 4 litre stirred tank reactor. The aqueous slurries used, all containing particles with diameters less than 80 μm and with density above $2.07 \cdot 10^3$ kgm^{-3}, showed non-Newtonian behavior and were regarded pseudohomogeneous. Oguz *et al.* found that the volumetric mass transfer coefficient decreases significantly with solid concentration for nearly all the slurries investigated. However, when they accounted for the slurry density in calculation of power consumption and included the slurry viscosity in their correlation for volumetric mass transfer coefficient, their correlation corresponds well with correlations for volumetric mass transfer coefficient for gas-liquid systems. Andersson (1999) provided results on density and apparent viscosity of non-Newtonian hydrate slurries as a function of hydrate crystal concentration.

Ozkan *et al.* (2000) found that at low solid concentrations, the volumetric gas-liquid mass transfer coefficient increases approximately threefold compared to the coefficient for pure water. They suggested that a low solid concentration might hinder coalescence of bubbles and thereby increase the interfacial area and the mass transfer coefficient. However, at high concentrations, solids may cover the gas-liquid interface and thus hinder diffusion of the gas. Solids may also dampen the turbulence. In fact, they did not conclude about the effect of solid concentration on the volumetric mass transfer coefficient. It should be noted that the effect of particles is investigated in slurry reactors with a solid density considerably higher than the density of water. The density of methane and natural gas hydrate is slightly less than the density of water, hence, the hydrate crystals will float.

The effect of floating particles on the volumetric mass transfer coefficient has not been reported in the literature. Bakker and Frijlink (1989) discussed drawdown of floating particles in stirred tank reactors. In liquid reactors with floating particles, drawdown is most efficiently performed by creating a vortex, however, vortex formation is suppressed in gassed systems. Therefore, instead of using a Rushton turbine for efficient gas dispersion, they recommend as a compromise to use an upward axial flow impeller for simultaneous gas dispersion and drawdown of particles. Then, the particles are transported to the reactor walls, drawn down and suspended. With a downward pumping impeller, the drawdown flow is in the center and is counteracted by the rising gas flow. Xu *et al.* (2000) investigated numerous combinations of impellers and baffle configurations in a tall reactor. They found that an upper upward pumping propeller (Figure 3.2c), a middle downward pumping propeller and a lower Rushton turbine provide the most efficient drawdown of floating particles and simultaneous dispersion of gas.

Based on the reported effects on mass transfer, several options for improving the mass transfer rate can be identified. According to Equation 3.14, the mass transfer rate can be increased by influencing the volumetric mass transfer coefficient or the concentration driving force. The volumetric mass transfer coefficient increases with power consumption and superficial gas velocity. Pressure does not seem to increase the volumetric mass transfer coefficient, however, increased pressure results in a larger concentration driving force. The gas concentration at the interface, that is the solubility of the gas in the liquid, increases with higher gas bulk pressure. The presence of particles, especially for low particle concentrations, may improve the volumetric mass transfer coefficient, but this is questionable as the literature on the effect of particles is contradictory.

3.6 Scale-up of stirred tank reactors

Scale-up of a stirred tank reactor includes two major tasks:

- identification of a criterion or criteria for scale-up, and
- accomplishment of a suitable procedure for scale-up.

Through experiments, parameters that affect the process result, especially those parameters that the process is sensitive to, must be identified. In addition, relationships showing how crucial parameters are affected by operational conditions and reactor and impeller geometry are needed. Each type of process has unique scale-up procedures that are determined by testing and experience.

Identification of the criterion includes choosing a parameter or a group of parameters, in terms of a dimensionless number, to remain constant during scale-up of the reactor. Concepts of kinematic (all velocity ratios equal) and dynamic similarity (all force ratios equal) suggest using dimensionless groups in scale-up, however, this approach cannot be applied in processes where the dimensionless group is not easily identified (Oldshue, 1983). The concept of geometric similarity (all dimensional ratios equal) will usually change the flow fields and the process result considerably. Instead, selecting one parameter to remain constant upon scale-up and then predicting the effect on the other parameters is an option. Depending on the process, scale-up can be based on constant:

- impeller power consumption per volume
- pumping capacity
- impeller tip speed
- average/maximum shear rate
- impeller diameter/tank diameter ratio

- mixing time
- superficial gas velocity
- gas-liquid interfacial area
- gas holdup
- volumetric mass transfer coefficient

It is important to note that keeping a single parameter constant usually leads to undesirable effects on other parameter, and therefore these consequences must be properly identified. Scale-up is always a trade-off between different parameters, especially in multi-phase reactors where different processes need contradicting conditions.

Looking at the flow field, the content of a laboratory reactor is typically well mixed, while the content of a large scale reactor may have zones where the turbulence is not well developed, typically in bulk and in the upper part of the reactor. The turbulent macroscale eddies created by the impeller is of the same order of magnitude as the impeller blade width (Tatterson, 1991). This means that larger eddies will form in large reactors compared to small reactors. Consequently, upon scale-up, increased variations in velocities and concentrations can be expected with the result that the final state of mixing to be achieved takes more time. In processes where shear is the main purpose of the mixing action, for example in gas dispersion, scale-up of the impeller diameter leads to larger variation in shear rates as well as higher maximum shear rate (Oldshue, 1983). Thus, the geometry must change to obtain a similar flow field in a large tank. Usually, larger volumes require taller reactors but not with equally larger diameter, which in turn may require multiple impellers.

For single phase liquid processes, Oldshue (1983) suggests first to examine the effect of constant power per liquid volume and geometric similarity, and then calculate the total power requirement, impeller speed and diameter, shear rates and pumping capacity. Different impeller/tank diameter ratios can be investigated to modify some of the effects. It is worth noting that the heat transfer coefficient is not significantly affected by changes in impeller power consumption, which means that other mixing applications than energy dissipation is often controlling the process (Oldshue, 1983). However, the heat transfer area usually decreases upon scale-up and therefore, additional internal heat transfer area such as coils may be required in a large tank.

Tatterson (1991) reviewed the published literature on scale-up of gas dispersion processes. Constant gas-liquid interfacial area is recommend, and is achieved by constant impeller tip speed and constant impeller/tank diameter ratio upon scale-up. Constant power consumption per volume may also provide constant interfacial area. Another approach is to maintain constant volumetric mass transfer coefficient, however, when maintaining geometric similarity, the volumetric mass transfer coefficient does not remain constant with power consumption per volume and superficial gas velocity. Therefore, larger reactors must generally be taller to accomplish constant volumetric mass transfer coefficient. Yet another criterion that may be successful, is to maintain constant volume of gas per volume of liquid.

In crystallization processes, impeller power consumption is a critical parameter as it affects the nucleation rate and the agglomeration and breakage of crystals. Mullin (1993) suggests several scale-up criteria, amongst them constant power consumption or constant impeller tip speed. Another approach is constant density of the liquid-solid suspension and constant residence time in the reactor. This is achieved by maintaining the ratio of squared impeller tip speed to turnover time (reactor volume/circulation rate) constant. Also, Mullin suggests to adjust the stirring rate to a level where all crystals are just in suspension.

3.7 Important findings

- Radial flow impellers such as the Rushton turbine are best suitable for gas dispersion in liquid. Axial upward flow impellers can be used in combination with radial flow impellers to keep floating particles in suspension and simultaneously obtain efficient gas dispersion.
- Correlations are available for calculation of impeller power consumption in a standard reactor. Closed reactors change the power consumption by no more than 5 %.

- Gas-liquid flow regime determines the dispersion of gas in liquid. Correlations to calculate the stirring rate for the transition between regimes are available for stirred tank reactors of standard design and for a large range of relative dimensions.
- Many researchers have reported gas-liquid volumetric mass transfer coefficients for various systems. This usually includes air and water at atmospheric pressure, and such correlations may therefore not be applicable to other systems.
- Correlations for volumetric mass transfer coefficients in standard reactors seem to hold for tall reactors with multiple impellers.
- Pressure does not seem to affect the mass transfer coefficient, but may influence the gas-liquid interfacial area, meaning that the volumetric mass transfer coefficient is a function of pressure.
- The effect of particles on the volumetric mass transfer coefficient is unclear. Both increase and decrease with particle concentration have been reported.
- Gas-liquid volumetric mass transfer coefficient and gas-liquid interfacial area are important parameters in scale-up of gas dispersing reactors. Power consumption is a crucial parameter in liquid-solid reactors.

4

Laboratory and experimental procedures

The experimental work was carried out in the natural gas hydrate laboratory at NTNU. This laboratory was built in 1997 to investigate different properties of natural gas hydrates for transport and storage of natural gas. Detailed descriptions of the laboratory are given in the Dr.ing. theses of Andersson (1999) and Levik (2000).

In this chapter, equipment and procedures relevant for rate of hydrate formation measurements are described. An overview of the laboratory is given in Section 4.1 and the reactor is described in Section 4.2. Gas flow meters, pressure regulator, pressure transducers and temperature sensors as well as data acquisition equipment are specified in Section 4.3. The experimental procedure and practical considerations in the experimental runs are described in Section 4.4 and Section 4.5, respectively. The analysis of the results is explained in Section 4.6.

4.1 Hydrate laboratory

The hydrate laboratory consisted of a flow loop with four main units: a reactor, a separator, a heat exchanger and a circulation pump. A flow diagram of the laboratory is shown in Figure 4.1. The units were interconnected with 25 mm OD

URN:NBN:no-3342

stainless steel tubes. In addition, the flow loop had a test section with quick connections for replacement of different test units. The volume of the flow loop was about 34 litre.

The flow loop was situated in a temperature-controlled room to avoid temperature gradients between the flowing media and the surroundings. The room temperature could be varied from 0 to 20 °C. The flow loop was designed for 120 bar pressure. For safety reasons, the laboratory equipment was classified for installation in hazardous area zone 2.

The reactor was of standard design and had a volume of 9.5 litre. Hydrates were formed in the reactor by injecting gas from the bottom of the water-filled reactor while stirring its content. The reactor is described in detail in Section 4.2. The separator was a vertical tank with the same diameter but twice the length of the reactor, giving a volume of 19 litre. The reactor and the separator were designed at NTNU and built by Proserv A/S. The main purpose of the separator was to separate unconverted gas from the slurry phase to obtain, as far as possible, a gas free hydrate slurry for the test section. The separator had three pairs of view-ports placed directly opposite at three different levels. The inlet line of the separator was connected close to the top, while the exit line was connected near the bottom. An air-driven positive displacement pump (Haskel piston pump) was mounted to the separator to provide mixing of hydrate and water, and thereby avoid accumulation of hydrates in the separator.

The heat exchanger was a shell-and-tube heat exchanger manufactured by Sperre Industri AS. The heat exchanger removed heat of hydrate formation and heat from rotating equipment such as the circulation pump and the stirrer in the reactor. The hydrate slurry flowed on the tube side, while a cooling medium consisting of glycol and water flowed on the shell side. The streams followed a cross-counter flow pattern. The cooling media was circulated with a constant flow centrifugal pump, and gave away heat to a secondary cooling media of propane in a plate heat exchanger. The minimum temperature of the secondary cooling media was -30 °C. The propane system was installed by Klima & Kuldeteknikk AS. The duty of the heat exchanger was regulated with a Samson three-way regulating valve based on a temperature measurement either in the reactor or downstream the heat exchanger. The setup of the heat exchanger system was intended to provide data

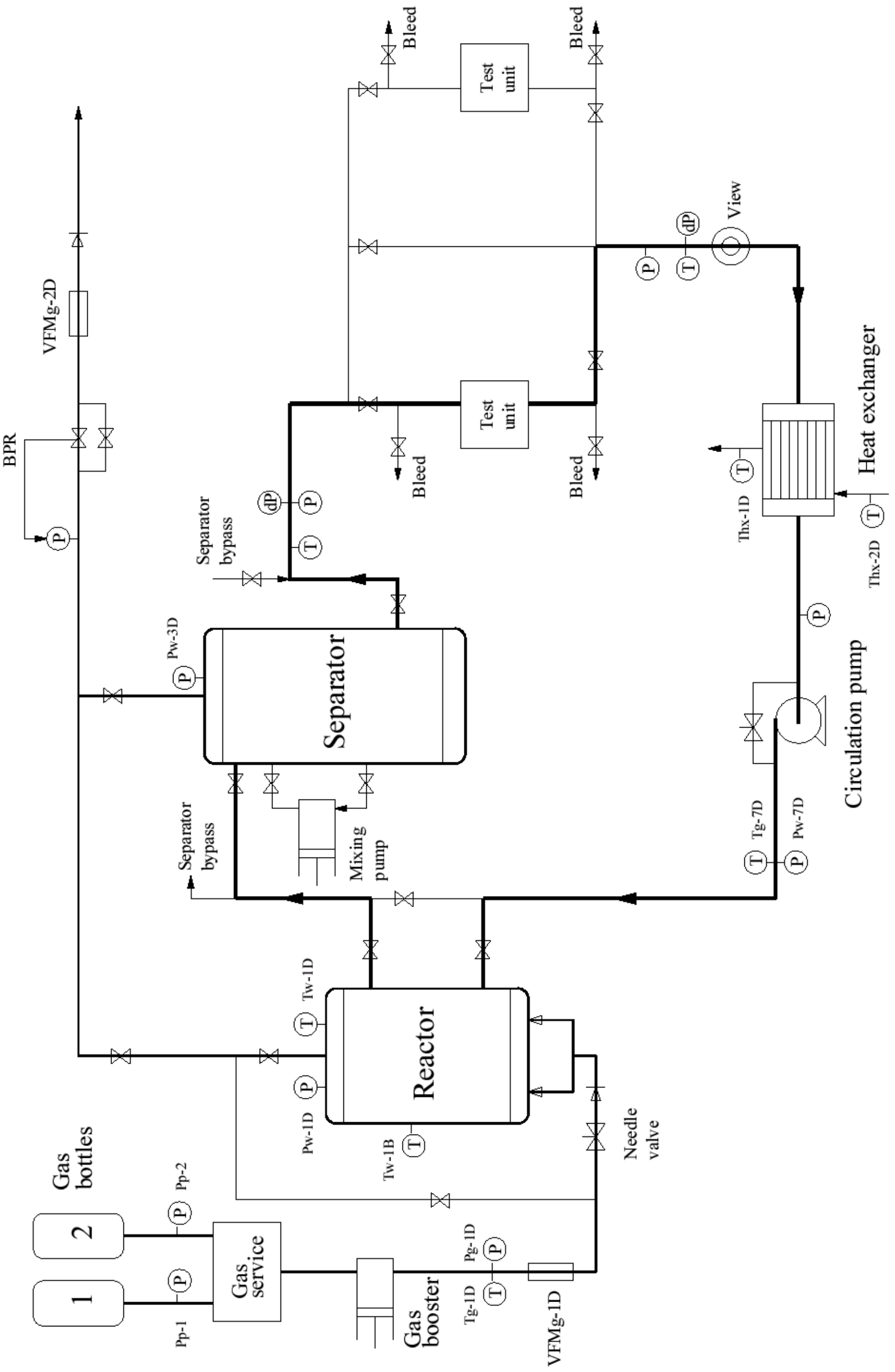

Figure 4.1 Flow diagram of the natural gas hydrate laboratory at NTNU.

for calculation of the heat exchanger duty, however, problems in operation of the regulation system made this difficult.

The circulation pump was a Caster magnet-driven centrifugal pump. The capacity was 100 litre per minute and the maximum head was 5 bar. The pump had a 5.5 kW motor with a continuous variable torque control. In the pump, degradation of hydrate particles was expected, however, Andersson (1999) did not observe any degradation in measurements of hydrate slurry properties in the NTNU laboratory.

Gas was supplied to the reactor from gas bottles normally of 50 litre. The gas bottles were placed in a separate room and were connected to the reactor by 6 mm OD stainless steel tubes. The gas injection line was about 6 meter long. Two bottles could be connected at the same time. A gas service panel with pressure-reducing valves provided adjustment of the pressure to the flow loop. The panel also displayed the gas bottle pressures and enabled switching from one bottle to another. A Haskel piston compressor could be used to boost the gas to a maximum pressure of 250 bar. A gas vent line from the top of the separator, also made of 6 mm OD stainless steel tubes, purged the gas. Different instruments connected to the injection and vent lines are described in Section 4.3.

A degassing tank and a vacuum pump were used to inject water into the flow loop. To avoid that dissolved air in water affected the results, water was deaerated in the tank before injection. The tank of about 80 litre was made of PVC and could be pressurized, typically with methane, to about 2 bara. The water was deaerated using the vacuum pump. Also, the vacuum pump could be connected to the flow loop for evacuation. The vacuum pump was made by Leybold and provided a pressure less than 1 mbara.

4.2 Reactor

The reactor was made of stainless steel and consisted of a cylinder with 258 mm OD and 180 mm ID. Lids were mounted at the top and the bottom of the cylinder. The cylinder wall had 8 ports in two levels. The liquid inlet and outlet were placed in two ports above each other. View ports were installed in two opposite lower ports.

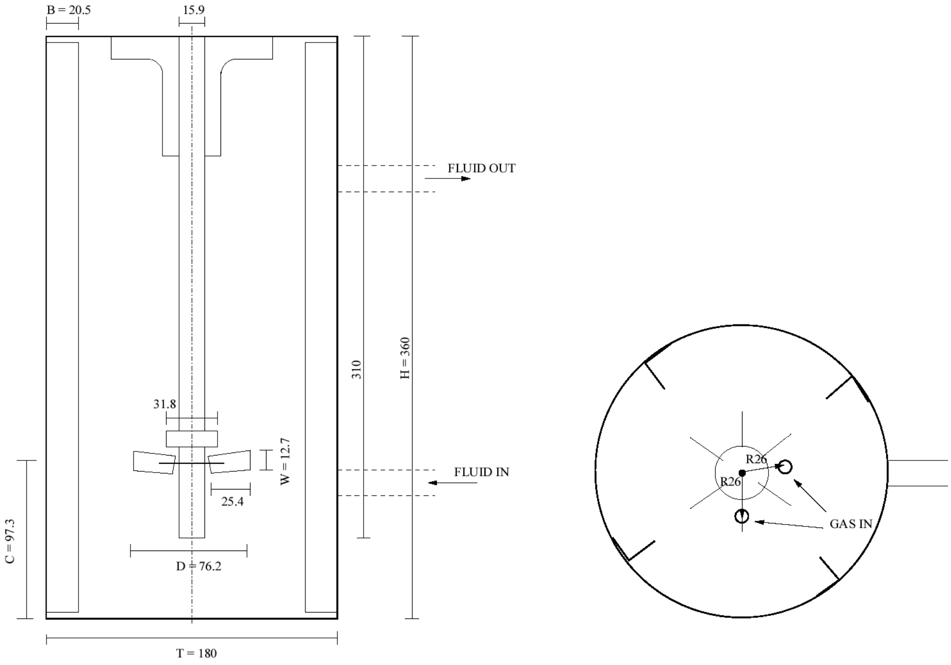

Figure 4.2 Inside geometry of 9.5 litre stirred tank reactor. Lengths are in mm. H and T correspond to H_R and T_R in nomenclature.

The inside geometry of the reactor is shown in Figure 4.2. Four equally spaced baffles were fitted to the reactor wall. The relative dimensions of the reactor and the impeller were:

- reactor height/tank diameter: $H_R/T_R = 2$
- impeller diameter/tank diameter: $D/T_R = 0.42$
- impeller clearance/tank diameter: $C/T_R = 0.54$
- baffle width/tank diameter: $B/T_R = 0.11$

The impeller was a disk impeller with six straight blades, also called a Rushton turbine. It was driven by an Autoclave Engineers Magnedrive, a magnetically coupled rotary impeller system. The stirring speed could be varied between 0 and 2500 RPM. The rotational speed was measured and displayed.

The gas was injected through two inlets placed within the radius of the impeller at the bottom of the reactor. The inlets had check valves to prevent backflow into the gas injection line. Stainless steel filters (7 µm) were also placed at each inlet to obtain small gas bubbles, however, a test at atmospheric pressure indicated that the bubble diameter resembled the diameter of the check valve outlet rather than the diameter of the filter pores. It was therefore believed that small gas bubbles probably coalesced rapidly before rising to the impeller.

Except from the height, which was twice the diameter of the reactor, the relative dimensions were similar to a standard design stirred tank reactor as discussed in Section 3.1. Gas and liquid were continuously charged to and discharged from the reactor enabling steady-state operation. Due to standard design and steady-state operation, the reactor was called a continuous stirred tank reactor (CSTR).

4.3 Instrumentation and data acquisition

On the gas injection and gas vent lines, gas flow meters were installed to measure the gas flow rates in terms of normal litre per minute (Nl/min). The unit refers to the volumetric gas flow rate measured at 0 °C and 1 atm. Throughout the present work, Nl/min is always according to the conditions above and *atm* or *bar* always denote absolute pressures if nothing else is stated.

The gas flow meter on the gas vent line (VFMg-2D) by Bronkhorst Hi-tec (type F-122MX) was calibrated by the manufacturer for methane gas at 80 bar and 10 °C. Maximum measurable flow rate was 165 Nl/min. With the software Flow Calculations (FLUIDAT) version 1.13 (1994), the measured gas flow rate was corrected for other gas compositions and pressure and temperature conditions. Several tests were performed to calibrate the gas flow meter using PVT-data from the gas bottle (described below), but the method was found less reliable than the precalibration from the manufacturer and thus, the precalibration was applied.

The gas injection rate could be measured with a Brooks controller (type MF51S) at the gas injection line (VFMg-1D). The measurement range was between 20 and 100 Nl/min for nitrogen, which corresponded to 16.2 to 80.8 Nl/min for methane. Also, the flow meter had a controller function to stabilize the flow at a set flow rate. For the present experiments, gas injection rates above 100 Nl/min were usually desirable. Therefore, the Brooks controller was *not* used, and the gas injection rate was found by using PVT-data for the gas bottle instead (described in Section 4.6). Both flow meters (VFMg-1D and VFMg-2D) were equipped with readout units for displaying measured values and adjusting settings. The measured flow rates were also displayed in the laboratory.

On the gas vent line, a back pressure regulator (BPR) supplied by Bronkhorst Hi-tec (type F-033C-XC), provided constant pressure in the flow loop during the experiments. The BPR consisted of an upstream pressure transducer and a electrically activated valve. The valve opened when the pressure, measured with the upstream pressure transducer, exceeded a set value. In this way, when the pressure in the flow loop exceeded the set value, gas was vented out continuously.

Pressure transducers and temperature sensors were installed upstream and downstream the main units as well as in the reactor and in the separator (Figure 4.1). For monitoring of the flow loop during experiments, measured pressure and temperature were displayed in the laboratory (labeled with “D” in Figure 4.1). Keller pressure transducers and PT-100 temperature sensors were used. In addition, a differential pressure transducer (dP) measured the pressure drop over the test units.

Voltage signals from gas flow meters, pressure transducers and temperature sensors were transferred to a separate control room for data acquisition on a personal computer. The software LabVIEW supplied by National Instruments collected the data, assigned physical values to the different signals according to the calibrations embedded and wrote the data to file at an optional time interval. Due to the amount of data collected, the minimum time interval was about 3 seconds.

4.4 Experimental procedure

Methane gas with 99.99 % purity or a natural gas mixture consisting of 92 % methane, 5 % ethane and 3 % propane (both supplied from AGA AS), were used in the experiments. The water was the ordinary cold tap water in Trondheim.

The experimental procedure included the preparation of the system and the carrying out of the experiment itself. Some experiments were carried out at the same conditions as the previous experiment, and therefore, a full preparation of the system was not necessary.

In the preparation, the flow loop was cooled, filled with deaerated tap water and pressurized to a pressure close to the hydrate equilibrium pressure. The laboratory was cooled to the test temperature by regulating the room temperature. Water in the degassing tank was deaerated by vacuum boiling overnight and then pressurized with methane to about 2 bar. The flow loop was evacuated to about 1 mbar with the vacuum pump. By connecting the flow loop and the degassing tank, water from the degassing tank was sucked into the flow loop because of the underpressure in the loop and the pressurized degassing tank. Water was drained from the separator until the liquid level was equal to the height of the lowest view-ports. Thus, a gas pocket was left in the separator for accumulation of produced hydrate. The volume of the drained water was measured and the total volume of water in the flow loop was calculated.

Then, while stirring at 400 RPM and circulating at 20 litre/min, gas (either methane or natural gas mixture) was injected into the reactor to a pressure about 5 bar lower than the hydrate equilibrium pressure. The amount of gas injected was recorded. The flow loop was left overnight for gas dissolution with a stirring rate of 400 RPM and a liquid circulation rate of 20 litre/min. The pressure usually decreased only a few bar, due to the low solubility of the gas in water, before leveling out at the saturation pressure.

The following day, stirring and circulation were stopped and the back pressure regulator set to the experimental pressure. Then, gas was injected until the pressure in the loop equaled the experimental pressure. The amount of gas injected was recorded. The system was allowed to reach temperature and pressure equilibrium, which usually was accomplished within 15 minutes, before the experiment was started.

Data acquisition was started. The experiment was initiated by simultaneously switching on the stirring, the heat exchanger cooling system, the circulation pump and the displacement pump at the separator, and opening valves for gas injection and gas vent.

Gas injection was provided by supplying a higher pressure, usually between 5 and 15 bar higher, in the gas injection line (at Pg-1D) than in the reactor (at Pw-1D).

The pressure in the gas injection line was regulated at the gas service panel with the pressure-reducing valve. The gas booster was *not* used since this would have caused fluctuations in the gas injection rate. Thus, the pressure in the gas bottles had to be at least 15 bar higher than the experimental pressure during the experiment. In most experiments, the gas injection rate exceeded the maximum measurable rate in VFMg-1D, but the display showing the gas vent rate (VFMg-2D) gave an indication of the stability and the level of the gas flow rates. The gas injection rate was calculated from the pressure drop in the gas bottles (either Pp-1 or Pp-2) using the real gas law. The calculation is described in more detail in Section 4.6. The experiment was continued for about 15 minutes unless the gas vent line was blocked. Operation of the system and system behaviour during experiments are described further in Section 4.5.

After the experiment was terminated, gas was slowly vented out from the top of the separator until the pressure was about 5 bar lower than the hydrate equilibrium pressure. The hydrates were allowed to dissociate. Sometimes the pressure was taken down to 1 atm and the water changed. This was done when the type of gas was to be changed, or when the separator was full of hydrates so that the pressure had to be reduced by draining water from the separator and the reactor to avoid water in the gas vent line.

4.5 Experimental runs

Each experiment was performed at steady-state conditions. In experiments where stable gas flow rates developed rapidly, the gas injection rate was shifted once and sometimes twice. Based on experience, about 2 minutes were considered enough time for one injection rate. Two experimental runs, one satisfactory stable and one relatively unstable, are shown in Figure 4.3 and Figure 4.4, respectively.

Methane gas bottles and natural gas mixture bottles had an initial pressure around 200 bar and 100 bar, respectively. Stable gas injection rates were obtained by applying constant pressure drop between the pressure-reducing valve at the gas panel and the reactor pressure. Experiments with the natural gas mixture at 90 bar were challenging (Figure 4.4). Maximum overpressure was 10 bar and the pressure declined rapidly as the gas bottle was emptied. Consequently, the gas

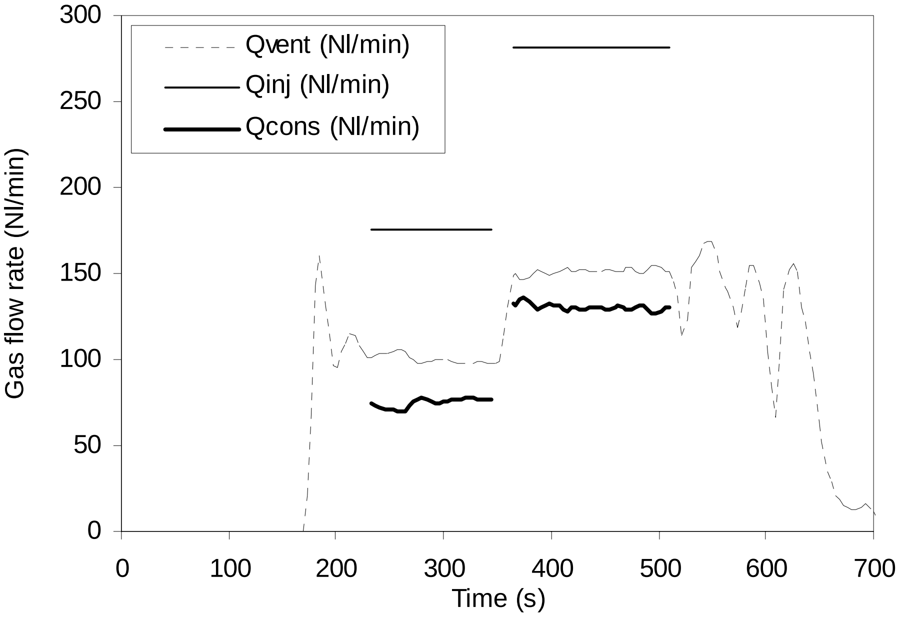

Figure 4.3 Gas flow rates in experiment 7a with methane gas at 70 bar.

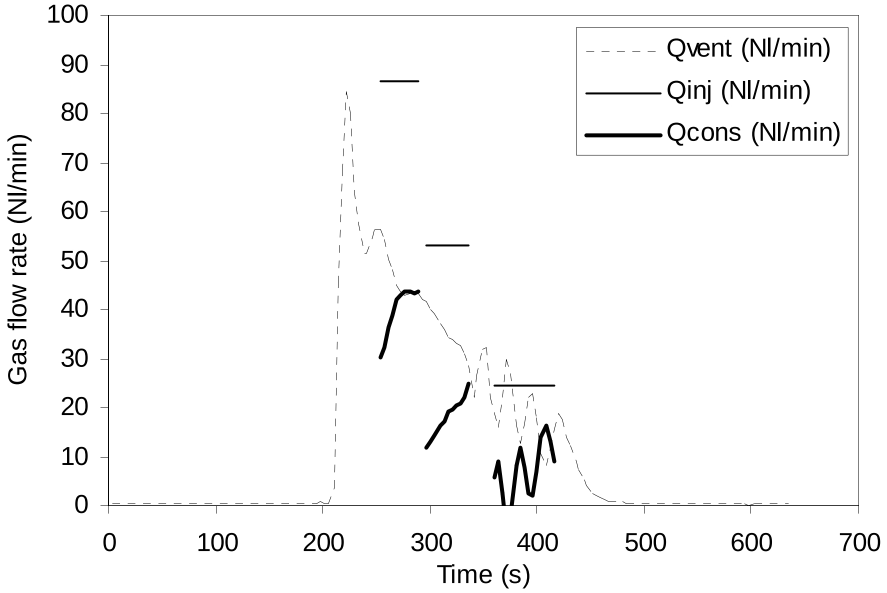

Figure 4.4 Gas flow rates in experiment 6b with natural gas mixture at 90 bar.

injection rate became unstable, making steady-state operation difficult. A constant gas injection rate was usually not obtained.

The experiments were planned to run for several minutes, however, the gas vent line tended to block after a few minutes, often because the back pressure regulator contained moist gas and closed. Hydrate plugs may also have occurred, however, the gas vent line was heated to avoid this problem. Also, many experiments were stopped early to avoid water in the vent line coming from overflow of hydrates in the separator. Experiments performed at high pressure (typically 90 bar) were more difficult to control than experiments at lower pressure (typically 70 bar), mostly because the hydrate formation rate was higher so that the separator was filled faster.

During some experiments, the gas vent rate dropped slightly even if a constant gas injection rate was maintained, probably because water condensed in the gas flow meter VFMg-2D. Moist gas from the separator continuously flowed through the gas vent line and the flow meter.

4.6 Analysis

The recorded data from each experiment were analyzed using MS Excel. Pressures, temperatures and gas flow rates were plotted against time, and the time interval or intervals with a linear gas bottle pressure drop and a stable gas vent rate were identified.

The Fortran-program Bottle (Parlaktuna, 1998) was used to calculate the average gas injection rate from the pressure drop in the gas bottle (either Pp-1 or Pp-2) by using the real gas law. The pressure drop, the gas bottle volume and the average bottle temperature were input to the program. The gas bottle volume was found by weighing the gas bottle at maximum pressure and measure the pressure and the temperature in the bottle. The empty bottle was weighed, and the initial gas volume in the bottle was calculated. The gas bottle temperature was measured with a thermometer on the gas bottle outside wall.

The measured gas vent rate (VFMg-2D) was corrected for current pressure, temperature and gas composition by multiplying with a factor calculated using

Flow Calculations (1994). The gas consumption rate was found by subtracting the corrected gas vent rate from the calculated gas injection rate for each data recording. The average gas consumption and vent rates and the average reactor temperature were calculated for the selected time interval. Also, the error in the gas consumption rate with contributions from errors in the gas injection rate and the gas vent rate was calculated. Appendix B describes the calculation of the error in the gas consumption rate and the calculation of the gas injection rate in more detail.

URN:NBN:no-3342

5
Experimental results

The rate of hydrate formation has been measured under different conditions by varying pressure, temperature, stirring rate, gas injection rate and gas composition. In this chapter, the rates of methane hydrate formation and natural gas hydrate formation are presented.

Parlaktuna and Gudmundsson (1998a, 1998b) measured the rate of hydrate formation in the hydrate laboratory at NTNU. These experiments and results, hereafter called previous experiments and results, were used together with the present results in modeling of the hydrate formation rate (Chapter 7 and Chapter 8). In both previous and present experiments, the rate of gas consumption was considered to represent the rate of hydrate formation. By assuming a certain degree of filling in the hydrate cages, the rate of hydrate formation can be found from the gas consumption rate, however this was not emphasized here.

Typical previous results are presented in Section 5.1. The experimental conditions for the present experiments are presented in Section 5.2. The present results from methane hydrate experiments are presented in Section 5.3 and compared with the previous results. In Section 5.4, the present results from natural gas hydrate experiments are presented and compared with similar results from previous experiments and with present methane hydrate results from Section 5.3. The results of each experiment are presented in Appendix A. The overall errors in the present results were calculated applying the procedure described in Appendix B.

URN:NBN:no-3342

5.1 Previous results

Parlaktuna and Gudmundsson (1998a, 1998b) performed experiments to investigate the effects of stirring rate, gas injection rate, pressure and subcooling on the rate of hydrate formation (the gas consumption rate). Experiments were carried out using both methane gas and a natural gas mixture with the same composition as the gas mixture in the present experiments.

The experimental conditions were:

- Pressure: 70, 80 and 90 bar
- Subcooling: from 2 to 8 °C
- Stirring rate: 0, 200, 400, 800, 1600 RPM
- Gas injection rate: from 7.95 to 110.25 Nl/min
- Liquid circulation rate: 20 litre/min

The effects of gas injection rate and pressure are shown in Figure 5.1, the effects of gas injection rate and subcooling in Figure 5.2, and the effects of gas injection rate and stirring rate in Figure 5.3. In Figure 5.4, the results of methane gas and natural gas mixture experiments at similar conditions illustrate the effect of gas composition. From the previous results, the following trends are observed:

- The gas consumption rate is proportional to the gas injection rate.
- The gas consumption rate seems to increase with pressure, however, the trend for 90 bar compared to 80 bar is unclear.
- A slight increase in consumption rate with subcooling is observed, however, the effect is small compared to the effect of gas injection rate.
- The gas consumption rate increases with stirring rate, but the effect is relatively small compared to the effect of gas injection rate. At 0 RPM, the consumption rate is different from zero.
- The gas consumption rate is slightly higher for methane gas than for natural gas mixture at similar conditions.

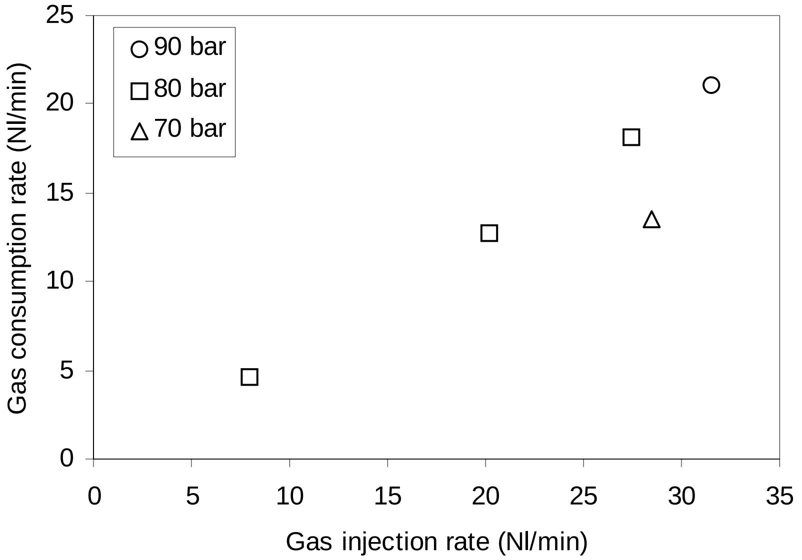

Figure 5.1 Methane gas consumption rate as a function of gas injection rate at 70, 80 and 90 bar. Subcooling was 2 °C and stirring rate was 400 RPM.

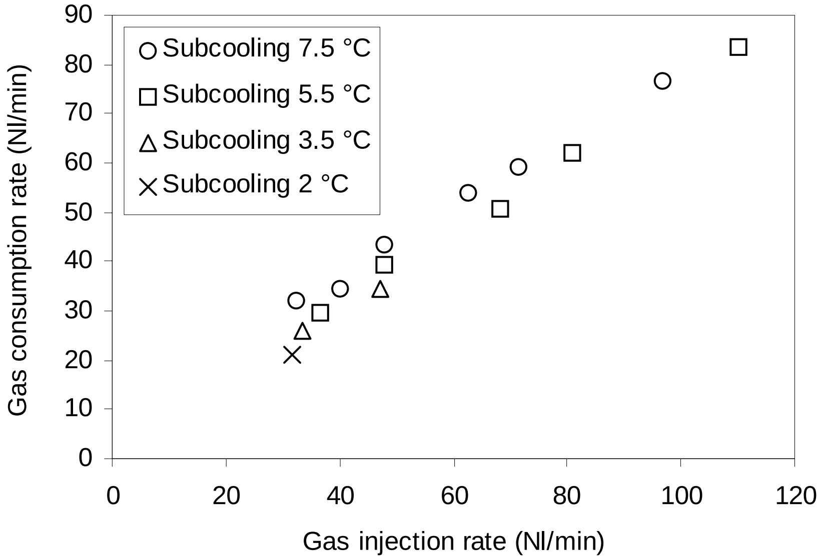

Figure 5.2 Methane gas consumption rate as a function of gas injection rate at 7.5, 5.5, 3.5 and 2 °C subcooling. Pressure was 90 bar and stirring rate was 400 RPM.

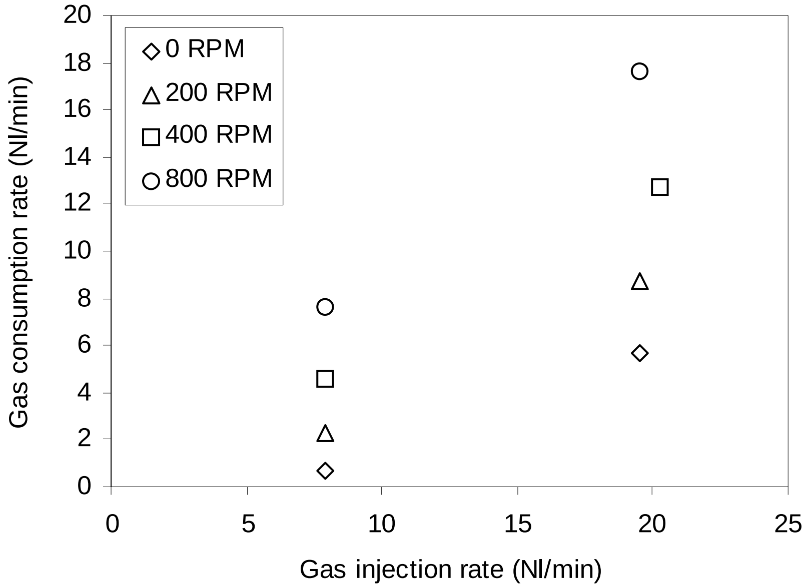

Figure 5.3 Methane gas consumption rate as a function of gas injection rate at 0, 200, 400 and 800 RPM. Pressure was 80 bar and subcooling was 2 °C.

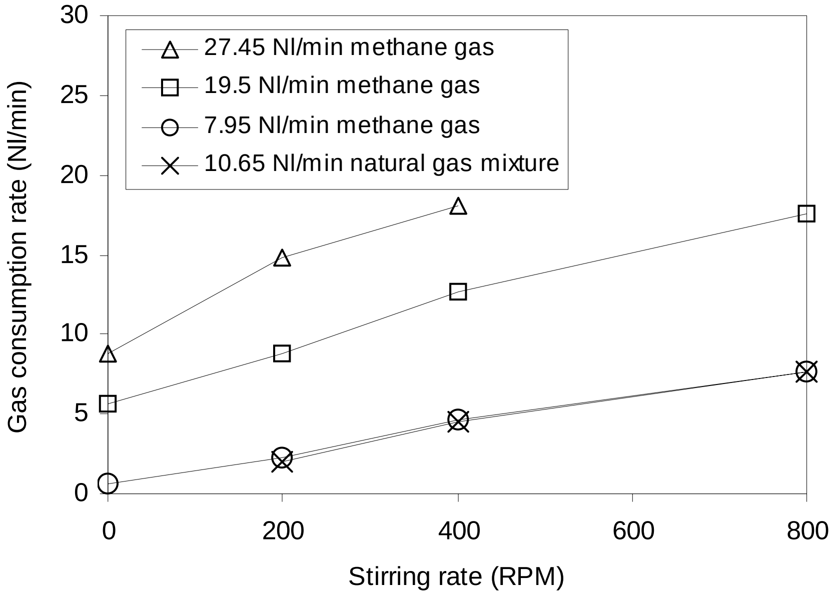

Figure 5.4 Methane gas and natural gas mixture consumption rates as a function of stirring rate at 80 bar and 2 °C subcooling.

5.2 Experimental conditions

The experimental conditions for the present experiments with methane gas and natural gas mixture are presented in Table 5.1 and Table 5.2, respectively. The pressure and temperature conditions together with the hydrate equilibrium curves are illustrated in Figure 5.5.

The water in the rig was sometimes changed (see Section 4.4). Equal water numbers in Table 5.1 indicate that the experiments were carried out with the same water. The same indicator type is used in Table 5.2, but equal water numbers in the two tables does *not* refer to the same water.

The subcooling is the difference between the hydrate equilibrium temperature for the gas composition used and the average reactor temperature. The hydrate equilibrium temperatures for both methane hydrate and natural gas mixture hydrate at 48, 70, 85 and 90 bar were calculated using CSMhyd (1998). For the natural gas mixture experiments, higher temperatures were chosen to obtain subcooling similar to the subcooling in the methane experiments (Figure 5.5).

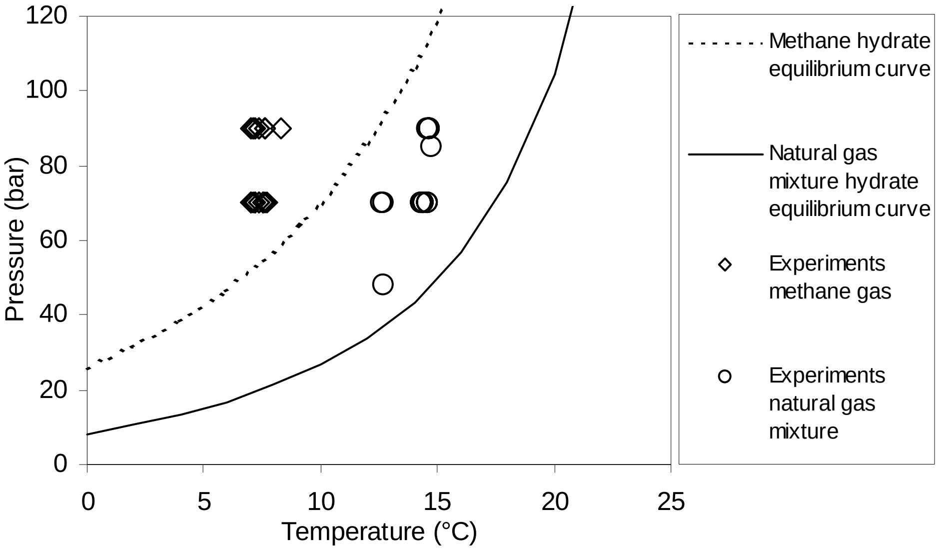

Figure 5.5 Hydrate equilibrium curves for methane gas and natural gas mixture (CSMhyd, 1998). Circles and squares show the pressure and temperature conditions at all the present experiments.

Table 5.1. Experimental conditions in methane hydrate formation experiments (a-experiments).

Exp. no.	Water no.	Pressure (bar)	Temperature (°C)	Sub-cooling (°C)	Stirring rate (RPM)	Gas injection rate (Nl/min)
1a	1	70	7.1	3	400	161
2a	1	70	7.5	2.6	400	207.2
3a	1	70	7.2	2.9	400	209.1, 92.1
4a	1	70	7.5	2.6	400	280.7
5a	2	70	7.4	2.7	400	237.1
6a	2	70	7.4, 7.5	2.7, 2.6	400	164.2, 221.9
7a	2	70	7.6, 7.7	2.5, 2.4	400	175.1, 281.7
8a	2	90	7.4	5.1	400	215.6
9a	2	90	7.6	4.9	400	228.8
10a	3	70	7.2	2.9	400, 600	196.4
11a	3	90	7.1	5.4	400	114.4
12a	3	90	7.2, 7.6	5.3, 4.9	400	190.1, 153.0
13a	4	90	8.3	4.2	400	233.6
14a	4	90	7.1	5.4	400	126.6
15a	4	90	7.6	4.9	400	107.6
16a	5	90	7.0	5.5	400	251.0
17a	6	90	7.0	5.5	400	339.0
18a	6	70	7.0	3.1	400, 800	141.2
19a	6	90	7.4	5.1	800, 200	49.1
20a	6	90	7.2	5.3	400	250.7

Table 5.2. Experimental conditions in natural gas mixture hydrate formation experiments (b-experiments).

Exp. no.	Water no.	Pressure (bar)	Temperature (°C)	Sub-cooling (°C)	Stirring rate (RPM)	Gas injection rate (Nl/min)
1b	1	70	12.6, 12.7	4.9, 4.8	400	48.6, 69.9
2b	1	48	12.7	2.1	400	89.1
3b	2	90	14.6	4.9	400	61.1
4b	3	70	14.4, 14.3	3.1, 3.2	400	79.9, 154.5, 163.1
5b	3	70	14.4	3.1	400	41.4, 89.5
6b	3	90	14.6, 14.7	4.9, 4.8	400	26.6, 57.5, 93.6
7b	3	70	14.6	2.9	400	60.5, 122.9, 192.9
8b	3	70	14.4	3.1	400	71.7
9b	4	85	14.7	4.1	400	32.5

In all the experiments, the liquid circulation rate provided by the pump was 20 litre/min. With a reactor volume of 9.5 litre, this corresponded to a residence time of 28.5 seconds.

The maximum gas injection rate was limited by the range of the gas flow meter at the gas vent line. The flow meter VFMg-2D measured gas flow rates from 0 to about 165 Nl/min of methane gas. Also, the separator filled rapidly with hydrates at the high gas injection rates limiting the maximum gas injection rate.

The repeatability of the experiments was investigated using similar gas injection rates in different experiments. For methane gas, experiments 4a and 7a, and 16a and 20a served this purpose. For natural gas mixture, experiments were not repeated.

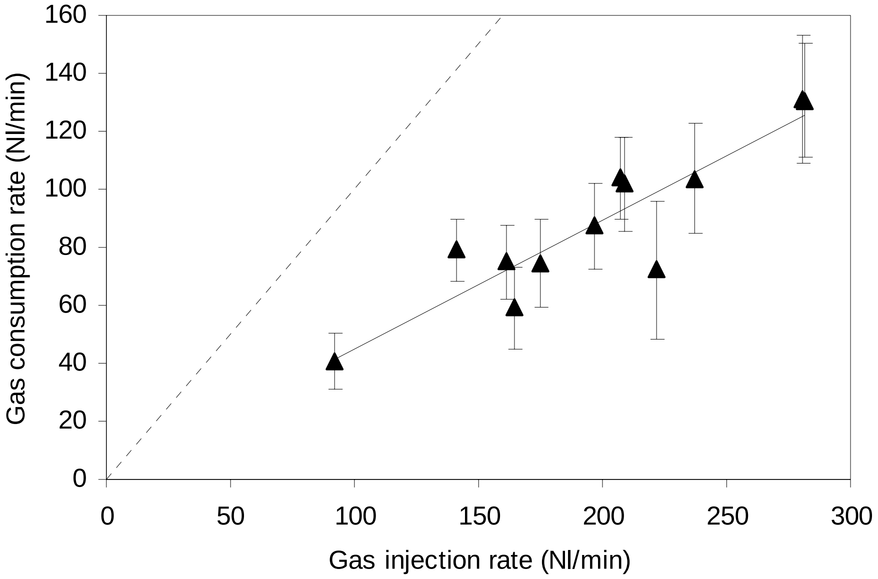

Figure 5.6 Methane gas consumption rate as a function of gas injection rate at 70 bar. Stirring rate was 400 RPM, and reactor temperature was about 7 °C. The dashed line represents the theoretical situation where the gas injection rate equals the gas consumption rate. The solid line is the linear best fit line for the data.

5.3 Methane gas results

The results of methane gas experiments at 70 bar demonstrated that the gas consumption rate was proportional to the gas injection rate (Figure 5.6). The overall errors in the gas consumption rates, indicated with error bars, were calculated using the procedure in Appendix B. The dashed line represents a theoretical situation where the whole gas volume injected would be converted to hydrates.

Two experiments at 70 bar with injection rates at about 208 and 280 Nl/min were repeated. In Figure 5.6, the data points for the repeated experiments almost coincide with the data points for the first experiments. Thus, the repeatability of the experiments was regarded satisfactory.

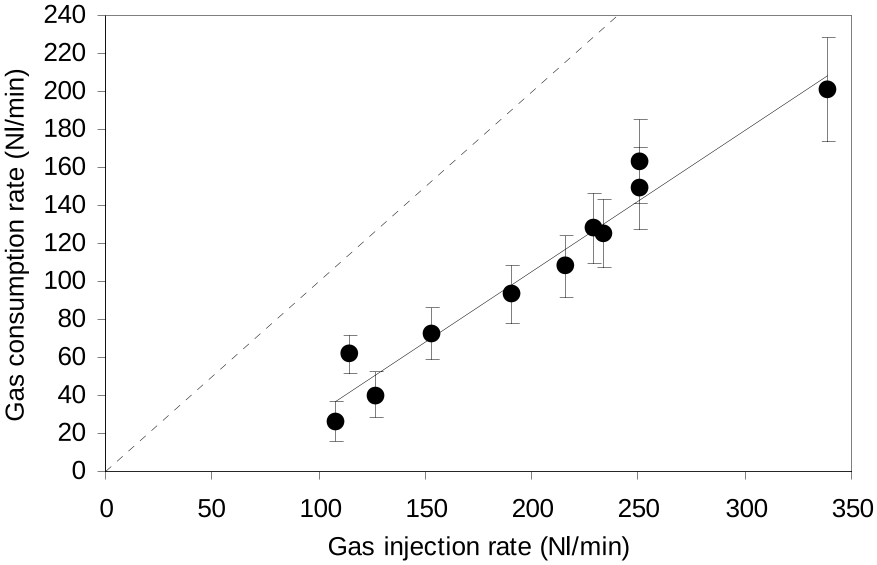

Figure 5.7 Methane gas consumption rate as a function of gas injection rate at 90 bar. Stirring rate was 400 RPM, and reactor temperature was about 7 °C. The dashed line represents the theoretical situation where the gas injection rate equals the gas consumption rate. The solid line is the linear best fit line for the data.

Experiments performed at 90 bar (Figure 5.7) also demonstrated that the gas consumption rate was proportional to the gas injection rate. However, the gas consumption rate seemed to approach zero when the injection rate was about 50 Nl/min. This is discussed below when comparing the results with the previous 90 bar results (Parlaktuna and Gudmundsson, 1998a, 1998b).

At 90 bar, the repeatability was demonstrated at injection rates around 230 and 250 Nl/min. The data points from the repeated experiments are close to the data points of the first experiments. The repeatability is satisfactory.

The effect of pressure on the gas consumption rate was illustrated by replotting, in Figure 5.8, the two data sets in Figure 5.6 and Figure 5.7. The gas consumption rate increased somewhat with pressure at high gas injection rates. The effect of pressure at the lowest injection rates is commented on below together with the previous experiments at 90 bar.

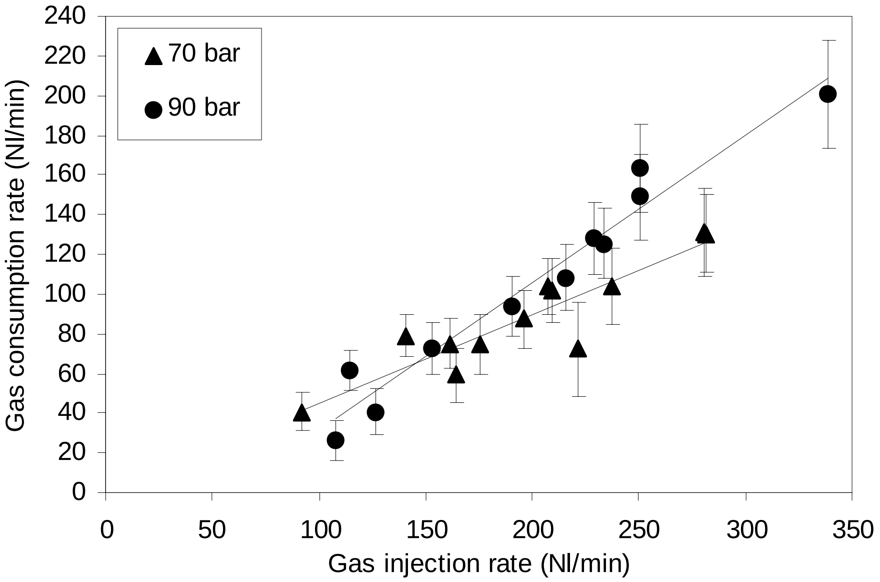

Figure 5.8 Methane gas consumption rate as a function of gas injection rate and pressure.

In addition to the effects of gas injection rate and pressure, comments can be made about the water memory effect (thermal effect on ordering of water molecules) and the effects of temperature and stirring rate. In most experiments, hydrates were produced from water that had a history as hydrate former. Experiments 1a, 5a, 10a, 13a, 16a and 17a were expected not to experience any water memory effect since the water had not previously been forming hydrates. No difference in the onset of hydrate formation was observed between experiments with water that had and water that had not formed hydrates earlier. Thus, any possible difference in the ordering of water molecules did not affect the production of hydrates. This was expected because tap water was used and no effort was made to clean the rig before each experiment, meaning that nucleation was promoted sufficiently in water with and without a history as a hydrate former.

The effect of temperature was not investigated separately, but the temperature varied from run to run with a range of 1.3 °C. This variation in temperature could not explain some of the deviations from the best fit line neither at 70 bar nor at 90 bar. Thus, no significant effect of subcooling within this range could be observed either. In contrast, a small effect of subcooling was found in the previous results

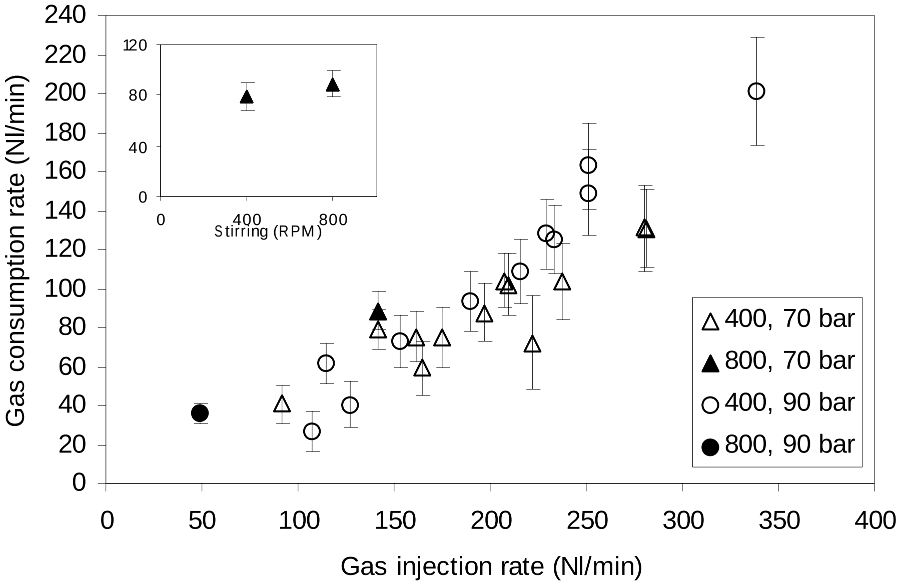

Figure 5.9 Methane gas consumption rate as a function of gas injection rate at around 7 °C. Other conditions are listed in the legend. The graph in the upper left corner shows the gas consumption rate with stirring rate at a gas injection rate of 141.2 Nl/min (experiment 18a).

(Figure 5.2) where the gas injection rate was low, but where the variation in subcooling was large. In the present results, any effect of subcooling was probably masked in the overall error in the gas consumption rate. Hence, the effect of subcooling was insignificant, and only observable when varying the subcooling several degrees and at low gas injection rates where the errors were smaller.

The stirring rate was varied to confirm previous findings shown in Figure 5.4 (Parlaktuna and Gudmundsson, 1998a, 1998b). In experiment 10a, when stirring rate increased from 400 to 600 RPM, the gas consumption rate *decreased* from 87.3 to 69.7 Nl/min (Figure A.12). Opposite behavior was observed in experiment 18a (Figure 5.9, upper left corner), where an increase in stirring rate from 400 to 800 RPM increased the gas consumption rate from 79.0 to 88.7 Nl/min. In the main graph, the results of experiment 19a carried out at 800 RPM and the results of experiment 18a are plotted with other results at 400 RPM. Based on the previous results (Figure 5.3), it was generally believed that by increasing the stirring rate, the gas consumption rate increased due to more intense mixing of the components in the reactor. The effect of stirring on the consumption rate was observable, but was not as important as the effect of gas injection rate.

Present and previous results from experiments at 70 bar and 6 to 8.3 °C were compared in Figure 5.10. The previous results corresponded well with the present results even with a slight difference in temperature. A linear best fit of both the present and the previous data gave the following correlation:

$$Q_{cons} = 0.443 \cdot Q_{inj} + 0.853 \tag{5.1}$$

indicating that about 44 % of the gas injected was converted hydrate. The regression coefficient was 0.92.

In Figure 5.11, previous data for 90 bar (Figure 5.2) at 5.5 °C subcooling (corresponded to a reactor temperature at 7 °C) were plotted with the present data from Figure 5.7. The proportionality in the previous results was clear, however, the data were shifted to the left compared to the present results. It was not clear whether the discrepancy was due to physically different effects of gas injection rates at high and low injection rates or due to some differences in the experimental procedures. Parlaktuna and Gudmundsson (1998a, 1998b) calibrated the gas flow meter on the gas vent line (VFMg-2D) using the real gas law (Section 4.6), whereas the calibration supplied from the manufacturer together with correction factors for different experimental conditions were used in the present experiments (Section 4.3). In addition, the liquid level of the separator was higher in the previous experiments than in the present experiments. In the present experiments, a lower liquid level was chosen to allow hydrate build-up for a longer time, without blocking of the gas vent line. The difference in the calibration and in the liquid level may explain the discrepancy between present and previous results at 90 bar.

Without considering which data set to trust, a linear best fit of both the present and the previous results at 90 bar gave the following correlation:

$$Q_{cons} = 0.562 \cdot Q_{inj} - 0.0582 \tag{5.2}$$

The slope of the curve indicated a conversion of about 56 % of the gas when producing hydrates at 90 bar. The regression coefficient was 0.89.

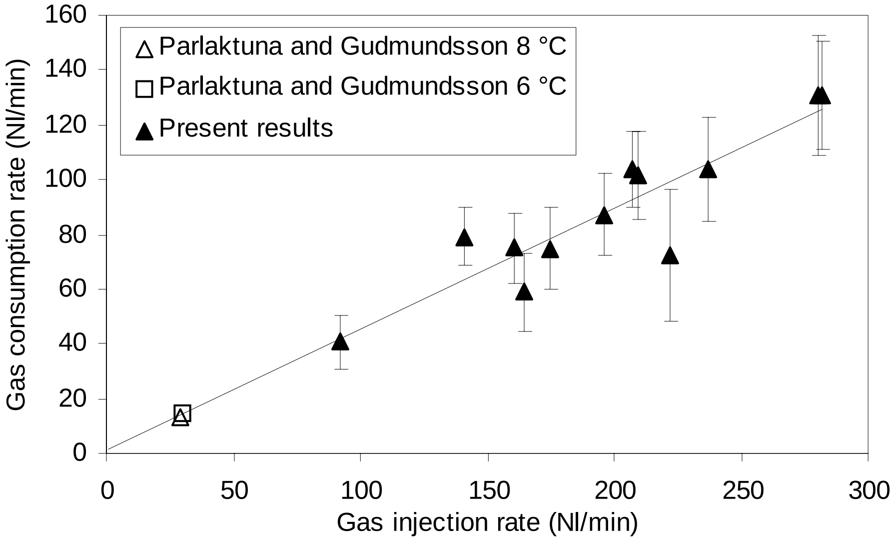

Figure 5.10 Methane gas consumption rate as a function of gas injection rate at 70 bar and 6 and 8 °C. Temperatures for present results were in the range 7.1 to 7.6 °C. The solid line is the linear best fit line for both the present and the previous data.

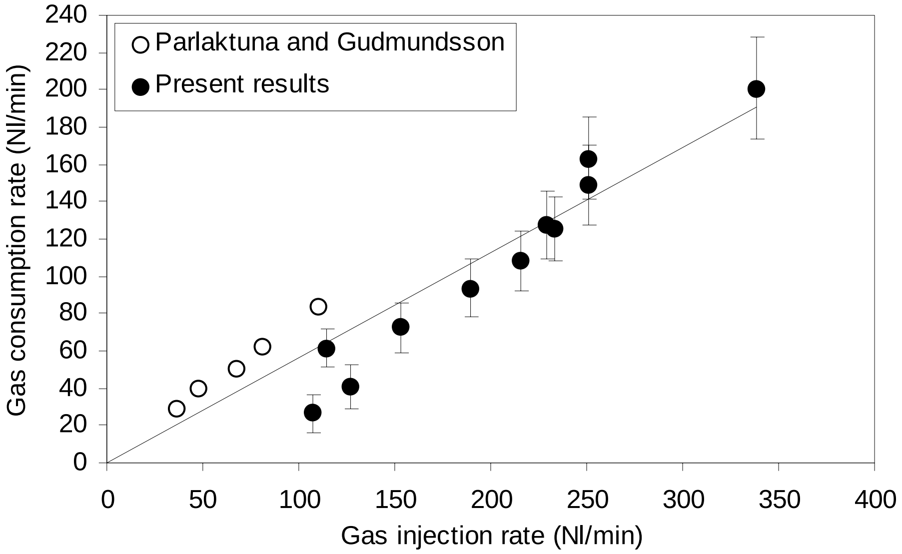

Figure 5.11 Methane gas consumption rates as a function of gas injection rates at 90 bar, 400 RPM and temperatures in the range from 7 °C to 8.3 °C. The solid line is the linear best fit for both the present and the previous data.

5.4 Natural gas mixture results

The results from experiments with natural gas mixture at 70 bar showed the same as for methane gas results, that the natural gas mixture consumption rate was proportional to the gas mixture injection rate (Figure 5.12). The results also showed that about 2 °C change in subcooling had no impact on the gas consumption rate at the present gas injection rates.

Consumption rates as a function of gas injection rate at 48, 85 and 90 bar are shown in Figure 5.13. The 90 bar results, except from the result at 61.1 Nl/min gas injection rate (experiment 3b), were all from experiment 6b (Figure 4.4). In experiment 6b, steady-state operation was not obtained, and therefore, the results were considered unreliable. In experiment 3b (Figure A.25), the gas vent rate was unstable and the result was based on averaging over a short time period. The general performance of the 90 bar natural gas mixture experiments are commented in Section 4.5.

An experiment was carried out at 85 bar as a substitution for 90 bar due to low initial pressure in the gas bottle. A single experiment was carried out at 48 bar to investigate the pressure effect and simultaneously ensure a considerable overpressure. Yet, 48 bar was considered too low for industrial production of hydrates and therefore not relevant in this study. The results at 85 and 48 bar in Figure 5.13, showed that the consumption rate increased with pressure. Hence, the effect of pressure was considered to be similar to what was found for methane gas.

The effect of gas composition is shown in Figure 5.14. Natural gas mixture consumption rates were compared with methane gas consumption rates at 70 bar. All data points seemed to fall into the same linear trend. It must be noted that the conditions were not directly comparable. Methane gas injection rates were generally higher than natural gas mixture injection rates. Similar subcooling was stressed (see Figure 5.5) to compare results with methane gas and natural gas mixture. This resulted in higher experimental temperatures in natural gas mixture experiments than in methane experiments. The difference in temperature was approximately 7 °C. However, as shown in Figure 5.2 and Figure 5.12, the effect of subcooling, and therefore also the effect of temperature, were not significant.

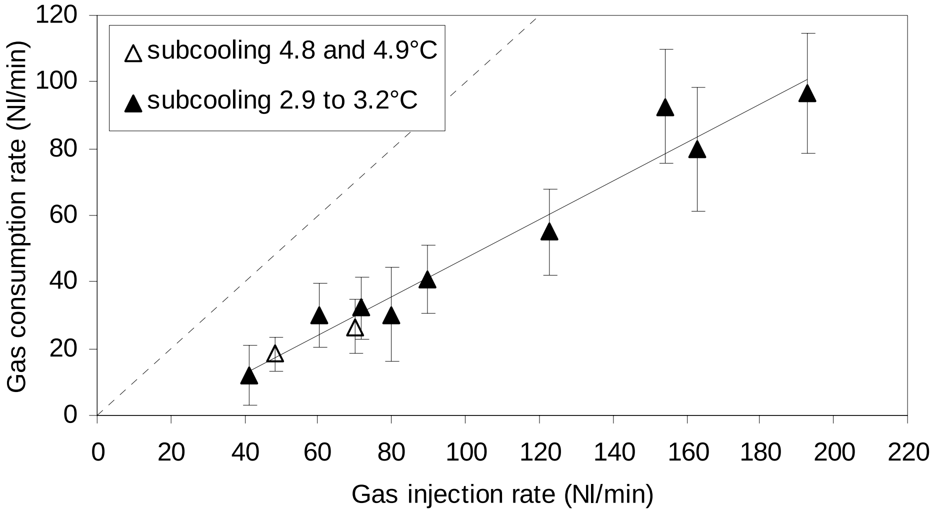

Figure 5.12 Natural gas mixture consumption rate as a function of gas injection rate at 70 bar. The results from experiment 1b (subcooling at 4.8 and 4.9 °C) are shown as hollow triangles. The stirring rate was 400 RPM and the temperature was in the range 12.6 °C to 14.7 °C. The dashed line represents the theoretical situation where the gas injection rate equals the gas consumption rate.

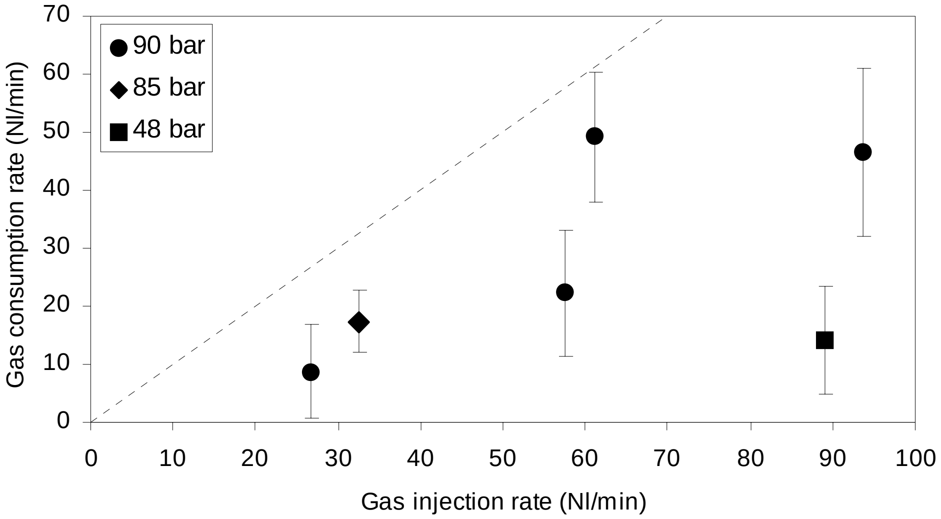

Figure 5.13 Natural gas mixture consumption rate as a function of gas injection rate at 48, 85 and 90 bar. Stirring rate was 400 RPM and temperature ranged from 12.7 to 14.6 °C. Dashed line illustrates maximum theoretical conversion.

Previous results (Parlaktuna and Gudmundsson, 1998a, 1998b) indicated that methane gas consumption rates were slightly higher than natural gas mixture consumption rates. At equal pressure and subcooling, and gas injection rates at 7.95 and 10.65 Nl/min for methane gas and natural gas mixture, respectively, the consumption rates were identical (Figure 5.4). For the present experimental conditions, such a difference would probably lie within the accuracy of the measurements. Hence, it was concluded that the difference between methane and natural gas mixture consumption rates at the present conditions was insignificant.

In the present natural gas mixture experiments, the gas injection rates were considerably higher than in the previous experiments, nevertheless, Figure 5.15 shows a good agreement between the results at 70 bar. A linear best fit of the present data and the previous data points with 3.5 and 4.5 °C subcooling gave the following correlation:

$$Q_{cons} = 0.562 \cdot Q_{inj} - 8.81 \tag{5.3}$$

The regression coefficient was 0.97. This result indicates that about 56 % of the natural gas mixture was converted to hydrates at 70 bar, which was equal to the conversion for methane gas at 90 bar. However, forcing the linear best fit line in Equation 5.3 to intersect at zero resulted in a slope equal to 0.49, which was similar to the slope for methane gas at 70 bar in Equation 5.1. A comparison of present and previous results at 90 bar was not performed since the present results at 90 bar were unreliable.

The experimental results in Appendix A show that the gas consumption rate maintained at the same level during an experiment if not considering the fluctuations. This holds for both methane gas and natural gas mixture experiments. A slight decrease in the gas vent rate in some of the experiments, and thereby an increase in the gas consumption rate, was explained by moisture in the vented gas (Section 4.5). The previous results (Parlaktuna and Gudmundsson, 1998a, 1998b) demonstrated that the gas consumption rates maintained the same level for up to two hours. The previous experiments ran for a longer period of time than the present experiments because of lower gas injection rates. During an experiment, the produced hydrate crystals were carried with the water phase and recirculated

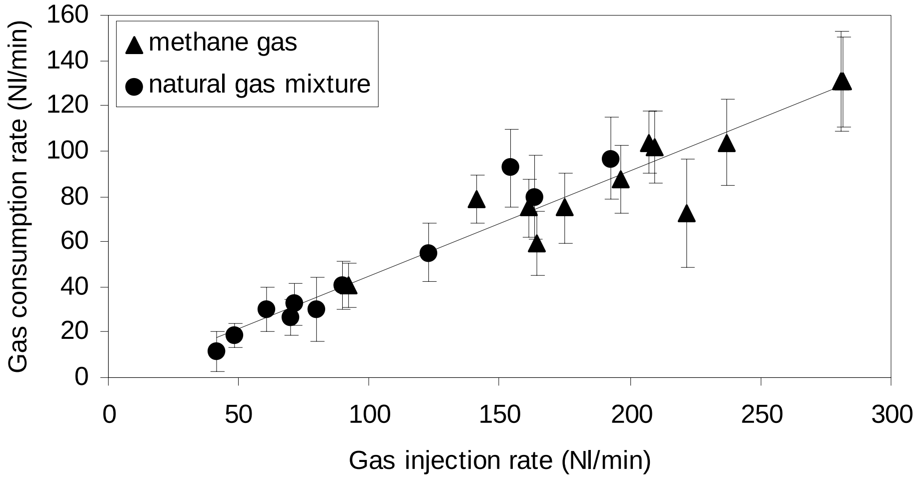

Figure 5.14 Gas consumption rate for methane gas and natural gas mixture as a function of gas injection rate. Pressure was 70 bar and stirring was 400 RPM. For methane, subcooling ranged from 2.4 °C to 3.1 °C. For natural gas mixture, subcooling ranged from 4.9 °C to 2.9 °C.

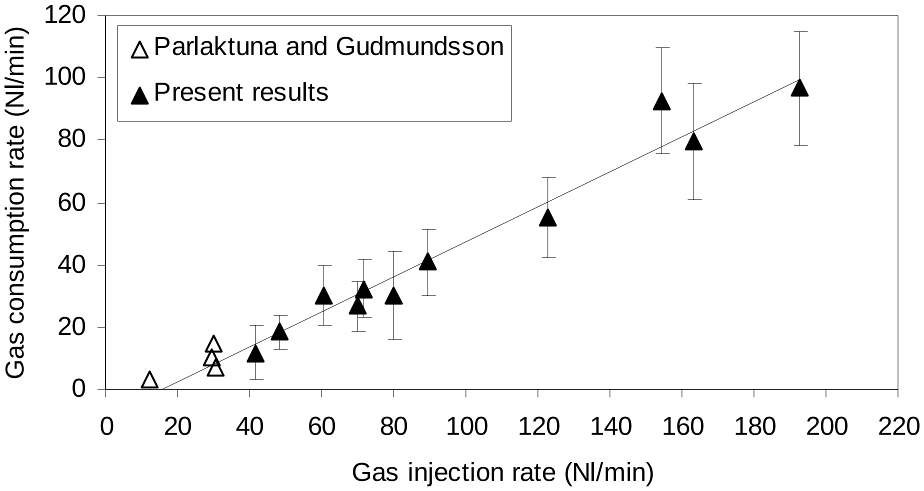

Figure 5.15 Natural gas mixture consumption rate as a function of gas injection rate. Pressure was 70 bar and stirring rate was 400 RPM. For the three results at approximately 30 Nl/min gas injection rate (Parlaktuna and Gudmundsson), the subcooling at the lowest to the highest point was 4.5, 6.5 and 8.5, respectively. The subcooling for the point at about 12 Nl/min was 3.5 °C.

back to the reactor. Hence, the increasing hydrate crystal concentration did not affect the gas consumption rate.

5.5 Errors in gas consumption rate

The overall error in gas consumption rate was calculated according to the description in Appendix B. The calculated overall error for methane gas was usually about ±15 % of the rate itself, and up to ±30 % for some experiments. For natural gas mixture, the overall error was usually about ±30 % with a few overall errors in the range 50-90 %.

The main contribution to the overall error was the error in the calculated gas injection rate. The error in the gas injection rate included errors in the measured pressure and temperature and errors in the calculated gas bottle volume and z-factor. The significant contributions were the errors in gas bottle volume and z-factor. As presented in Appendix B, the given error in gas bottle volume of 5 % (Henriksen, 2001) was reduced by determination of the gas bottle volume by weighing. The errors in pressure, temperature and z-factor contributed to the error in the gas bottle volume. The error in the natural gas mixture bottle volume was larger than the error in the methane gas bottle volume due to only about 100 bar initial pressure in the natural gas mixture bottles. The error in the measured gas vent rate contributed little to the overall error in the gas consumption rate.

For the experiments where gas flow rates were not fully stabilized, errors from averaging over a time period contributed significantly to the overall error in consumption rate. The instability in the experiment (Figure A.28), and the short time period for averaging (Figure A.25) affected the errors in the 90 bar results in Figure 5.13.

Leakages were potential sources of error in addition to the errors identified in the calculation. Before each experiment, the flow loop including gas flow lines were pressurized and leakages could be identified. Several leakages, all of them in the gas injection line, were detected and tightened. Leakages were not observed in the flow loop and in the gas vent line. A leakage in the gas injection line leads to an overestimation of the gas injection rate, and thereby, an overestimation of the gas consumption rate.

5.6 Concluding remarks

The experimental results have been presented. Gas consumption rates were measured under various conditions, and the following were found:

- Gas consumption rate increased proportionally with the gas injection rate, both for methane gas and natural gas mixture. When the gas injection rate approached zero, the gas consumption rate approached zero.
- Gas consumption rate increased with increased pressure, both for methane gas and natural gas mixture.
- Gas composition did not affect the gas consumption rate.
- Stirring influenced the gas consumption rate, but not to the same extent as gas injection rate and pressure. Previous experiments and most of present experiments showed an increase in consumption rate with increased stirring rate.
- In present experiments, subcooling did not influence the gas consumption rate, however, in previous experiments, a slight increase with increased subcooling was observed.
- An increasing concentration of produced hydrate crystals did not influence the gas consumption rate.
- Overall error in gas consumption rate for methane gas and natural gas mixture was for most experiments about 15 % and 30 %, respectively.

6

Hydrate crystal morphology

Information about morphology and particle size distribution is desirable in design of reactors for crystallization processes, especially to control the characteristic parameters of the product. By using microscopic imaging, the hydrate crystal size and appearance were investigated. Originally, the goal was to obtain enough information to determine the particle size distribution, however, the chosen experimental equipment was found not to give such quantitative information at this stage. Nevertheless, the equipment was found suitable for a rough determination of the hydrate crystal size as well as for qualitative information about shape and behaviour of the crystals.

The produced hydrate crystals were studied by using a microscope set-up and a high pressure flow cell connected to the flow loop. The flow cell and the microscope as well as the experimental procedure are described in Section 6.1. Images are shown and commented on in Section 6.2.

6.1 Experimental set-up and procedure

A schematic drawing of the flow cell and the microscope is shown in Figure 6.1. The flow cell of stainless steel was connected to the test unit of the flow loop (Section 4.1). The hydrate slurry flowed vertically downward in parallel to two sapphire windows within the flow cell. The sapphire windows were 9 mm thick

URN:NBN:no-3342

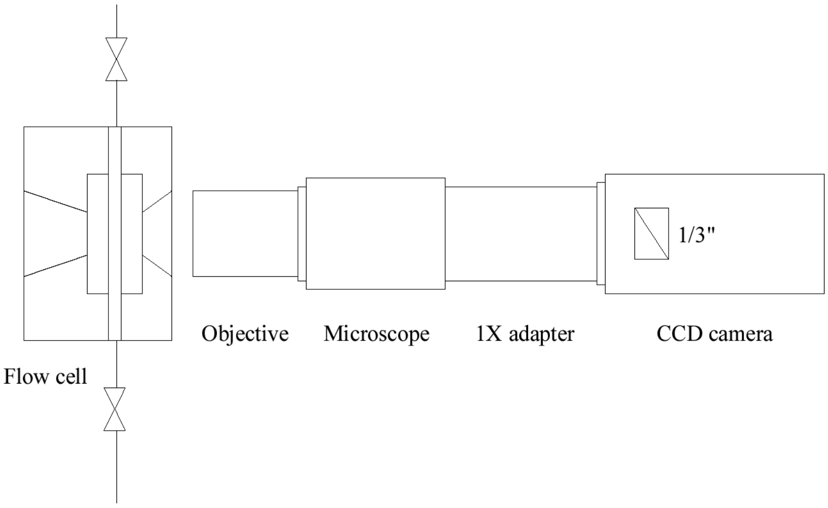

Figure 6.1 Schematic drawing of high pressure flow cell and microscope (not to scale).

and were pretreated to avoid reflections. The pretreatment consisted of a so-called “c”-axis orientation at high temperature and was performed by Sanchez Technologies SA. The space between the sapphire windows was 4 mm.

The microscope from Navitar consisted of a 20 X objective lens (type 0.42 NA 1-60228) with 20 mm working distance, a 1 X adapter and a 6.5 UltraZoom microscope with 3.5 mm fine focus (type 1-60191). A 150 W Fostec light source could be coupled to the microscope via an optic fibre. However, it was found that a 12 V halogen lamp placed to the left of the flow cell in Figure 6.1 provided images of higher quality. The halogen lamp was used in the experiments. A 1/3” CCD-camera (Sanyo VCC-3972 P) was connected to the microscope. The images were recorded on a Sony VHS Time Lapse video tape recorder, and a 14” Sony colour monitor was used to display the images. With a MRT VideoPort framegrabber PC-card, images were transferred to a personal computer and could be analyzed using the image analysis program Optimas 6.1. At the monitor, this set-up provided a magnification between 414 X and 2670 X and a field of view (diagonal) between 0.90 and 0.14 mm. This means that for a field of view at 0.90 mm, the diagonal of the monitor corresponded to approximately 90 particles of 10 μm in diameter in line at the diagonal. In this case, the magnification was 414 X.

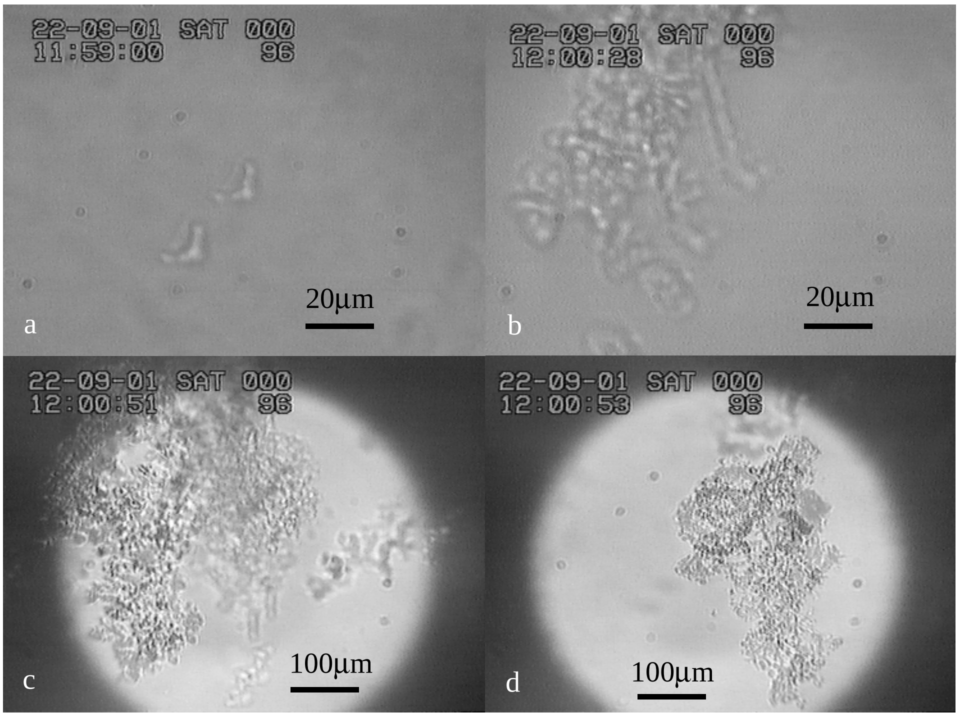

Figure 6.2 Natural gas mixture hydrate crystals at 2670 X (a) (b) and 414 X (c) (d) magnification. Experiment 4b.

During an experiment, the slurry was directed into the flow cell and two valves were closed to bring the fluid inside the flow cell to rest. When the content of the flow cell volume stopped moving, the valves were opened and the slurry flowed through the cell until the next volume was captured. The content of the flow cell was continuously recorded, and opening and closing of the flow cell volume were repeated several times during an experiment.

6.2 Results on hydrate morphology

Hydrate crystals produced from natural gas mixture at 70 bar are shown in Figure 6.2. Images (a) and (b) with 2670 X magnification show two different hydrates captured with about one and a half minute space of time. Images (c) and (d) with 414 X magnification are taken two seconds apart and are probably showing the same hydrates.

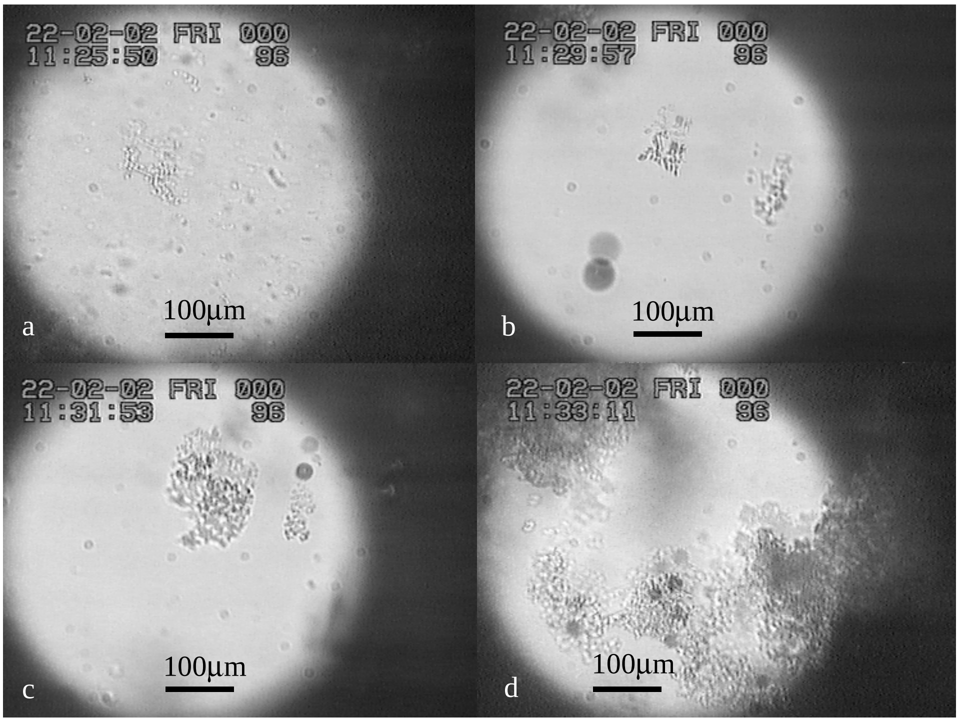

Figure 6.3 Natural gas mixture hydrates at 414 X magnification. Experiment 9b.

The hydrate crystal in Figure 6.2a consists of one main unit of about 5 x 10 µm in size. In Figure 6.2b, crystal units of this size are connected to form an agglomerate, indicating that an agglomerate consists of elongated crystals that are about 5 µm in diameter and 10 µm long. An upper branch in the agglomerate seems to consist of four consecutive crystal units. In 414X magnification (c,d), the agglomerates look like semi-transparent snow flakes in water. The images at 414X magnification resemble Bylov's (1997) images taken shortly after nucleation with a magnification of about 25 X. As reviewed in Section 2.7, hydrate crystal sizes between 7 and 12 µm (Bylov, 1997) and 10 and 22 µm (Herri *et al.*, 1999) have been measured.

A series of images in Figure 6.3, taken within a few minutes in experiment 9b, shows the same type of semi-transparent agglomerates. The series illustrates how agglomerates increased in size during an experiment from tens to hundreds of micrometers. In Figure 6.3a, the agglomerate consists of fewer crystals compared to the agglomerate in Figure 6.3c. Typically, the field of view was totally covered with agglomerates after a while.

In Figure 6.3d, gas bubbles are trapped inside the agglomerate. Gas bubbles were sometimes observed during recording of the hydrate slurry, which means that some gas was transferred along with the hydrate slurry. Also, the presence of the gas bubbles suggests that the gas could exist as a bubble without immediately being dissolved in the water phase or converted to hydrate.

The agglomerates were exposed to turbulence and shear when being recirculated in the flow loop. It was observed that the shear in the flow cell after the valves were closed, but before the fluid was brought to rest, was not enough to break the agglomerates. Whether the agglomerates were broken or not when the slurry flowed through the cell could not be observed because the velocity through the cell was too high.

Unfortunately, the contours in the images are reflected, as in Figure 6.2a for example. In fact, the crystal itself cannot be distinguished from the reflection. The reflections were attempted removed by improving the parallelity of the sapphire windows by modifying the flow cell, and by giving the sapphire windows the high temperature pretreatment. These attempts had no effect on the visibility of the reflection or the distance between the crystal and its reflection. The problem was left unsolved.

7

Empirical model

In this chapter, the relative importance of the effects investigated in Chapter 5 are examined. To study the reactor performance relative to established knowledge, the measured gas consumption rates are connected to parameters used in studies of stirred tank reactors. Gas injection rate was found to be an important parameter as well as pressure. Less important were the effects of stirring and subcooling. The significance of each parameter was found by performing a multiple non-linear regression analysis on the experimental results.

An empirical model was developed based on both the previous experimental results of Parlaktuna and Gudmundsson (1998a, 1998b) and the present experimental results from Chapter 5. Since the experimental results indicated no significant difference between the rates of methane and natural gas mixture hydrate formation, one empirical model was developed.

The method of determining the model is described in Section 7.1. The stirring rate and the gas injection rate were used to calculate parameters relevant in studies of standard stirred tank reactors. This is described in Section 7.2. The empirical model and its fitted parameters are presented in Section 7.3. In Section 7.4, the empirical model is applied to consider the interactions between the investigated effects and to explain the different effects.

URN:NBN:no-3342

7.1 Method

Multiple non-linear regression was preformed using the computer program POLYMATH 5.1 (2002). Experimental data including gas consumption rate, superficial gas velocity, pressure, power consumption and subcooling, one parameter in each column, were input to the program.

As a start, a model equation, where the dependent gas consumption rate was a function of the other independent parameters, was suggested. The model was modified, by trial and error, until simultaneously the sum of squares of errors and the 95 % confidence intervals of the converged parameters were at a minimum. The 95 % confidence interval indicates the precision of the converged parameter and contains the converged parameter 95 % of the time. A 95 % confidence interval corresponds to two standard deviations of the mean value. Converged parameter values and their 95 % confidence intervals were the principal output from the regression.

7.2 Calculation of parameters

The concept of impeller power consumption presented in Section 3.2 and Section 3.4 on page 42 was used to determine the impeller power consumption for each experiment. First, the ungassed (liquid only) power consumption was calculated from the stirring rate by using Equation 3.1 for standard stirred tank reactors:

$$P = N_p \rho N^3 D^5 \tag{7.1}$$

where an impeller power number N_p equal to five, according to Figure 3.3, was used. The density of the reactor medium, a mixture of water, hydrate particles and dispersed gas bubbles, was assumed equal to the density of water since the density of hydrate is close to the density of liquid water and since the presence of gas was accounted for separately. The stirring rate varied from 0 to 800 RPM, or 0 to 13.3 s^{-1}. The diameter of the impeller was 0.076 m.

URN:NBN:no-3342

The impeller power consumption was corrected for the presence of the gas using the gassed power consumption, Equation 3.10 on page 42:

$$P_g = (1 - 12.6 N_{QG}) P \tag{7.2}$$

for flow numbers N_{QG} lower than 0.035. The flow number was lower than 0.035 in all the experiments.

Superficial gas velocity is the volumetric gas flow rate per cross sectional area of the reactor at *in situ* conditions. It was calculated from the gas injection rate with the units Nl/min. Using the experimental pressure and temperature, and z-factor (PVTsim 11.0, 2001), the *in situ* volumetric gas flow rate was calculated with the real gas law. Then, superficial gas velocity with the units m/s was found from:

$$v_{sg} = \frac{Q(p, T)}{A_R} \tag{7.3}$$

where the cross sectional area of the reactor A_R was 0.025 m^2.

7.3 Model and parameter values

The present and the previous experimental results were used to arrive at an empirical expression that included the main parameters affecting the gas consumption rate. All the present experiments in Appendix A and all the experimental results of Parlaktuna and Gudmundsson (1998a, 1998b), except from one experiment performed at 1600 RPM, were included. Based on the analysis of totally 91 experimental data, the following empirical model for the gas consumption rate emerged:

$$q = k\, p\, v_{sg}^{\alpha} (P_g + P_o)^{\beta} \tag{7.4}$$

where q is the gas consumption rate, p the pressure, v_{sg} the superficial gas velocity, P_g the gassed power consumption and P_o an additional power consumption term. The range of the experimental parameters are given in Table 7.1. The converged values and the 95 % confidence intervals of the fitting parameters are given in Table 7.2.

Table 7.1. Range of investigated parameters in methane and natural gas mixture experiments.

Parameter	Range of parameter
Pressure p [bar]	48-90
Superficial gas velocity v_{sg} [m/s]	$59.1 \cdot 10^{-6}$ - $2.37 \cdot 10^{-3}$
Gassed power consumption P_g [W]	0-29.95
Subcooling ΔT [°C]	2-8
Gas consumption rate q [m^3/s]	$0.119 \cdot 10^{-6}$ - $32.2 \cdot 10^{-6}$

Table 7.2. Fitting parameters in Equation 7.4.

Parameter	Converged value	95% confidence interval
k [$m^{3-\alpha} s^{\alpha-1} bar^{-1} W^{-\beta}$]	$0.143 \cdot 10^{-3}$	$0.0643 \cdot 10^{-3}$
α [–]	1.00	0.0707
β [–]	0.146	0.0769

The additional power consumption term P_o was 0.030. It was found by minimizing, by trial and error, the sum of squares of the difference between measured and calculated gas consumption rates. P_o was considered to represent other sources of mixing such as the turbulence created by the gas and liquid streams into the reactor. The term was included to account for the measured gas consumption rates when the stirring was turned off (Parlaktuna and Gudmundsson, 1998a).

The subcooling was not included in Equation 7.4 because the effect of subcooling on the consumption rate was found to be insignificant. However, if a subcooling term had been included, its exponent would have been 0.02 with a 95 % confidence interval of 0.10. The pressure term exponent was left out of Equation 7.4. Using an exponent on the pressure term resulted in a converged value of 0.99 with a 95 % confidence interval of 0.27. The values of α and β remained almost unchanged (as in Table 7.2), however, the confidence interval of k exceeded the converged value of k. This was attributed to the relatively scattered experimental results, especially at 90 bar. Hence, an exponent equal to unity was assumed without affecting the empirical model significantly. Including both a pressure term exponent and a subcooling term, generated a pressure term exponent equal to 0.72 and a subcooling term exponent equal to 0.12, however, the 95 % confidence interval of k exceeded the converged value of k.

The constant α was equal to 1.00. This demonstrated that the gas consumption rate was proportional to the gas injection rate, as concluded from the experimental results. The exponent on the pressure term equal to 0.99 indicated that the consumption rate was proportional to pressure as well. However, the pressure exponent was 0.72 when including both pressure and subcooling, indicating that the pressure effect may have been less important than the superficial gas velocity effect.

According to Equation 7.1, the power consumption term β, equal to 0.146, corresponded to an exponential term on the stirring rate term equal to 0.438. This demonstrated that the stirring rate was less important than the superficial gas velocity and the pressure. Also, the value of β indicated that the gas consumption rate increased faster at low stirring rates than at high stirring rates.

In Figure 7.1, the measured gas consumption rates are plotted against the calculated gas consumption rates using Equation 7.4 and the fitted parameters in Table 7.2. Most of the calculated gas consumption rates were within ±30 % of the measured gas consumption rates. Previous experimental results (Parlaktuna and Gudmundsson, 1998a, 1998b), generally shown as low gas consumption rates, and present results, shown as intermediate and high consumption rates, indicated that the empirical model in Equation 7.4 described both groups of results equally well.

7.4 Interactions between parameters

The significant effects, the superficial gas velocity, the pressure and the power consumption, were included in the empirical model (Equation 7.4). In descending order of importance, increased superficial gas velocity, pressure and power consumption resulted in increased gas consumption rate. The effect of subcooling was insignificant. In comparing the experimental results in Chapter 5, no effect of gas composition was found.

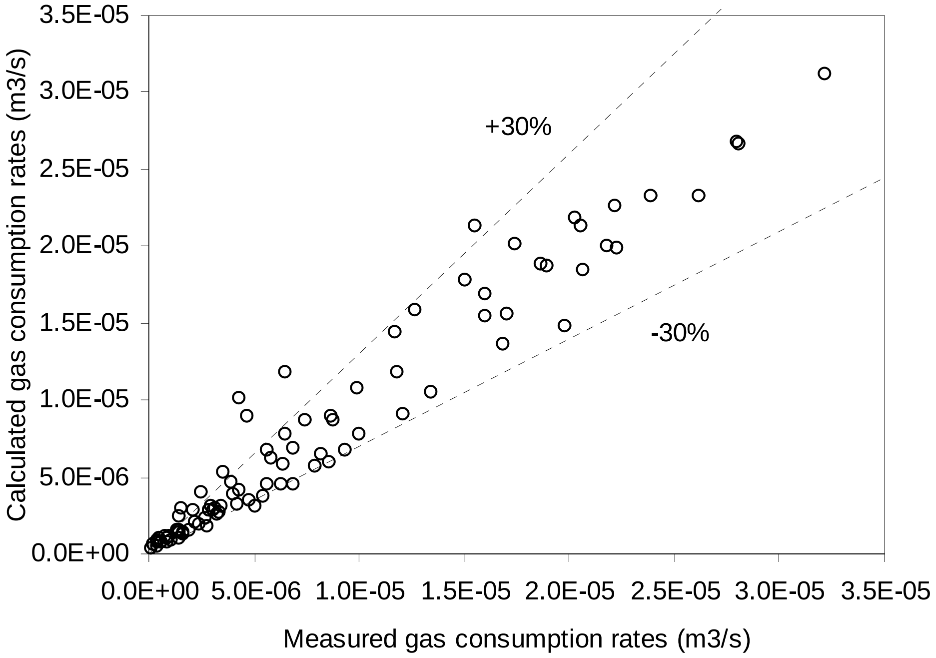

Figure 7.1 Measured and calculated (Equation 7.4) gas consumption rates for methane and natural gas mixture hydrate formation, both present and previous experimental results (Parlaktuna and Gudmundsson, 1998a, 1998b).

The effects of superficial gas velocity and power consumption were closely related. In the experiments, gas was bubbled into the reactor through two inlets, the bubbles rose to the Rushton turbine where the bubbles were broken and the gas dispersed in the water. Different flow regimes are created depending on the gas flow rate and the stirring rate (Section 3.4). The stirring rate for transition to the recirculating regime was calculated using Equation 3.9 on page 41 and the dimensions of the reactor in Figure 4.2. The result indicated that the transition to recirculated regime occurred at stirring rates between 190 and 398 RPM for the present experimental gas flow rates. Similarly, the transition to complete dispersion (Equation 3.8 on page 41) occurred from 33 to 206 RPM. According to Equation 3.8, the impeller could completely disperse the gas at 400 RPM for superficial gas velocities up to 0.035 m/s. The maximum superficial gas velocity in present experiments was $2.37 \cdot 10^{-3}$ m/s. Nearly all experiments were carried out at 400 or 800 RPM, meaning that the gas in the reactor was at least completely dispersed and probably recirculated.

Identification of the flow regime helps explaining why the hydrate formation rate was proportional to the superficial gas velocity and less dependent on the power consumption. Several researchers (Vysniauskas and Bishnoi, 1983, Skovborg and Rasmussen, 1994, Kvamme, 1996) have stressed the importance of the gas-liquid interfacial area in the hydrate formation process. Increased superficial gas velocity results in more gas bubbles, and hence, increased interfacial area. The mass transfer rate is proportional to the interfacial area (Equation 3.14). Consequently, assuming that gas-liquid mass transfer occurred, the gas consumption rate was proportional to the interfacial area, and thus, proportional to the superficial gas velocity too. Excess stirring did not increase the interfacial area significantly because the gas was completely dispersed or even recirculated at the experimental stirring rates. Therefore, the power consumption had a small effect on the gas consumption rate.

The empirical model showed a strong effect of pressure and a negligible effect of subcooling. In contrast, Parlaktuna and Gudmundsson (1998b) observed a small increase in consumption rate with increased subcooling (Figure 5.2). The increased gas consumption rate with increased pressure or subcooling could have been caused by increased driving force for hydrate formation, increased solubility of methane gas or natural gas mixture in water, or a combination of the two.

For gas-liquid mass transfer the distance from the hydrate equilibrium curve, in terms of overpressure or subcooling, is irrelevant. According to Mullin (1993), the crystal growth rate depends on the driving force, but not on hydrodynamic effects. Thus, because the hydrodynamics affected the consumption rate significantly, the effect of pressure was dominated by an effect of increased gas-liquid mass transfer rate through increased gas solubility.

The relative importance of pressure and temperature on the solubility of methane in water was investigated. According to Henry’s law, the solubility of methane, ethane and propane increases with an increase in pressure and a decrease in temperature, as presented in Appendix C. The procedure in Appendix C was used to calculate methane solubilities at 5, 7 and 9 °C for 70, 80 and 90 bar. The selected pressures and temperatures were within the range of the experimental conditions. By using POLYMATH 5.1 (2002), the following equation was found to fit the calculated methane solubilities:

$$x = 8.39 \cdot 10^{-5} p^{0.84} T^{-0.17} \qquad (7.5)$$

where x is the mole fraction solubility.

The exponents in Equation 7.5 show that pressure strongly affects the solubility while temperature weakly affects the solubility. The empirical model and the experimental results demonstrated that pressure strongly affected the gas consumption rate. The small effect of increased subcooling, that is, decreased temperature, in the previous results (Parlaktuna and Gudmundsson, 1998b) was comparable to the effect of temperature on solubility. Hence, the effects of pressure and temperature on solubility resembled the effects of pressure and temperature on the hydrate formation rate, and the effect of pressure was an effect of increased solubility. In addition, the pressure may have affected the gas-liquid interfacial area, but whether the interfacial area increased or decreased with increased pressure could not be concluded. In the literature, studies of effect of pressure are contradictory (Stegeman *et al.*, 1995, Maalej, Benadda and Otterbein, 2001).

The empirical model was developed based on the results from both methane gas and natural gas mixture experiments because no difference between the consumption rates of the two gases was observed. The consumption rates were compared at similar subcooling (Figure 5.14), but the temperature was about 7 °C higher in natural gas mixture experiments than in the methane gas experiments. This supported that the gas consumption rate was insensitive to a change in temperature. The natural gas mixture consisted of 92 % methane, but formed sII hydrates. Hence, it was likely that the gas composition would influence the rate of inclusion of gas molecules into the hydrate structure rather than the rate of gas dissolution. Therefore, because the composition did not affect the consumption rate, the gas consumption rate was not dominated by the rate of inclusion.

The hydrodynamic effects of superficial gas velocity and stirring, the effect of solubility and the lack of a compositional effect, indicated that, for the present experimental conditions, the rate of hydrate formation was controlled by the rate of gas transport rather than the rate of inclusion of gas molecules into the hydrate structure.

8

Mass transfer model

The rate of hydrate formation has been measured at conditions where nucleation easily commences and where hydrate crystals grow and agglomerate. New hydrate crystals form and grow as more gas is injected into the reactor. The hydrate formation may take place both at the gas-liquid interface and in the liquid bulk phase. The total gas-liquid interfacial area is given by the gas bubble size distribution while the hydrate crystal surface area is given by the particle size distribution. The hydrate formation process is complex.

The objective of this chapter is to present a mass transfer model, based on basic theory, applicable for analysis of the experimental results and for design of a large scale hydrate reactor. The model and its assumptions are presented in Section 8.1. The solubility of hydrocarbon gases in water and the overall mass transfer coefficient, both important parameters in the model, are discussed in Section 8.2 and Section 8.3, respectively. The model parameters are presented in Section 8.4. The model is compared with the experimental results in Section 8.5. The overall mass transfer coefficient and the rate of hydrate formation are compared with literature values in Section 8.6.

URN:NBN:no-3342

8.1 Model development

The hydrate formation process can be studied both at a macroscopic and a microscopic (molecular) level. Mullin (1993) gives an overview of different growth theories in crystallization. In the present study, hydrate formation was considered as a crystallization phenomenon where mass transfer and crystal growth are the relevant phenomena. Nucleation was considered to be instantaneous based on the experimental observations. A model, based on experimental findings and given the name bubble-to-crystal model, was proposed, and mass transfer was chosen to represent the transport processes in the system, including heat transfer.

The hydrate forming system consists of gas bubbles and growing hydrate crystals dispersed in a continuous water phase, as illustrated in Figure 8.1. Gas is transferred in consecutive steps between the three phases. Concentration gradients are chosen to represent the driving force in each step. Also, temperature gradients are included to illustrate the temperature increase from gas bubble to hydrate crystal.

According to standard two-film theory (Froment and Bischoff, 1990), film layers exist in both gas and liquid phases along the interface. Gas is transferred by molecular diffusion through the gas side film to the gas-liquid interface and further through the liquid film to the liquid bulk. The gas side resistance to mass transfer is assumed negligible, which usually holds for sparingly soluble gases such as methane, ethane and propane (Whitton, 1992). Similar is assumed for the gas side heat transfer resistance. The gas and liquid phases are in equilibrium at the gas-liquid interface. The temperature increases across the liquid film due to heat of solution. In the liquid bulk, the turbulence is sufficient to eliminate concentration and temperature gradients. Here the gas is transferred due to both eddy and molecular diffusion.

Mullin (1993) has reviewed diffusion-reaction theories for crystal growth. These theories are considered suitable for engineering approaches, however, it is not proved that they represent the nature of crystallization more correctly than other growth models. A two step model is adopted for the transport of gas from the bulk to the crystal surface and the inclusion of the gas molecules into the hydrate

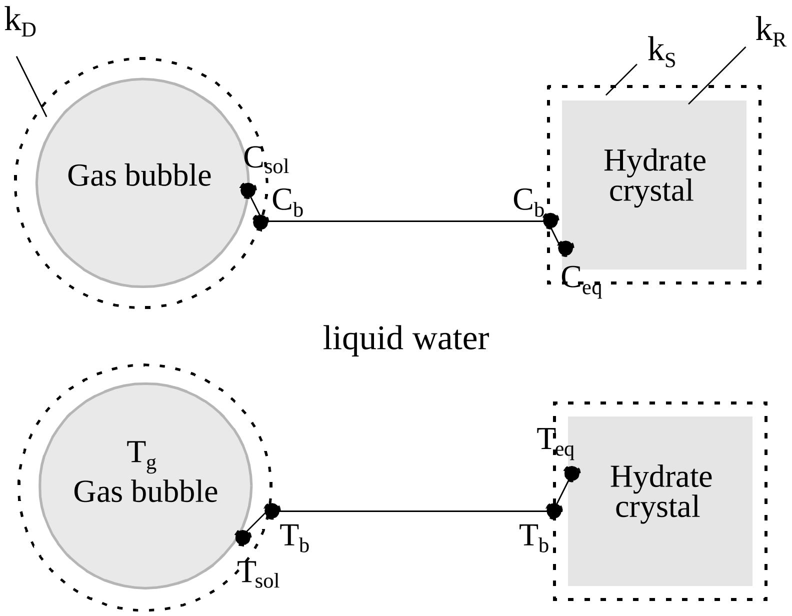

Figure 8.1 Schematic illustration of the bubble-to-crystal model showing the concentration and temperature gradients as gas is transferred from the gas bubble to the hydrate crystal.

structure. Gas is transferred by molecular diffusion through a liquid film surrounding the hydrate crystal. The temperature increases across the film due to heat of hydrate formation. At the crystal surface, the dissolved gas is in equilibrium with the hydrate crystal. The gas molecules are included into the hydrate structure at the crystal surface. The inclusion of gas is modeled as a transport process where the gas is transferred across a hypothetical stagnant film at the crystal surface.

Assuming no accumulation in the liquid film around the gas bubble and neglecting the gas side mass transfer resistance, the following equation emerges for the rate of gas dissolution in liquid bulk:

$$r_1 = k_L a (C_{sol} - C_b) \tag{8.1}$$

where k_L is the gas-liquid mass transfer coefficient and a represents the gas-liquid interfacial area per liquid volume. Also, it is assumed that a negligible amount of gas is converted to hydrate during transfer through the liquid film. Assuming equilibrium between the gas and the liquid phase, the gas concentration at the interface is given by the mole fraction solubility of gas in water at the experimental pressure and temperature:

$$C_{sol} = \frac{x(p, T)\,\rho_{H_2O}}{M_{H_2O}} \tag{8.2}$$

In the bulk, the gas concentration is assumed uniform due to turbulent mixing of the liquid phase. The diffusion of gas through the liquid film around the hydrate crystal is expressed as:

$$r_2 = k_S a_c (C_b - C_i) \tag{8.3}$$

by assuming no accumulation in the film. k_S is the liquid-solid mass transfer coefficient, a_c is the hydrate crystal surface area and C_i is the concentration of gas at the liquid-crystal interface. The surface area of the liquid film is assumed equal to the hydrate crystal surface area. According to Mullin (1993), when the surface integration is of first-order, the rate of inclusion of molecules into the crystal structure is expressed in terms of a concentration drop across a hypothetical stagnant film:

$$r_3 = k_R a_c (C_i - C_{eq}) \tag{8.4}$$

where k_R is the rate constant and C_{eq} is the gas concentration at the crystal surface where gas and water are in equilibrium with hydrate. The temperature is equal to the hydrate equilibrium temperature while the pressure is uniform throughout the system and is therefore equal to the experimental pressure. Thus, assuming equilibrium between gas, water and hydrate phases at the crystal surface, the concentration at the hydrate crystal surface is the solubility of gas in water at the experimental pressure and the hydrate equilibrium temperature:

$$C_{eq} = \frac{x(p, T_{eq})\,\rho_{H_2O}}{M_{H_2O}} \tag{8.5}$$

Equating the three consecutive steps in the hydrate formation process gives the overall rate of hydrate formation per liquid volume:

$$r_{hyd} = K(C_{sol} - C_{eq}) \tag{8.6}$$

where K is the overall mass transfer coefficient given by:

$$\frac{1}{K} = \frac{1}{k_L a} + \frac{1}{k_S a_c} + \frac{1}{k_R a_c} \tag{8.7}$$

Thus, the driving force for hydrate formation is the difference in gas solubility concentration at the experimental conditions and the gas solubility concentration at the hydrate equilibrium conditions. The pressure and the temperature conditions at the gas-liquid interface and at the crystal surface, and thereby also the temperature driving force (subcooling), are included in the driving force.

Based on the argument that the hydrate formation rate was limited by transport of gas (Section 7.4), the rate constant k_R for the integration process is considered large compared to the two other mass transfer coefficients, eliminating the crystal surface integration term. The overall mass transfer coefficient in Equation 8.7 can therefore be simplified to:

$$\frac{1}{K} = \frac{1}{k_L a} + \frac{1}{k_S a_c} \tag{8.8}$$

The sizes of the gas bubble and the hydrate crystal have not been considered in the bubble-to-crystal model. The same assumptions and model apply if the gas bubble is large compared to the hydrate crystal, many hydrate crystals can surround the gas bubble, for example. Moreover, a large crystal can be surrounded by many small gas bubbles. Microcrystals and microbubbles can exist on a bubble and on a crystal, respectively.

Irrespective of the relative size or the distance between a crystal and a gas bubble, the model depends on the assumption that there is a liquid film between the crystal and the bubble where the gas must dissolve to form hydrate. Hirata and Mori (1998) argued that it is likely that the hydrate surface is hydrophilic, that is, wettable with liquid water because the major proportion of gas hydrate is water. In experiments, Hirata and Mori observed that THF hydrates are highly hydrophilic and concluded that presumably hydrates in general have highly hydrophilic surfaces.

The bubble-to-crystal model is developed for a single gas component system. Using an approach of Himmelblau (1960) for the solubility of gas mixtures presented in Appendix C, the model applies to gas mixtures as well. It is important to note, however, that this approach assumes that the mass transfer coefficients are equal and hence, that the rates of diffusion of the different components are equal or similar.

8.2 Solubility of gas in water

To calculate the gas concentrations at the gas-liquid interface and at the crystal surface (Equation 8.2 and Equation 8.5, respectively), gas solubility data at the experimental and equilibrium conditions were required. In the literature, experimental data on methane, ethane and propane solubilities in water at high pressure and low temperature are limited. Before deciding what data to use for calculation of solubility concentrations, an overview of relevant literature is given below.

Besnard *et al.* (1997) and Song *et al.* (1997) reported methane solubility at near hydrate forming conditions, from 0 to 19 °C and 34.5 to 139.3 bar (Figure 8.2). A significant increase in methane solubility near hydrate forming conditions was observed and ascribed to structuring of the water molecules around the gas molecules. Also shown are the data of Cramer (1984) at 30 bar and Perry and Green (1984), calculated from Henry's law constants using a procedure described in Appendix C. The results of Besnard *et al.* and Song *et al.* deviate significantly from Henry's law calculations while the results of Cramer correspond well with Henry's law.

Lekvam and Bishnoi (1997) measured the solubility of methane near hydrate forming conditions at 1.2, 10.2 and 12.5 °C at pressures ranging from 5.7 to 90.8 bar (Figure 8.3). Solubilities based on the data of Perry and Green (1984) were predicted for 1.2 and 12.5 °C and also shown in Figure 8.3. The calculated solubilities correspond well at 1.2 °C and overestimate the solubility at 12.5 °C and high pressure. Englezos and Bishnoi (1988) reported the mole fractions of methane in water at the nucleation point. The results, plotted in Figure 8.3, show that the mole fractions at the nucleation point are similar to the solubility results of Lekvam and Bishnoi and calculated solubilities, however, the data of Englezos and Bishnoi are more scattered.

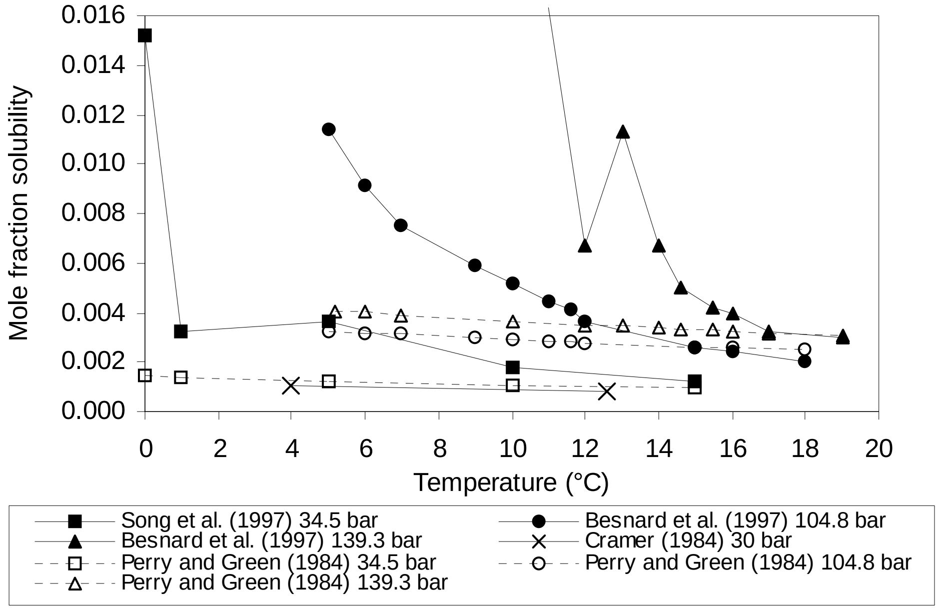

Figure 8.2 Solubility data for methane in water. Besnard et al. (1997) measured that the solubility was 0.05244 at 139.3 bar and 5.2 °C.

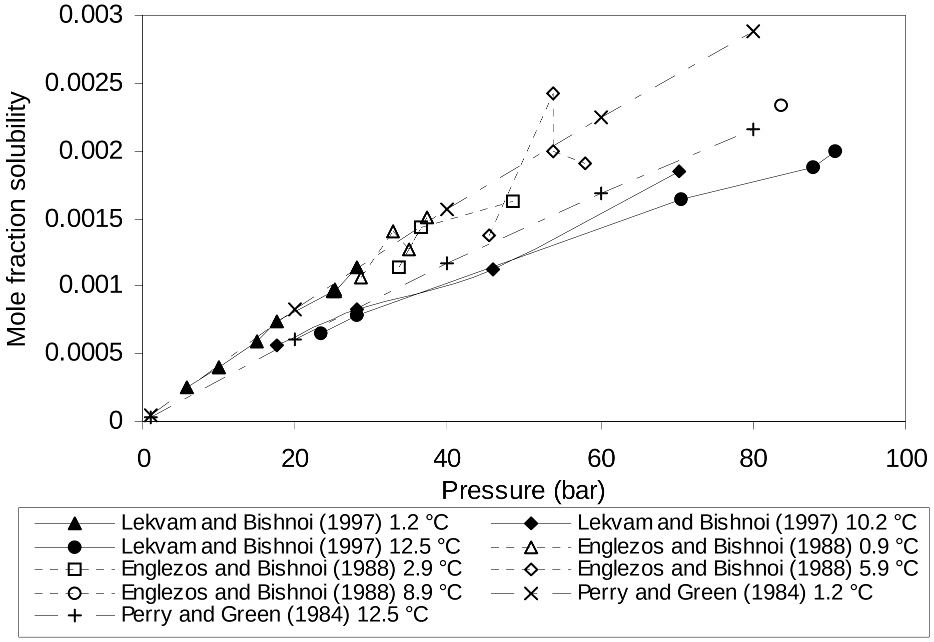

Figure 8.3 Solubility data for methane in water.

Wang *et al.* (1995) measured the solubility of methane as a function of pressure at 10, 15 and 20 °C. The results are shown in Figure 8.4 together with calculated solubilities based on Henry’s law constants reported by Perry and Green (1984) and the procedure in Appendix C. Handa (1990) predicted the solubility at 0 and 5 °C up to 500 bar. Some of the calculated values are shown in Figure 8.4. The experimental results of Wang *et al.* and the calculated results of Handa correspond well with Henry’s law solubilities, especially up to a pressure of about 50 bar.

Song *et al.* (1997) measured ethane solubilities at low temperatures at 6.6 bar. A significant increase in solubility near hydrate forming conditions was observed. Figure 8.5 shows the results and calculated solubilities using Henry’s law constants for ethane (Perry and Green, 1984) and the procedure described in Appendix C. The results of Song *et al.* deviate significantly from the Henry’s law calculations. Ethane solubilities of Culberson and McKetta (1950) at 37.8 °C are compared with Henry’s law solubility (Perry and Green, 1984) in Figure 8.6. Henry’s law overestimates the solubility at high pressures, however the deviations are relatively small at pressures up to about 100 bar.

Azarnoosh and McKetta (1958) reported the solubility of propane up to 11 bar for 15.6 and 37.8 °C (Figure 8.7). Kobayashi and Katz (1953) reported the solubility of propane at 12.2 and 37.8 °C and Henry’s law constants for 37.8, 54.4, 71.7 °C. Experimental data are shown in Figure 8.7 together with solubilities calculated from the reported Henry’s law constants using the procedure in Appendix C. The calculated solubilities are in good agreement with the experimental results of Azarnoosh and McKetta, and Kobayashi and Katz at low pressure, however, Henry’s law overestimates the solubility at high pressure.

Based on the above comparisons of experimental data and predictions using Henry’s law, it is concluded that Henry’s law predicts the solubility of methane, ethane and propane in water with good accuracy at low pressure. The solubility is overestimated at higher pressure, typically around experimental conditions for hydrate experiments (Section 5.2). The significant increase in solubility at low temperature, only observed by Song *et al.* (1997) and Besnard *et al.* (1997), is not accounted for in Henry’s law. Due to lack of consistent data at low temperatures and pressures around 70 to 90 bar, Henry’s law was chosen for calculation of the mole fraction solubilities in the bubble-to-crystal model (Equation 8.2 and

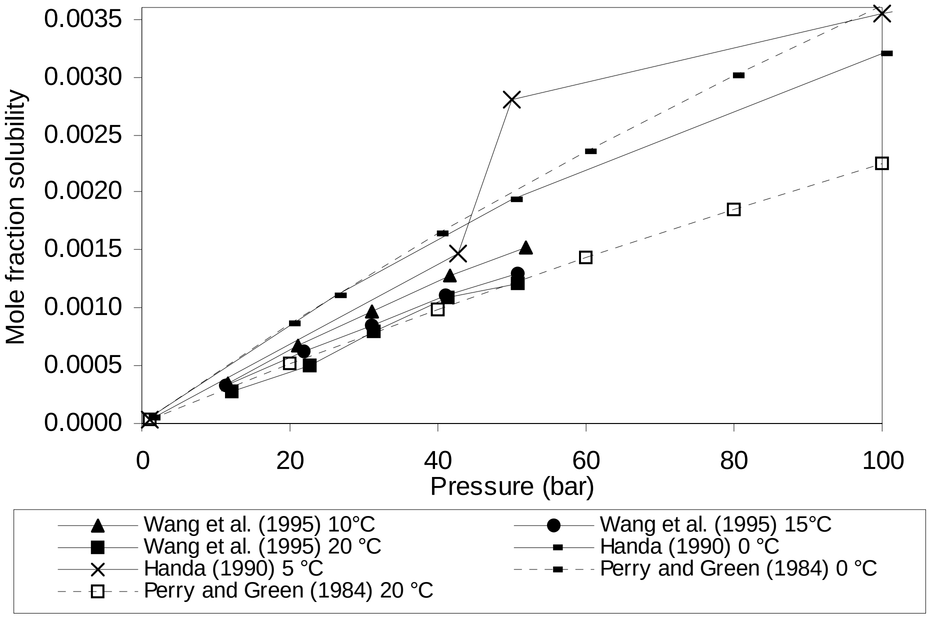

Figure 8.4 Solubility data for methane in water.

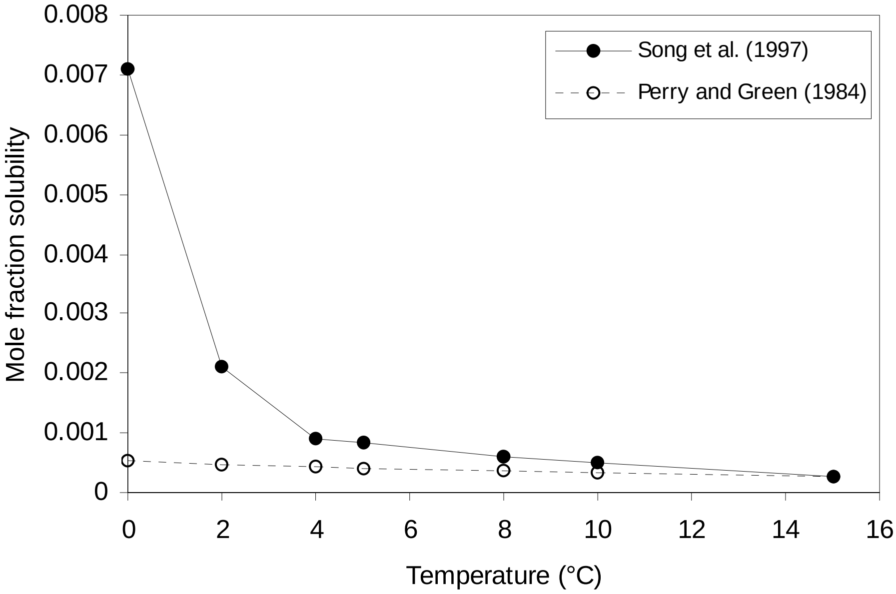

Figure 8.5 Solubility data for ethane in water at 6.6 bar.

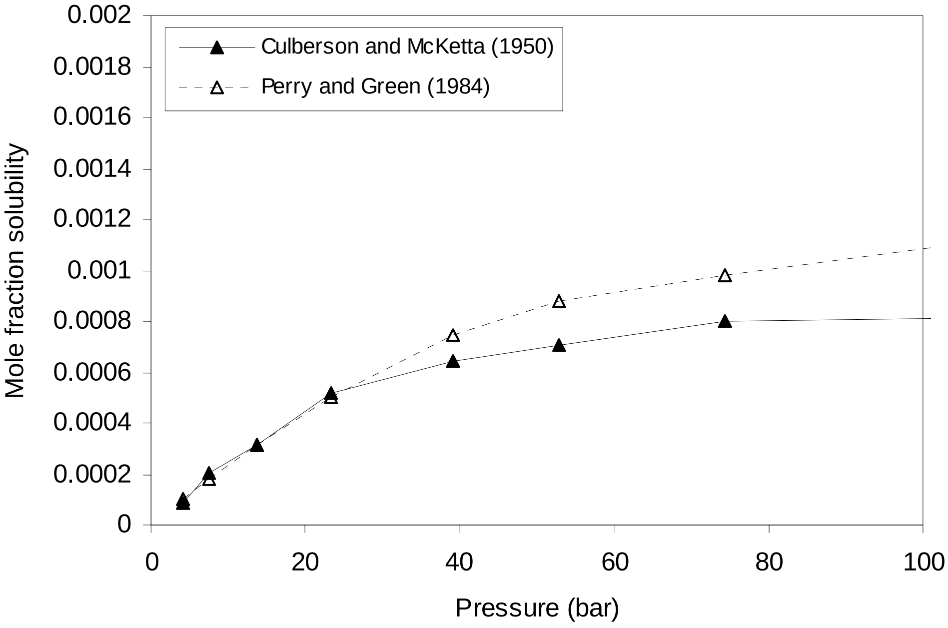

Figure 8.6 Solubility data for ethane in water at 37.8 °C.

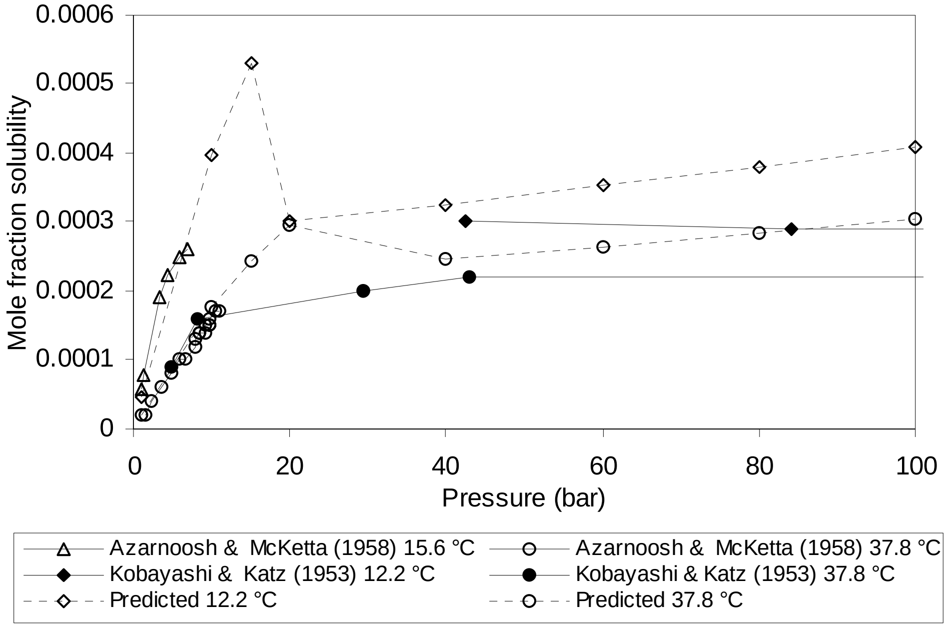

Figure 8.7 Solubility data for propane in water. Predicted solubilities are based on Henry's law constants obtained from the data of Kobayashi and Katz (1953).

Equation 8.5). At high pressure, the overestimation became less significant since the calculated mole fraction solubilities were subtracted in calculation of the concentration driving force. The calculation procedure in Appendix C was used.

8.3 Overall mass transfer coefficient

The overall mass transfer coefficient *K* in Equation 8.8 was determined by using an approach adopted from determination of gas-liquid mass transfer coefficients in stirred reactors of standard design (Section 3.5). The volumetric gas-liquid mass transfer coefficient can be expressed by the relationship (Equation 3.15):

$$k_L a = \alpha\left(\frac{P_g}{V}\right)^{\beta}(v_{sg})^{\gamma} \tag{8.9}$$

Experiments performed by Grisafi, Brucato and Rizzuti (1998) in a gas-liquid-solid reactor of standard design show that the liquid-solid mass transfer coefficient is affected by the impeller power consumption, but not by the gas injection rate if the gas injection rate is taken into account in the calculation of the power consumption. Assuming that the liquid-solid mass transfer coefficient was a function of gassed power consumption only, based on Equation 8.9, the following expression was suggested to represent the solid-liquid mass transfer coefficient:

$$k_S a_c = \delta\left(\frac{P_g}{V}\right)^{\lambda} \tag{8.10}$$

Thus, the overall mass transfer coefficient in Equation 8.8 was expressed as:

$$\frac{1}{K} = \frac{1}{\alpha\left(\frac{P_g}{V}\right)^{\beta}(v_{sg})^{\gamma}} + \frac{1}{\delta\left(\frac{P_g}{V}\right)^{\lambda}} \tag{8.11}$$

where the constants were model parameters that had to be determined by fitting the model to the experimental results. The superficial gas velocity was indirectly included in the second term of Equation 8.11 through the gassed power consumption, calculated as in the empirical model (Equation 7.1 and Equation 7.2).

8.4 Estimation of model parameters

Based on Equation 8.6, the overall rate of hydrate formation for the total liquid volume was modelled using:

$$R_{tot} = K(C_{sol} - C_{eq})V \tag{8.12}$$

where the mass transfer coefficient K is given in Equation 8.11. The overall hydrate formation rate is given in terms of moles of gas per second, hence, the liquid volume where hydrate formation occurs is included. The reactor volume was chosen as the liquid volume.

The model parameters in Equation 8.11 were determined by fitting the model to the experimental results. Separate model parameters for methane and natural gas mixture hydrate formation were determined based on 59 and 32 experimental data points, respectively. The regression was performed using the computer program POLYMATH 5.1 (2002) featuring multiple non-linear regression. Input parameters to the program were gas consumption rate in terms of mole per second, superficial gas velocity, gassed power consumption and concentration driving force. Except from the input parameters, the method was equal to the method described in Section 7.1.

For methane gas results, an attempt was made to fit the experimental data to the model with the overall mass transfer coefficient given in Equation 8.11. This attempt was unsuccessful, and simplifications of Equation 8.11 were investigated. First, β and λ were assumed equal. The 95 % confidence intervals of the parameters α and δ in Equation 8.11 were larger than their mean values, which was not accepted. Equation 8.11 was simplified further by assuming that β was equal to λ, and that α was equal to δ (Table 8.1). For all the fitting parameters, the 95 % confidence intervals were smaller than the converged values and the model could be accepted.

The resulting liquid-solid volumetric mass transfer coefficient was about three orders of magnitude larger than the gas-liquid volumetric mass transfer coefficient because the superficial gas velocity was not included in the liquid-solid volumetric mass transfer coefficient. In the experiments, the increasing hydrate crystal concentration did not influence the gas consumption rate (Section 5.4), which indicated that the hydrate crystal surface area did not influence the consumption rate (Equation 8.3) and that the formation rate was controlled by the gas-liquid mass transfer rather than the liquid-solid mass transfer. Also, the importance of the superficial gas velocity and the small effect of stirring rate supported this observation. Skovborg and Rasmussen (1994) also arrived at the conclusion that the gas-liquid mass transfer controlled the rate of hydrate formation. Thus, the liquid-solid volumetric mass transfer coefficient was much larger than the gas-liquid volumetric mass transfer coefficient, and the gas-liquid mass transfer coefficient could be used to represent the overall mass transfer coefficient.

Removing the second term on the right hand side of Equation 8.11, the liquid-solid volumetric mass transfer coefficient term, insignificant difference in converged parameters were observed (Table 8.2). The 95 % confidence intervals were smaller than the mean value for all parameters, and the sum of squares was slightly lower than in Table 8.1. The final bubble-to-crystal model equation (Equation 8.12), including the mass transfer coefficient in Equation 8.9 and the model parameters in Table 8.2, became:

$$R_{tot} = 363.3\left(\frac{P_g}{V}\right)^{0.1801}(v_{sg})^{1.124}(C_{sol} - C_{eq}) \cdot 9.5 \qquad (8.13)$$

Based on the same observations in natural gas mixture experiments, the model parameters in Table 8.3 were found using Equation 8.9 and Equation 8.12. For the constant α, the 95 % confidence interval exceeded the mean value. The superficial gas velocity exponent γ was considerably higher than the superficial gas velocity exponent for methane gas (Table 8.2) and did not correspond with the observation that the gas consumption rate was proportional to the gas injection rate (Figure 5.12). Similarly, the gassed power consumption exponent β was higher than expected from the experimental results (Parlaktuna and Gudmundsson, 1998a) and comparison with methane gas results. Less experimental data on natural gas mixture and operational challenges (discussed in Section 4.5) could explain these deviations.

URN:NBN:no-3342

Table 8.1. Model parameters for methane hydrate formation, including gas-liquid and liquid-solid volumetric mass transfer coefficient.

$\alpha = \delta$ $\beta = \lambda$	$K = \dfrac{\alpha\left(\frac{P_g}{V}\right)^{\beta}(v_{sg})^{\gamma}}{1 + (v_{sg})^{\gamma}}$	
Parameter	Converged value	95% confidence interval
α	365.2	339.6
β	0.1801	0.1378
γ	1.125	0.1162
Sum of squares of errors 70.29		

Table 8.2. Model parameters for methane hydrate formation.

$K = \alpha\left(\frac{P_g}{V}\right)^{\beta}(v_{sg})^{\gamma}$		
Parameter	Converged value	95% confidence interval
α	363.3	338.3
β	0.1801	0.1378
γ	1.124	0.1165
Sum of squares of errors 70.27		

Table 8.3. Model parameters for natural gas mixture hydrate formation.

$K = \alpha\left(\frac{P_g}{V}\right)^{\beta}(v_{sg})^{\gamma}$		
Parameter	Converged value	95% confidence interval
α	100.4	360.2
β	0.8805	0.7320
γ	1.473	0.2159
Sum of squares of errors 12.51		

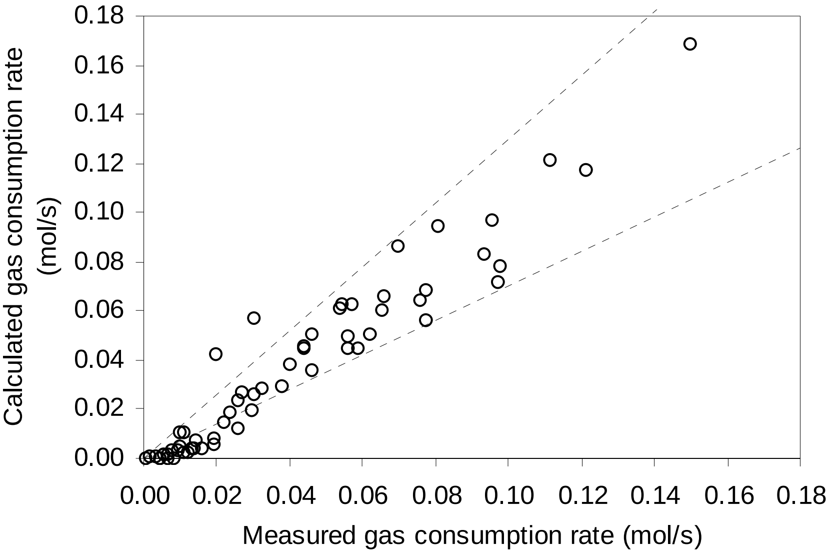

Figure 8.8 Methane gas results. Measured gas consumption rates vs. calculated gas consumption rates using the values given in Table 8.2. Dotted lines indicate ±30 % deviation between calculated and measured consumption rates.

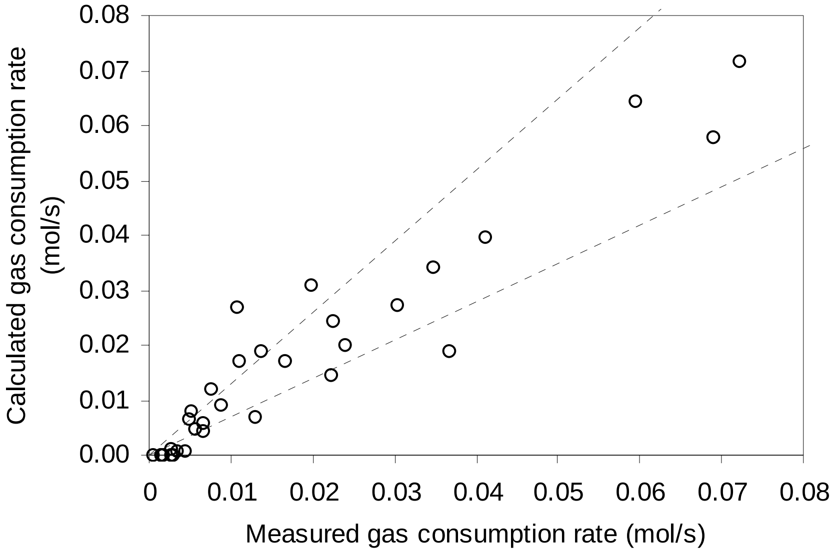

Figure 8.9 Natural gas mixture results. Measured gas consumption rates vs. calculated gas consumption rates using the values given in Table 8.3. Dotted lines indicate ±30 % deviation between calculated and measured consumption rates.

8.5 Comparison with experimental results

Gas consumption rates calculated with the bubble-to-crystal model are plotted against measured gas consumption rates for methane gas and natural gas mixture in Figure 8.8 and Figure 8.9, respectively. Most calculated gas consumption rates were within ±30 % of the measured gas consumption rates, however, the bubble-to-crystal model underestimated the consumption rate at low rates.

The underestimated consumption rates stem from an experimental series investigating the effect of stirring rate on the gas consumption rate (Parlaktuna and Gudmundsson, 1998a). Since no additional power consumption term was included, as in the empirical model in Equation 7.4, the bubble-to-crystal model predicted a gas consumption rate equal to zero for 0 RPM. However, this did not explain the underestimation for stirring rates from 200 to 800 RPM. A study of the same previous experiments in the empirical model results, indicated that also the empirical model underestimated the consumption rate in that series. One explanation was that the experimental series of Parlaktuna and Gudmundsson was carried out differently from the rest of the experiments, but no indication of that was found.

The bubble-to-crystal model was used to calculate the hydrate formation rate at selected experimental conditions (Figure 8.10, Figure 8.11). The model predicted the methane gas consumption rate satisfactorily at 70 bar, but at 90 bar, there was a discrepancy between the model and the results due to the relatively scattered experimental data. Predicted gas consumption rates for natural gas mixture (Figure 8.11) agreed with the measured rates at 70 bar. At gas injection rates higher than the experimental rates, the consumption rate increased slower because the high superficial gas velocity lead to a relatively low gassed power consumption (Equation 7.2 and Equation 7.3).

The model's ability to predict the effect of stirring rate is illustrated in Figure 8.12 and Figure 8.13. For gas injection rates around 30 Nl/min (Figure 8.12), the bubble-to-crystal model underestimated the consumption rate while the empirical model was in good agreement with the experimental data. With respect to stirring

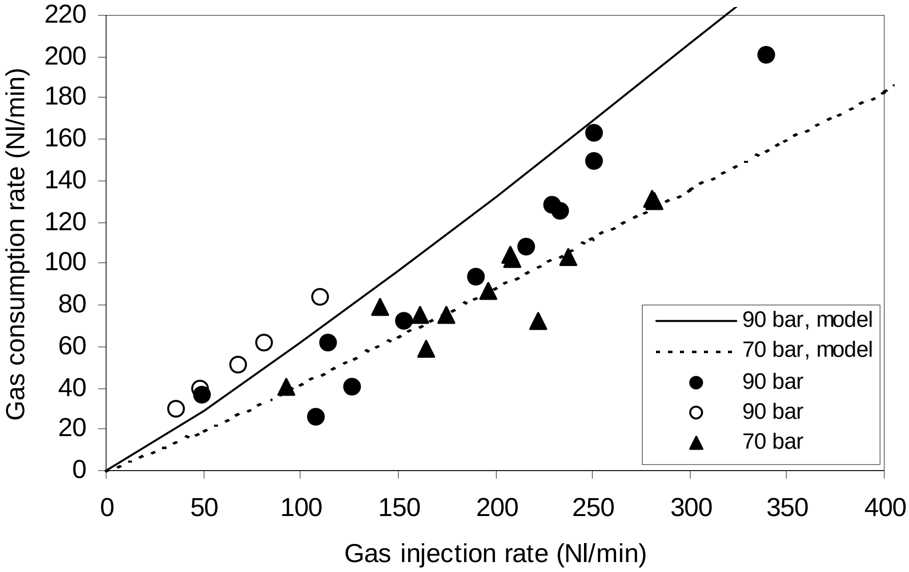

Figure 8.10 Comparison of bubble-to-crystal model (values from Table 8.2) and experimental data for methane gas at 7 °C and 400 RPM and for 70 and 90 bar. Circles are previous results at 90 bar (Parlaktuna and Gudmundsson, 1998a, 1998b).

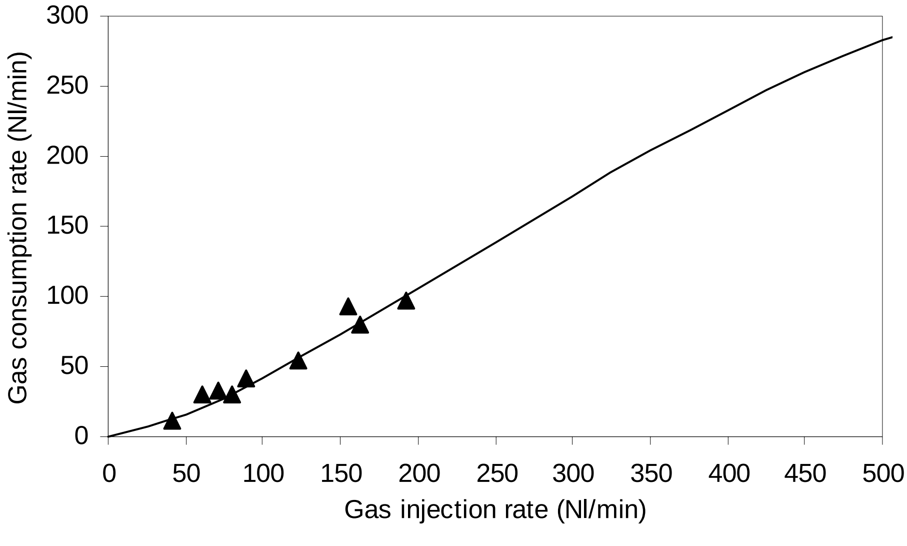

Figure 8.11 Comparison of bubble-to-crystal model (values from Table 8.3) and experimental data for natural gas mixture at 70 bar and from 14.3 to 14.6 °C.

URN:NBN:no-3342

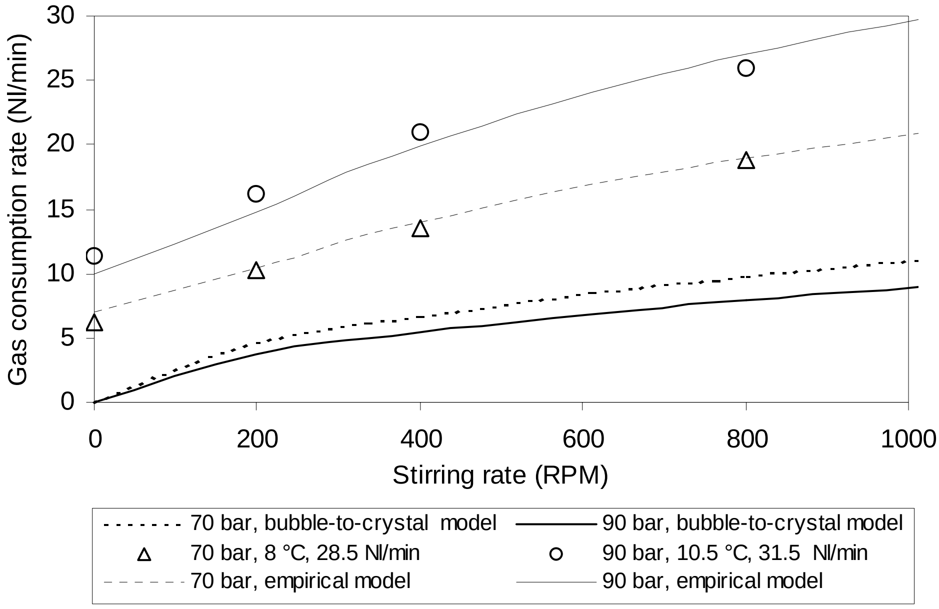

Figure 8.12 Comparison of experimental results (Parlaktuna and Gudmundsson, 1998a, 1998b) and empirical model (Equation 7.4 and Table 7.2) with bubble-to-crystal model using values from Table 8.2.

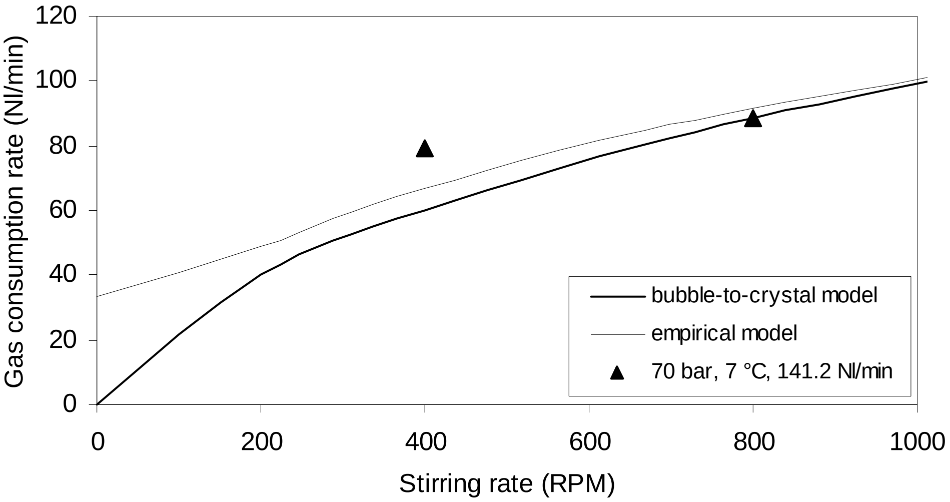

Figure 8.13 Comparison of the results from experiment 18a with bubble-to-crystal model (Table 8.2) and empirical model (Equation 7.4 and Table 7.2).

rate, the main difference between the two models was that a constant P_0 was added to the power consumption term in the empirical model, meaning that a consumption rate different from zero was calculated when the stirring rate was 0 RPM. Figure 8.13 shows that the bubble-to-crystal model predicted the gas consumption rate satisfactorily compared to the experimental data, but that the bubble-to-crystal model differed significantly from the empirical model at the lowest stirring rates.

In Figure 8.12, the gas consumption rates calculated with the bubble-to-crystal model were lower at 90 bar than at 70 bar at apparently similar conditions. However, the *in situ* superficial gas velocity and the power consumption terms were lower at 90 bar conditions than for the 70 bar case. Also, in the bubble-to-crystal model, the pressure was only accounted for indirectly in the concentration difference, making the model less sensitive to a change in pressure than the empirical model.

8.6 Comparison with literature correlations

The overall mass transfer coefficient, given in Table 8.2, was compared with correlations for the volumetric mass transfer coefficient in the literature. The volumetric mass transfer coefficients were calculated from the converged values in Table 8.2 and all the pairs of superficial gas velocity and gassed power consumption in the methane gas experiments. Three correlations from the literature for different systems were selected for comparison.

Nocentini *et al.* (1993) measured the volumetric mass transfer coefficient in a tall reactor with four Rushton turbines and a ring sparger. For air-water, the following correlation fitted the experimental data:

$$k_L a = 1.5 \cdot 10^{-2} \left(\frac{P_g}{V}\right)^{0.59} v_{sg}^{0.55} \tag{8.14}$$

Smith (1992) reported the volumetric mass transfer coefficient in an air-water system for a Rushton turbine:

$$k_L a = 1.25 \cdot 10^{-4}\left(\frac{D}{T_R}\right)^{2.8} Fr^{0.6} N_{Re}^{0.7} N_{QG}^{0.45}\left(\frac{D}{g}\right)^{-0.5} \tag{8.15}$$

Oguz, Brehm and Deckwer (1987) measured the volumetric mass transfer coefficient in homogeneous slurries in a standard reactor with a flat blade impeller with four blades and a ring sparger:

$$k_L a = 6.6 \cdot 10^{-4}\left(\frac{\mu_{Sl}}{\mu_L}\right)^{-0.39}\left(\frac{P_g}{V}\right)^{0.75} Q_G^{0.5} \tag{8.16}$$

where μ_{Sl}/μ_L is the relative viscosity between the slurry and the carrying liquid without solids.

The above correlations were plotted versus the overall mass transfer coefficient from the bubble-to-crystal model (Figure 8.14) using the experimental conditions in the present and previous methane experiments (Table 5.1 and Parlaktuna and Gudmundsson, 1998a, 1998b). In the literature correlations, the experimental pairs of superficial gas velocity and gassed power consumption were used. In addition, D = 0.076 m, ρ = 987.4 kg/m^3 (Andersson, 1999) (density in Froude number), $\mu_{Sl} = 2.57 \cdot 10^{-3}$ Pa s (Andersson, 1999) and $\mu_L = 1.79 \cdot 10^{-3}$ Pa s (Lide, 1990) were used.

The overall mass transfer coefficients in the bubble-to-crystal model were about one order of magnitude higher than the volumetric mass transfer coefficients based on literature correlations (Figure 8.14). In addition, the effects of superficial gas velocity and gassed power consumption were not well estimated using the literature correlations. The exponents on the superficial gas velocity and the gassed power consumption terms in Equation 8.14 and Equation 8.16 (here the gas flow rate) differed considerably from the exponents in Table 8.2.

For further comparison, the theoretical maximum gas-liquid mass transfer rates were calculated and compared with the measured hydrate formation rates. Defining the maximum rate as the situation where the gas concentration in the bulk is equal to zero, the maximum gas-liquid mass transfer rate was calculated from:

$$R_{G-L} = k_L a \cdot C_{sol} \cdot V \tag{8.17}$$

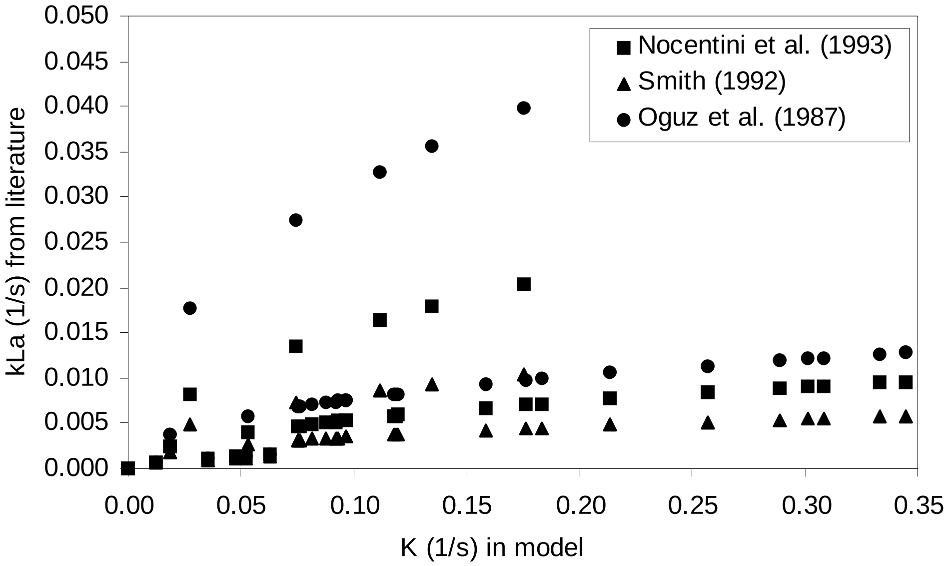

Figure 8.14 Overall mass transfer coefficient in bubble-to-crystal model versus gas-liquid volumetric mass transfer coefficients from literature. Literature coefficients were calculated at experimental conditions.

where the volumetric mass transfer coefficients from the literature were used, and C_{sol} was calculated from Equation 8.2. The theoretical maximum mass transfer rates versus the measured hydrate formation rates are shown in Figure 8.15. The measured hydrate formation rates were up to one order of magnitude higher than the theoretical maximum gas-liquid mass transfer rates. This shows that the hydrate formation process was different from a typical gas dissolution process.

A possible hypothesis for the discrepancy between the hydrate formation rates and the gas dissolution rates was that the literature volumetric mass transfer coefficients were not representative for the present system. In the literature, no correlation for the methane-water mass transfer coefficient in stirred tank reactors was available. In the present experiments, as calculated in Section 7.4, the gas in the reactor was probably recirculated. The correlations for air-water mass transfer coefficients were based on experiments where the superficial gas velocities were higher than in the present experiments. The reactors were probably operated in another flow regime.

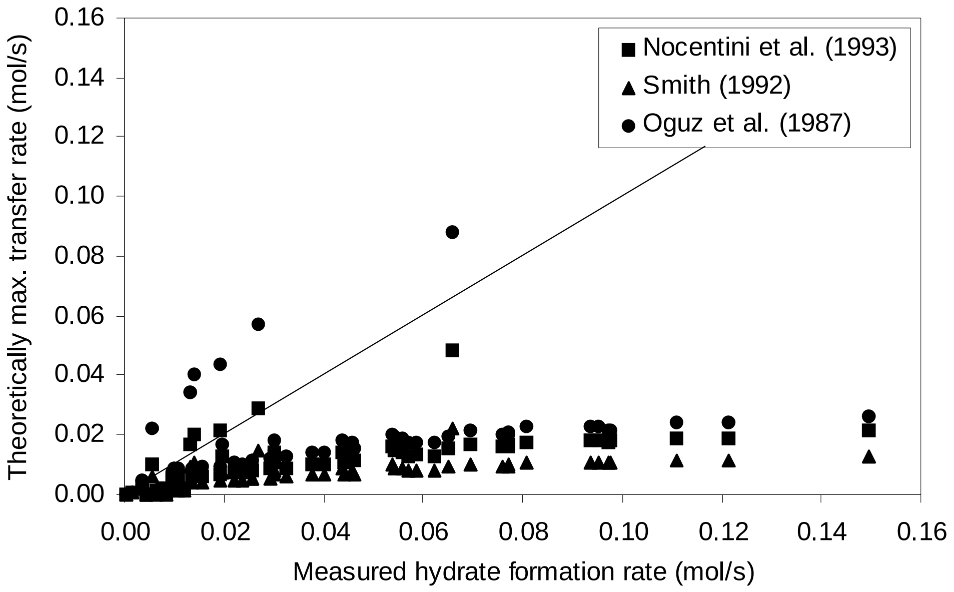

Figure 8.15 Measured hydrate formation rates (present and previous results) versus theoretically maximum gas-liquid mass transfer rate defined by Equation 8.17.

The presence of hydrate crystals may have affected the overall mass transfer coefficient differently from the particles present in the work of Oguz *et al.* (1987). The particles used by Oguz *et al.* were denser than water, while the hydrate crystals were floating. The effect of floating particles on the volumetric mass transfer coefficient is not reported in the literature.

The air-water systems reported in the literature were free coalescing systems, while the hydrate crystals may have affected the coalescing behaviour of the gas bubbles. Gumerov and Chahine (1998) studied the dynamics of gas bubbles in the presence of hydrates, and observed a complex bubble behaviour with several regimes depending on gas flow, liquid flow and capillary effects. Whitton (1992) reported that the exponents on the superficial gas velocity and the power consumption terms vary considerably from system to system, and that they change with the gas bubble behaviour of the system.

The bubble-to-crystal model and the theoretical maximum mass transfer rate were sensitive to errors in the gas solubility. The reported gas solubilities at low temperatures and high pressures deviate (Section 8.2). Especially, assuming that the data of Besnard *et al.* (1997) and Song *et al.* (1997) are correct for typical experimental conditions such as 70 bar and 7 °C, the solubility would be an order of magnitude higher than the solubility predicted by Henry's law. Thus, the maximum mass transfer rate would have increased with an order of magnitude and agreed with the measured hydrate formation rates.

8.7 Concluding remarks

The objective of this chapter was to present a mass transfer model for the rate of hydrate formation in a CSTR. The following can be concluded:

- A steady-state model, called the bubble-to-crystal model, was developed for the hydrate formation rate in a continuous stirred tank reactor. The model was based on standard film theory and mass transfer of gas from a gas bubble to a hydrate crystal surface. Mass transfer was chosen to represent all the transport phenomena in the system.
- In the model, the rate of hydrate formation was a function of an overall mass transfer coefficient and a concentration driving force.
- The experimental results showed that the rate of hydrate formation was limited by gas-liquid mass transfer. The overall mass transfer coefficient was expressed in terms of superficial gas velocity and power consumption, parameters typically used to correlate gas-liquid mass transfer coefficients.
- The difference in gas concentration at the gas-liquid interface and at the crystal surface was the driving force for hydrate formation. The concentrations were calculated by assuming that the concentration at the gas-liquid interface was the solubility concentration at the experimental pressure and temperature, and that the concentration at the crystal surface was the solubility concentration at the experimental pressure and the hydrate equilibrium temperature.
- The bubble-to-crystal model predicted the gas consumption rate within ±30 % for the majority of the experimental data, however, it underestimated the consumption rate for the lowest experimental gas consumption rates.

- The overall mass transfer coefficient was an order of magnitude higher than gas-liquid mass transfer coefficients reported in the literature. The measured gas consumption rates were higher than the maximum gas dissolution rates. The suitability of the literature correlations was questioned, and the gas solubility was pointed out as a critical parameter in the comparison.

9

Discussion

The experimental results and the models illustrate some of the characteristics of the hydrate production process, which influence the performance, operation and scale-up of the reactor. The performance of the reactor and the dominating effects are discussed in Section 9.1. The desirable operational conditions with respect to the hydrate formation rate are discussed in Section 9.2. The energy balance presented in Appendix D is used in Section 9.3 to discuss the operational conditions with respect to heat transfer. Finally, the implications of the present results on hydrate reactor scale-up is discussed in Section 9.4.

9.1 Dominating effects

The experimental results and the empirical model show that the superficial gas velocity and the pressure have a significant effect on the rate of hydrate formation. By studying the interaction between the investigated parameters (Section 7.4), it was found that the rate of hydrate formation is limited by the mass transfer of gas rather than inclusion of gas into the hydrate structure. Whether gas-liquid or liquid-solid mass transfer is the controlling step is not evident from the investigation. However, other observations support that the gas-liquid mass transfer rate is the rate-limiting step.

URN:NBN:no-3342

The hydrate formation rate did not change during a particular experimental run (Section 5.4). Hence, the hydrate concentration and the total crystal surface area, do not affect the rate of hydrate formation. According to Equation 8.3, the crystal surface area partly determines the liquid-solid mass transfer rate. Since the formation rate is unaffected by the total crystal surface area, the rate of hydrate formation cannot be limited by the liquid-solid mass transfer rate. Similarly, Skovborg and Rasmussen (1994) found, by analyzing the experimental results of Englezos *et al.* (1987a), that the rate of hydrate formation is unaffected by the crystal surface area and can be modeled as a gas-liquid mass transfer process without any particle size distribution.

Impeller power consumption only slightly affects the rate of hydrate formation. The liquid-solid mass transfer coefficient is not directly affected by the superficial gas velocity, but by the power consumption (Grisafi, Brucato and Rizzuti, 1998). Since the rate of hydrate formation is strongly affected by the superficial gas velocity and slightly affected by the power consumption, it is believed that the gas-liquid mass transfer rate dominates over the liquid-solid mass transfer rate. Thus, in the bubble-to-crystal model, the overall mass transfer coefficient for the hydrate process can be represented by an expression for the volumetric gas-liquid mass transfer coefficient where the constants are determined by fitting the measured gas consumption rates to the model.

The bubble-to-crystal model is based on the assumption that a gas dissolution process occurs as a part of the hydrate formation process; that is, the gas must dissolve in water to form hydrate. The images of hydrate crystals in Chapter 6 indicate just that. The hydrate crystals were observed after the reactor and the separator, where the excess gas was separated from the hydrate-water slurry. Some microbubbles that had not been separated were observed. The alternative to gas dissolution could have been the formation of a hydrate layer at the gas-liquid interface that prevented further gas dissolution, but apparently, the microbubbles were not observed to be covered with such a hydrate layer. Also, the produced hydrates were observed to float in the water phase and not being attached to a gas bubble. Therefore, the gas cannot be supplied directly from the gas phase, and the hydrate crystals must grow from gas dissolved in the liquid phase.

Comparing the overall mass transfer coefficient in the bubble-to-crystal model with the volumetric gas-liquid mass transfer coefficients from the literature

(Section 8.6), the overall mass transfer coefficient is higher and more dependent on the superficial gas velocity than the literature coefficients. Furthermore, the measured rates of methane hydrate formation are up to one order of magnitude higher than the maximum gas-liquid mass transfer rates calculated from literature data. In Section 8.6, several explanations for the discrepancy were proposed. The bubble dynamics in the presence of hydrates is expected to be complex, but information about the behaviour of the bubbles in the reactor is not available. In the literature, no correlation for the volumetric mass transfer coefficient for methane-water systems is available for comparison. Reported solubilities of methane in water at high pressure and low temperature diverge, especially in the presence of hydrates. Thus, it is difficult to point out the main reason for the differences observed. Nevertheless, the bubble-to-crystal model and the comparison with established correlations and maximum dissolution rate have identified differences between the hydrate formation process and a typical gas dissolution process in a continuous stirred tank reactor.

The simple model was chosen to represent all the transport processes in the reactor. Thus, it is not expected that the bubble-to-crystal model takes into account all the physical processes during hydrate formation, the bubble dynamics and the heat balance, for example. Still, the bubble-to-crystal model predicts the rate of methane hydrate formation within ±30 %, and is simple and easy to use. The investigated effects that were found significant are included. A calculation of the driving force requires only information about the experimental temperature and pressure and the hydrate equilibrium temperature.

9.2 Mass transfer in reactor

In the present experiments, the gas consumption rate ranged from 8.7 (experiment 6b) to 200.8 Nl/min (experiment 17a). These gas consumption rates correspond to volumetric gas flow rates per liquid volume (9.5 litre) of 0.92 and 21.1 Nl min^{-1} dm^{-3}. Compared to the gas consumption rates from the literature shown in Table 2.1 on page 19, the present hydrate formation rates are high, up to one order of magnitude higher than the highest rate reported. The effect of gas injection rate was not investigated in the studies presented in Table 2.1. By operating in continuous mode, the present and previous (Parlaktuna and Gudmundsson, 1998a, 1998b) experiments have identified the gas injection rate as an important parameter for the hydrate formation rate.

The maximum methane gas consumption rate at 200.8 Nl/min corresponds to a production of 1.9 tonne of methane hydrate per day, assuming that one m^3 of hydrate contains 150 Sm^3 of gas and that the density of the hydrates is 0.9 tonne per m^3 hydrate. The experimental conditions and the reactor geometry were not optimized in the present experiments, and therefore, the reactor is believed to have a considerable potential for increased capacity.

The reactor was operated in the recirculated flow regime. By increasing the superficial gas velocity and thereby obtaining a complete dispersion flow regime (Section 7.4), the hydrate formation rate will increase considerably. For superficial gas velocities up to 0.035 m/s, 400 RPM is sufficient to completely disperse the gas (Section 7.4). Thus, a substantial increase in the stirring rate, that is, the power consumption, is not necessary, but the stirring rate must be accommodated to the superficial gas velocity to obtain complete dispersion of the gas.

The rate of hydrate formation can be improved significantly by increasing the pressure and thereby the gas solubility. Increased pressure results in higher conversion of the gas. Also, at high pressure, the hydrates are formed at a high driving force so that fractionation is suppressed. Levik (2000) found that the gas composition in natural gas hydrates produced with a high driving force is closer to the feed gas composition than the composition in natural gas hydrates produced with a low driving force. Thus, in production of hydrates at higher pressure, the gas recycle rate will decrease due to increased conversion, and the gas composition will change less during the process. The selection of the operating pressure will be a trade-off between the benefits described above and the costs of high pressure reactors and connected equipment.

A mass balance for the reactor, based on standard reactor theory for a CSTR, is presented in Appendix D. Using some of the present and previous experimental conditions, the mass balance predicted the reactor volume typically within ±30 % of the actual reactor volume. A better accuracy cannot be expected since the bubble-to-crystal model predicts the rate of hydrate formation within ±30 %

(Figure 8.8 and Figure 8.9). An example in Appendix D shows that the reactor volume will be reduced to 3.9 litre when the superficial gas velocity is increased to 0.05 m/s. Superficial gas velocities around 0.05 m/s are typically used in industrial reactors (Cropper, 1998). The heat transfer effects were not considered. Operation of the reactor at increased superficial gas velocity requires a smaller reactor volume for the same conversion of the gas. Assuming that the rate of hydrate formation can be predicted by the bubble-to-crystal model at 0.05 m/s and the conversion is correct, a reactor of about 4 litre should be able to produce about 15 tonne per day with 150 Sm^3 of gas per m^3 of hydrate and a hydrate density of 0.9 tonne per m^3 hydrate. The estimate seems optimistic, and it should be noted that the present results are extrapolated and that the heat of formation is not considered.

9.3 Heat transfer in reactor

For an evaluation of the heat transfer in the reactor, a steady-state energy balance is presented in Appendix D. Based on literature data and measured temperatures and conversion, the energy balance predicts the theoretical outlet temperature. For the two examples shown, the measured reactor temperature is close to the theoretical outlet temperature for a CSTR.

The energy balance shows that the heat of hydrate formation is proportional to the conversion and the molar gas injection rate (Equation D.10), and is three orders of magnitude higher than the impeller power consumption (Equation D.13). Thus, by increasing the hydrate formation rate through increased superficial gas velocity, the total heat production will increase proportionally. So far, the heat of formation has efficiently been dissipated in the water resulting in a slight increase in the outlet temperature (about 1 °C). The high heat capacity of water combined with a high molar liquid flow rate compared to the gas heat capacity and the molar gas flow rate (Table D.5), accounts for the slight temperature increase.

Increasing the superficial gas velocity to 0.05 m/s alters the heat production drastically. Using the conditions of experiment 1a in Table D.4, the estimated reactor outlet temperature for 0.05 m/s becomes 68 °C. The hydrate formation process will terminate when the temperature reaches the hydrate equilibrium temperature, which is 10.1 °C at 70 bar for methane (CSMhyd, 1998). For the conditions in experiment 1a, a superficial gas velocity of $2.65 \cdot 10^{-3}$ m/s is sufficient to obtain an outlet temperature equal to the hydrate equilibrium temperature. Thus, to obtain a considerably higher hydrate formation rate, the gas and liquid inlet temperatures should be as close to 0 °C as practical so that a limited temperature increase in the reactor is allowed.

Increased pressure gives increased hydrate formation rate, but also a higher hydrate equilibrium temperature. By using a natural gas mixture, a higher temperature can be accepted since the hydrate equilibrium temperature at 70 bar is 17.5 °C (CSMhyd, 1998). On the other hand, the heat of formation of natural gas mixture hydrate is higher than for methane hydrate. Examples of heat of formation are presented in Appendix D. The calculated heat of formation for natural gas mixture hydrate is about 88 kJ/mol (Figure D.2), while the heat of formation for methane hydrate is about 51.7 kJ/mol (Equation D.11), both at 70 bar. By assuming that the hydrates contain 150 Sm^3 gas per m^3 hydrate, the heat of formation per mass of hydrate becomes 613.9 and 362.7 kJ/kg, respectively (Appendix D on page 180). As discussed in Appendix D, there exists uncertainty about the correct heat of natural gas hydrate formation compared to the heat of methane hydrate formation.

A key parameter in the removal of heat is the liquid flow rate. According to the energy balance, the cooling capacity is increased by increasing the liquid flow rate. Unfortunately, the effect of liquid circulation rate on the rate of hydrate formation was not investigated in the present work. Assuming that the produced hydrate slurry is homogeneous, the liquid rate determines the residence time of the hydrate crystals in the reactor. For the present conditions, pumping rates less than 20 litre/min (the present rate) would have given valuable information about the heat transfer in the reactor and identified any effects on the hydrate formation rate. Higher circulation rates were not necessary at the present conditions because the temperature increase was only about 1 °C.

Based on the energy balance, the hydrate production rate will more likely be limited by the heat transfer rate than the gas-liquid mass transfer rate. The rate of mass transfer is improved by increasing the superficial gas velocity and the pressure. Applying a ring sparger and adding a second impeller will probably increase the formation rate further. Also, a second impeller can reduce the temperature gradients in the reactor. The heat transfer rate can be improved by increasing the liquid flow rate or the relative volume of water to the volume of gas, but then the superficial gas velocity will decrease. If the inlet temperatures of gas and liquid are close to 0 °C, a higher heat production can be allowed. The optimal operating conditions will have to be a trade-off between a high hydrate formation rate and efficient heat transfer.

9.4 Reactor scale-up

The present operational experience with the reactor demonstrates that the potential production capacity is considerably higher than achieved so far. The capacity is currently limited by the upstream gas injection system and the downstream separator. For continuous production of hydrates, a much larger separator is needed for the produced hydrates. In many of the present experiments, the rate of hydrate formation was so high that the separator was filled with hydrates within a couple of minutes. The present separator volume was the double of the reactor volume.

An important objective of the present experiments was to increase the rate of hydrate formation. The rate was increased considerably by increasing the superficial gas velocity, however, the gas injection rate was limited by the gas supply system. A larger gas supply system and a larger gas reservoir will make higher superficial gas velocities possible.

Another method for measuring the gas flow rate should be used to reduce the inaccuracy of the calculated gas injection rates, and thereby the inaccuracy of the gas consumption rate. According to the error analysis in Appendix B and the calculated errors in Appendix A, the maximum errors in gas injection rates are typically four to six times higher than the maximum errors in gas vent rates. Unless the volume of the gas reservoir is more accurately determined, another method to measure the gas injection flow rate should be used.

The mass balance (Appendix D) indicates that a larger reactor volume is not necessary to increase the hydrate formation rate considerably. Considering a scale-up of the reactor volume, it is believed that the present reactor can provide much

URN:NBN:no-3342

higher production rates, and be used in a larger process if the separator and the gas injection system are changed. However, since the effects of operational parameters on the heat transfer rate, and thereby the hydrate formation rate, are not well known, the heat transfer must be kept in mind in selection of the reactor volume for the desired hydrate production rate.

In scale-up of stirred tank reactors, parameters that the process is sensitive to should be identified (Section 3.6). The hydrate formation rate is most sensitive to changes in superficial gas velocity, and the modeling indicates that the gas-liquid interfacial area is a crucial parameter. The energy balance has shown that the reactor performance is sensitive to changes in heat transfer parameters at increased hydrate formation rates.

In the present system, the rate of hydrate formation is higher than the maximum gas dissolution rate calculated using correlations from the literature (Section 8.6). Also, the effects of superficial gas velocity and power consumption differ. Thus, correlations for mass transfer coefficients as well as for gas hold-up from the literature should be used with caution.

Upon scale-up of a reactor, to obtain similar flow fields, a taller reactor, but not with a proportionally larger diameter is recommended (Oldshue, 1983). In this way, the reactor volume is increased, but the gas injection rate does not have to increase equally much to obtain the same superficial gas velocity.

10

Conclusions

The formation rate of methane and natural gas hydrate was measured in a 9.5 litre continuous stirred tank reactor at pressures from 70 to 90 bar and temperatures from 7 to 15 °C. The gas injection rate was varied between 25 and 340 Nl/min, the stirring rate between 400 and 800 RPM and the subcooling between 2.5 and 5.5 °C. Hydrate formation rates between 10 and 200 Nl/min were measured, which correspond to a conversion of the gas between 44 and 56 %.

The experimental results show that the rate of hydrate formation is strongly influenced by the gas injection rate and the experimental pressure. Less significant is the effect of stirring rate, and no effect of subcooling is found. No difference between the rates of methane and natural gas hydrate formation is observed. The hydrate formation rate is unaffected by the hydrate crystal concentration. The experimental results show that the rate of hydrate formation is gas-liquid mass transfer limited.

In an empirical model, the relative importance of the investigated parameters are illustrated. The gas injection rate and the stirring rate are expressed in terms of superficial gas velocity and impeller power consumption, respectively, parameters commonly used in analysis of stirred tank reactors. The empirical model was fitted to the measured hydrate formation rates by using multiple non-linear regression.

A steady-state mass transfer model, the bubble-to-crystal model, was developed for the rate of hydrate formation in the continuous stirred tank reactor. The model

URN:NBN:no-3342

describes the mass transfer of gas from the gas bubble to the hydrate crystal surface. The driving force for hydrate formation is the difference in gas concentration at the gas-liquid interface and at the hydrate crystal surface. The concentrations are based on the gas solubility in water at the experimental conditions and at the hydrate equilibrium conditions, respectively. The overall mass transfer coefficient is expressed in terms of superficial gas velocity and impeller power consumption.

The morphology of the produced hydrates was studied by using microscopic imaging. The hydrates were observed to form semi-transparent agglomerates consisting of elongated crystal units of about 5 µm in diameter and 10 µm long.

The present reactor has a considerable potential for increased capacity. By increasing the superficial gas velocity or the pressure, the rate of hydrate formation will increase considerably. However, an increase in the rate of hydrate formation will be limited by the heat of hydrate formation. The reactor performance is sensitive to changes in the gas flow rate and the liquid flow rate, which influence the hydrate formation rate and the heat transfer rate, respectively.

The experimental results, the models and the operational experience are of importance in design and operation of a large scale hydrate production process. Dominating effects and sensitive process parameters are identified. In large scale continuous production, the capacities of the upstream gas supply system and the downstream separator must be increased in proportion to the reactor capacity.

11

Further work

For a better understanding of the reactor performance in production of hydrates, the following tasks are recommended in further work:

- Increase the capacity of the reactor, by applying another gas supply system and separator. Then, investigate the effect of increased superficial gas velocity.
- Investigate the effect of liquid circulation rate on the rate of hydrate formation at higher formation rates so that heat transfer becomes significant. Document the effect of liquid circulation rate on the reactor temperature and the heat production.
- Improve the quality of microscope images and install the high pressure flow cell in a by-pass downstream of the reactor. More knowledge about the hydrate crystal morphology and agglomerating behaviour is desirable in product control and design of separation equipment.

URN:NBN:no-3342

References

Andersson, V., *Flow properties of natural gas hydrate slurries, An experimental study*, Dr.ing. thesis, Norwegian University of Science and Technology, 156 pp., 1999.

Arai, T., Kato, Y., Ebinuma, T., Uchida, T., Narita, H. and Matsuo, K., Experiment on formation rate of methane hydrate, *10th International Offshore and Polar Engineering Conference*, Seattle, USA, May 28-June 2, 2000.

Azarnoosh, A. and McKetta, J.J., The solubility of propane in water, *Petroleum Refiner*, **37**, 275-278, 1958.

Bakker, A. and Frijlink, J.J., The drawdown and dispersion of floating solids in aerated and unaerated stirred vessels, *Chemical Engineering Research and Design*, **67**, 2, 208-210, 1989.

Besnard, G., Song, K.Y., Hightower, J.W., Kobayashi, R., Elliot, D. and Chen, R., New method of temperature-ramping, isobaric experiments to study the hydrate formation and decomposition, *213th American Chemical Society National Meeting,* San Francisco, USA, April 13-17, 1997.

Bourgmayer, P., Sugier, A. and Behar, E., A new proposal for solving hydrates problem in multi-phase flow, *4th International Conference on Multi-Phase Flow*, Nice, France, June 19-21, 1989.

Bylov, M., *An experimental study of the nucleation and growth of gas hydrates*, Ph.D. thesis, Technical University of Denmark, 160 pp., 1997.

Chaudhari, R.V. and Ramachandran, P.A., Three phase slurry reactors, *AIChE Journal*, **26**, 2, 177-201, 1980.

Christiansen, R.L. and Sloan, E.D., Jr., Mechanisms and kinetics of hydrate formation, *Annals of the New York Academy of Sciences*, **715**, 283-305, 1994.

Cramer, S.D., Solubility of methane in brines from 0 to 300 °C, *Industrial & Engineering Chemistry. Process design and development*, **23**, 533-538, 1984.

Cropper, S.R., *Review of kinetics and hydrodynamics of hydrate producing reactor,* Technical Report, NGH at NTNU, 39 pp., 1998.

CSMhyd, *The Colorado School of Mines Hydrate Prediction Software,* 1998.

URN:NBN:no-3342

Culberson, O.L and McKetta, J.J., Phase equilibria in hydrocarbon-water systems, *Petroleum Transactions, AIME*, **189**, 1950.

Doebelin, E.O., *Measurement systems, application and design*, 4th ed., McGraw-Hill, 1990.

Englezos, P., Kalogerakis, N., Dholabhai, P.D. and Bishnoi, P.R., Kinetics of formation of methane and ethane gas hydrates, *Chemical Engineering Science,* **42**, 11, 2647-2658, 1987a.

Englezos, P., Kalogerakis, N., Dholabhai, P.D. and Bishnoi, P.R., Kinetics of gas hydrate formation from mixtures of methane and ethane, *Chemical Engineering Science*, **42**, 11, 2659-2666, 1987b.

Englezos, P. and Bishnoi, P.R., Gibbs free energy analysis for the supersaturation limits of methane in liquid water and the hydrate-gas-liquid water phase behavior, *Fluid Phase Equilibria*, **42**, 129-140, 1988.

Flow Calculations (FLUIDAT) V 1.13, *Bronkhorst High-Tech B.V.*, 1994.

Fogler, H.S., *Elements of chemical reaction engineering*, 3rd ed., Prentice-Hall, 1999.

Froment, G.F and Bischoff, K.B., *Chemical reactor analysis and design,* 2nd ed., John Wiley & Sons, 1990.

Gaillard, C., Monfort, J.P. and Peytavy, J.L., Formation and growth kinetics of natural gas hydrate, *2nd International Conference on Natural Gas Hydrates Proceedings*, Toulouse, France, June 2-6, 1996.

Gaillard, C., Monfort, J.P. and Peytavy, J.L., Investigation of methane hydrate formation in a recirculating flow loop: modeling of the kinetics and tests of efficiency of chemical additives on hydrate inhibition, *Oil & Gas Science and Technology -Rev. IFP*, **54**, 3, 365-374, 1999.

Grisafi, F., Brucato, A. and Rizzuti, L., Solid-liquid mass transfer coefficients in gas-solid-liquid agitated vessels, *The Canadian Journal of Chemical Engineering*, **76**, 446-455, 1998.

Gudmundsson, J.S., Method and equipment for production of gas hydrate, Norwegian Patent 172080, 1990.

Gudmundsson, J.S., Parlaktuna, M. and Khokhar, A.A., Storage of natural gas as frozen hydrate, *SPE 67th Annual Technical Conference & Exhibition*, SPE paper 24924, Washington D.C., USA, October 4-7, 1992.

Gudmundsson, J.S., Parlaktuna, M. and Khokhar, A.A., Storing natural gas as frozen hydrate, *SPE Production and Facilities,* 69-73, February 1994.

Gudmundsson, J.S. and Børrehaug, A., Frozen hydrate for transport of natural gas, *2nd International Conference on Natural Gas Hydrates Proceedings*, Toulouse, France, June 2-6, 1996.

Gudmundsson, J.S., Andersson, V., Levik, O.I. and Parlaktuna, M., Hydrate concept for capturing associated gas, *SPE European Petroleum Conference*, SPE paper 50598, The Hague, The Netherlands, October 20-22, 1998.

Gudmundsson, J.S., Graff, O.F., Hove, A.M. and Laading, G., Natural gas hydrate (NGH) technology for stranded gas, *IBC Remote Gas Utilization*, London, U.K., December 1, 1999.

Gumerov, N.A. and Chahine, G.L., Dynamics of bubbles in conditions of gas hydrate formation, *8th International Offshore and Polar Engineering Conference*, Montréal, Canada, May 24-29, 1998.

Han, X., Wang, S., Chen, X. and Liu, F., Surfactant accelerates gas hydrate formation, *Proceedings of The Fourth International Conference on Gas Hydrates*, Yokohama, Japan, May 19-23, 2002.

Handa, Y.P., Compositions, enthalpies of dissociation, and heat capacities in the range 85 to 270 K for clathrate hydrates of methane, ethane, and propane, and enthalpy of dissociation of isobutane hydrate, as determined by a heat-flow calorimeter, *Journal of Chemical Thermodynamics*, **18**, 915-921, 1986.

Handa, Y.P., Effect of hydrostatic-pressure and salinity on the stability of gas hydrates, *Journal of Physical Chemistry*, **94**, 6, 2652-2657, 1990.

Happel, J., Hnatow, M.A. and Meyer, H., The study of separation of nitrogen from methane by hydrate formation using a novel apparatus, *Annals of the New York Academy of Sciences*, **715**, 412-424, 1994.

Henriksen, L.V., AGA AS, personal communication, 2001.

Herri, J.M., Gruy, F., Cournil, M., Di Benedetto, D. and Breuil, P., A new experimental set-up for the characterization in situ of methane hydrate formation, *2nd International Conference on Natural Gas Hydrates Proceedings*, Toulouse, France, June 2-6, 1996a.

Herri, J.M., Gruy, F. and Cournil, M., Kinetics of methane hydrate formation, *2nd International Conference on Natural Gas Hydrates Proceedings*, Toulouse, France, June 2-6, 1996b.

Herri, J.M., Pic, J.S., Gruy, F. and Cournil, M., Methane hydrate crystallization mechanism from in-situ particle sizing, *AIChE Journal*, **45**, 3, 590-602, 1999.

Himmelblau, D.M., Solubilities of inert gases in water, 0 °C to near the critical point of water, *Journal of Chemical and Engineering Data*, **5**, 1, 10-15, 1960.

Hirata, A. and Mori, Y.H., How liquids wet clathrate hydrates: some macroscopic observations, *Chemical Engineering Science*, **53**, 14, 2641-2643, 1998.

Holder, G., Zetts, S. and Pradhan, N., Phase behaviour in systems containing clathrate hydrates, A Review, *Reviews in Chemical Engineering*, **5**, 1-4, 1-70, 1988.

Holder, G.D. and Bishnoi, P.R., eds., Gas hydrates: challenges for the future, *Annals of the New York Academy of Sciences*, **912**, 2000.

Irvin, G., Li, S., Simmons, B., John, V., McPherson, G., Max, M. and Pellenbarg, R., Control of gas hydrate formation using surfactant systems, underlying concepts and new applications, *Annals of the New York Academy of Sciences*, **912**, 515-526, 2000.

Karaaslan, U. and Parlaktuna, M., Effect of surfactants on hydrate formation rate, *Annals of the New York Academy of Sciences*, **912**, 735-743, 2000.

Knox, W.G., Hess, M., Jones, G.E. and Smith Jr., H.B., The hydrate process, *Chemical Engineering Progress*, **57**, 2, 66-71, 1961.

Kobayashi, R. and Katz, D.L., Vapor-liquid equilibria for binary hydrocarbon-water systems, *Industrial Engineering and Chemistry*, **45**, 2, 440-451, 1953.

Kvamme, B., Mechanisms for initiation of hydrate from liquid water, liquid phase clustering, surface adsorption, or what?, *Annals of the New York Academy of Sciences*, **715**, 306-310, 1994.

URN:NBN:no-3342

Kvamme, B., A new theory for the kinetics of hydrate formation, *2nd International Conference on Natural Gas Hydrates Proceedings*, Toulouse, France, June 2-6, 1996.

Kvamme, B., A unified nucleation theory for the kinetics of hydrate formation, *Annals of the New York Academy of Sciences*, **912**, 496-501, 2000.

Kvamme, B., Initiation and growth of hydrate, *Proceedings of The Fourth International Conference on Gas Hydrates*, Yokohama, Japan, May 19-23, 2002.

Larsen, R., Lund, A., Andersson, V. and Hjarbo, K.W., Conversion of water to hydrate particles, *2001 SPE Annual Technical Conference and Exhibition*, SPE paper 71550, New Orleans, USA, September 30-October 3, 2001.

Lekvam, K. and Ruoff, P., A reaction kinetic mechanism for methane hydrate formation in liquid water, *Journal of American Chemical Society*, **115**, 8565-8569, 1993.

Lekvam, K. and Bishnoi, P.R., Dissolution of methane in water at low temperatures and intermediate pressures, *Fluid Phase Equilibria*, **131**, 297-309, 1997.

Levik, O.I., *Thermophysical and compositional properties of natural gas hydrate*, Dr.ing. thesis, Norwegian University of Science and Technology, 164 pp., 2000.

Lide, D.R., *CRC handbook of chemistry and physics*, 71st ed., CRC Press, 1990.

Maalej, S., Benadda, B. and Otterbein, M., Influence of pressure on the hydrodynamics and mass transfer parameters of an agitated bubble reactor, *Chemical Engineering and Technology*, **24**, 77-84, 2001.

Makogon, Y.F., *Hydrates of hydrocarbons*, PennWell Books, 1997.

Makogon, Y.F., Makogon, T.Y. and Holditch, S.A., Gas hydrate formation and dissociation with thermodynamic and kinetic inhibitors, *SPE Annual Technical Conference and Exhibition*, SPE paper 56568, Houston, USA, October 3-6, 1999.

Maksimov, A.M., *Thermophysical properties of hydrates, Experimental studies*, Technical report, Russian Academy of Sciences, 29 pp., 1996.

Miyata, K., Okui, T., Hirayama, H., Ihara, M., Yoshikawa, K. and Nagayasu, H., Iwasaki, S., Kimura, T., Kawasaki, T., Kikuchi, K. and Terasaki, D., A challenge to high-rate industrial production of methane hydrate, *Proceedings of The Fourth International Conference on Gas Hydrates*, Yokohama, Japan, May 19-23, 2002.

Monfort, J.P. and Nzihou, A., Light scattering kinetics study of cyclopropane hydrate growth, *Journal of Crystal Growth*, **128**, 1182-1186, 1993.

Monfort, J.P., ed., *2nd International Conference on Natural Gas Hydrates Proceedings*, Toulouse, France, June 2-6, 1996.

Monfort, J.P., Jussaume, L., El Hafaia, T. and Canselier, J.P., Kinetics of gas hydrate formation and tests of efficiency of kinetic inhibitors, experimental and theoretical approaches, *Annals of the New York Academy of Sciences*, **912**, 753-765, 2000.

Moran, M.J. and Shapiro, H.N., *Fundamentals of engineering thermodynamics*, 2. ed., John Wiley & Sons, 1993.

Mori, Y.H., ed., *Proceedings of The Fourth International Conference on Gas Hydrates*, Yokohama, Japan, May 19-23, 2002.

Mullin, J.W., *Crystallization*, 3rd ed., Butterworth-Heinemann, 1993.

Narita, H. and Uchida, T., Studies on formation/dissociation rates of methane hydrates, *2nd International Conference on Natural Gas Hydrates Proceedings*, Toulouse, France, June 2-6, 1996.

Natarajan, V., Bishnoi, P.R. and Kalogerakis, N., Induction phenomena in gas hydrate nucleation, *Chemical Engineering Science*, **49**, 13, 2075-2087, 1994.

Nerheim, A.R., Svartaas, T.M. and Samuelsen, E.K., Investigation of hydrate kinetics in the nucleation and early growth phase by laser light scattering, *2nd International Offshore and Polar Engineering Conference*, San Francisco, USA, June 14-19, 1992.

Nocentini, M., Fajner, D., Pasquali, G. and Magelli, F., Gas-liquid mass transfer and holdup in vessels stirred with multiple Rushton turbines: water and water-glycerol solutions, *Industrial and Engineering Chemistry Research*, **32**, 19-26, 1993.

URN:NBN:no-3342

Oguz, H., Brehm, A. and Deckwer, W.D., Gas/liquid mass transfer in sparged agitated slurries, *Chemical Engineering Science*, **42**, 7, 1815-1822, 1987.

Oldshue, J.Y., *Fluid mixing technology*, Chemical Engineering McGraw-Hill, 1983.

Ozkan, O., Calimli, A., Berber, R. and Oguz, H., Effect of inert solid particles at low concentrations on gas-liquid mass transfer in mechanically agitated reactors, *Chemical Engineering Science*, **55**, 2737-2740, 2000.

Pangborn, J.B. and Barduhn, A.J., The kinetics of methyl bromide hydrate formation, *Desalination,* **8**, 35-68, 1970.

Parlaktuna, M. and Gudmundsson, J.S., *Gas-in-ice, formation rate and gas content*, Technical Report, NGH at NTNU, 53 pp., 1995.

Parlaktuna, M. and Gudmundsson, J.S., Formation rate of methane and mixture hydrate, *2nd International Conference on Natural Gas Hydrates Proceedings*, Toulouse, France, June 2-6, 1996.

Parlaktuna, M. and Gudmundsson, J.S., *Continuous production rate of hydrate, effect of RPM, pressure and gas injection rate*, Technical Report, NGH at NTNU, 22 pp., 1998a.

Parlaktuna, M. and Gudmundsson, J.S., *Continuous production rate of hydrate, effect of sub-cooling and gas injection rate,* Technical Report, NGH at NTNU, 22 pp., 1998b.

Parlaktuna, M., Program *Bottle*, Department of Petroleum Engineering and Applied Geophysics, NTNU, 1998.

Perry, R.H. and Green, D., *Perry's chemical engineer's handbook*, 6th ed., McGraw-Hill, 1984.

Pic, J.S., Herri, J.M. and Cournil, M., Mechanisms of methane hydrate crystallization in a semibatch reactor, influence of a kinetic inhibitor: polyvinylpyrrolidone, *Annals of the New York Academy of Sciences*, **912**, 832-842, 2000.

POLYMATH 5.1, *CACHE Corporation, University of Connecticut, Ben Gurion University of the Negev and The University of Michigan,* 2002.

PVTsim 11.0, *Calsep A/S*, 2001.

Randolph, A.D. and Larson, M.A., *Theory of particulate processes, analysis and techniques of continuous crystallization*, 2nd ed., Academic Press, 1988.

Reid, R.C., Prausnitz, J.M. and Poling, B.E., *The properties of gases and liquids,* 4th ed., McGraw-Hill, 1987.

Rodger, P.M., Stability of gas hydrates, *Journal of Physical Chemistry*, **94**, 6080-6089, 1990.

Rogers, R.E., Kothapalli, C. and Lee, M.S., Influence of microbes on gas hydrate formation in porous media, *Proceedings of The Fourth International Conference on Gas Hydrates*, Yokohama, Japan, May 19-23, 2002.

Skovborg, P., *Gas hydrate kinetics*, Ph.D. thesis, Technical University of Denmark, 238 pp., 1993.

Skovborg, P., Ng, H.J., Rasmussen, P. and Mohn, U., Measurement of induction times for the formation of methane and ethane gas hydrates, *Chemical Engineering Science*, **48**, 3, 445-453, 1993.

Skovborg, P. and Rasmussen, P., A mass transport limited model for the growth of methane and ethane gas hydrates, *Chemical Engineering Science*, **42**, 11, 1131-1143, 1994.

Sloan, E.D., Jr. and Fleyfel, F., A molecular mechanism for gas hydrate nucleation from ice, *AIChE Journal*, **37**, 9, 1281-1292, 1991.

Sloan, E.D., Jr., Happel, J. and Hnatow, M., eds., International Conference on Natural Gas Hydrates, *Annals of the New York Academy of Sciences*, **715**, 1994.

Sloan, E.D., Jr., *Clathrate hydrates of natural gases*, 2nd ed., Marcel Dekker, 1998.

Smith, J.M., Simple performance correlations for agitated vessels, *7th European Conference on Mixing*, Kluwer Academic Publishers, 55-63, 1992.

Song, K.Y., Feneyrou, G., Fleyfel, F., Martin, R., Lievois, J. and Kobayashi, R., Solubility measurements of methane and ethane in water at and near hydrate conditions, *Fluid Phase Equilibria*, **128**, 249-260, 1997.

Stegeman, D., Ket, P.J., Vanderkolk, H.A., Bolk, J.W., Knop, P.A. and Westerterp, K.R., Interfacial area and gas holdup in an agitated gas-liquid reactor under pressure, *Industrial and Engineering Chemistry Research*, **34**, 1, 59-71, 1995.

Takahashi, M., Oonari, H. and Yamamoto, Y., A novel manufacturing method of gas hydrate using the micro-bubble technology, *Proceedings of The Fourth International Conference on Gas Hydrates*, Yokohama, Japan, May 19-23, 2002.

Takano, S., Yamasaki, A., Ogasawara, K., Kiyono, F., Fujii, M. and Yanagisawa, Y., Development of a formation process of CO_2 hydrate particles in a fluidized bed type reactor, *Proceedings of The Fourth International Conference on Gas Hydrates*, Yokohama, Japan, May 19-23, 2002.

Takaoki, T., Iwasaki, T., Katoh, Y., Arai, T. and Horiguchi, K., Use of hydrate pellets for transportation of natural gas -I, advantage of pellet form of natural gas hydrate in sea transportation, *Proceedings of The Fourth International Conference on Gas Hydrates*, Yokohama, Japan, May 19-23, 2002.

Tatterson, G.B., *Fluid mixing and gas dispersion in agitated tanks*, McGraw-Hill, 1991.

Tohidi, B., Danesh, A., Østergaard, K. and Todd, A., The kinetic of structure-H hydrate formation -experimental data and modelling, *2nd International Conference on Natural Gas Hydrates Proceedings*, Toulouse, France, June 2-6, 1996.

Udachin, K.A. and Ripmeester, J.A., A complex clathrate hydrate structure showing bimodal guest hydration, *Nature*, **397**, 420-423, 1999.

Varaminian, F., The role of heat transfer in kinetics of hydrate formation, *Proceedings of The Fourth International Conference on Gas Hydrates*, Yokohama, Japan, May 19-23, 2002.

Vysniauskas, A. and Bishnoi, P.R., A kinetic study of methane hydrate formation, *Chemical Engineering Science*, **38**, 7, 1061-1072, 1983.

Vysniauskas, A. and Bishnoi, P.R., Kinetics of ethane hydrate formation, *Chemical Engineering Science*, **40**, 2, 299-303, 1985.

Wang, Y., Han, B., Yan, H. and Liu, R., Solubility of CH_4 in the mixed solvent *t*-butyl alcohol and water, *Thermochimica Acta*, **253**, 327-334, 1995.

Whitton, M.J., *Gas liquid mixing in tall vessels fitted with multiple impellers*, Ph.D. thesis, Cranfield Institute of Technology, 143 pp., 1992.

Xu, S.A., Feng, L.F., Gu, X.P., Wang, K. and Hu, G.H., Gas-liquid floating particle mixing in an agitated vessel, *Chemical Engineering and Technology*, **23**, 2, 103-113, 2000.

Yousif, M. H., The kinetics of hydrate formation, *SPE 69th Annual Technical Conference and Exhibition*, SPE paper 28479, New Orleans, USA, September 25-28, 1994.

Zhong, Y. and Rogers, R.E., Surfactant effects on gas hydrate formation, *Chemical Engineering Science*, **55**, 4175-4187, 2000.

Østergaard, K.K., Tohidi, B., Danesh, A., Burgass, R.W., Todd, A.C. and Baxter, T., A novel approach for oil and gas separation by using gas hydrate technology, *Annals of the New York Academy of Sciences*, **912**, 832-842, 2000.

Appendix A
Experimental data

During analysis of the experimental results, three plots were made for each experiment:

- temperatures and pressures with time at different locations in the flow loop
- gas bottle pressure drop, gas flow rate in gas vent line, and pressures and temperatures along the gas injection line and gas vent line with time
- calculated gas injection rate, measured gas vent rate and calculated gas consumption rate with time

Examples of the two first plots are shown in Figure A.1 and Figure A.2. For experiments with methane gas, plots of gas injection rate, gas vent rate and gas consumption rate are shown in Figure A.3 to Figure A.22. Plots for experiments with natural gas mixture are shown in Figure A.23 to Figure A.31.

URN:NBN:no-3342

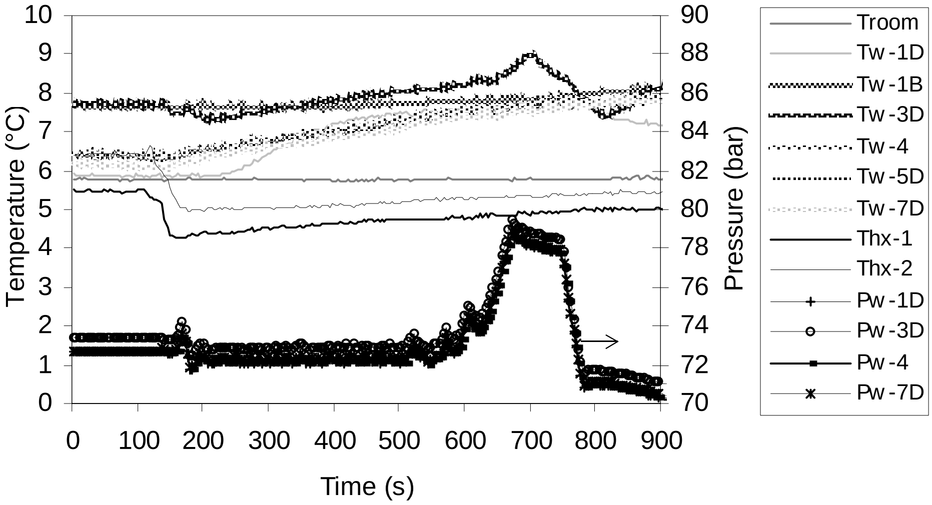

Figure A.1 Measured temperatures and pressures in the flow loop during experiment 7a. Troom was room temperature, Tw-1D to Tw-7D were measured temperatures in the water phase. Thx-1D and Thx-2D were inlet and outlet temperatures of the glycol cooling medium in the heat exchanger. The temperature of both water phase and cooling medium increased slightly with time, meaning that the capacity of heat exchanger was not sufficiently high. Pw-1D to Pw-7D were measured pressures in the water phase. The increase in pressure was due to blocking of the gas vent line causing shutdown of the experiment.

URN:NBN:no-3342

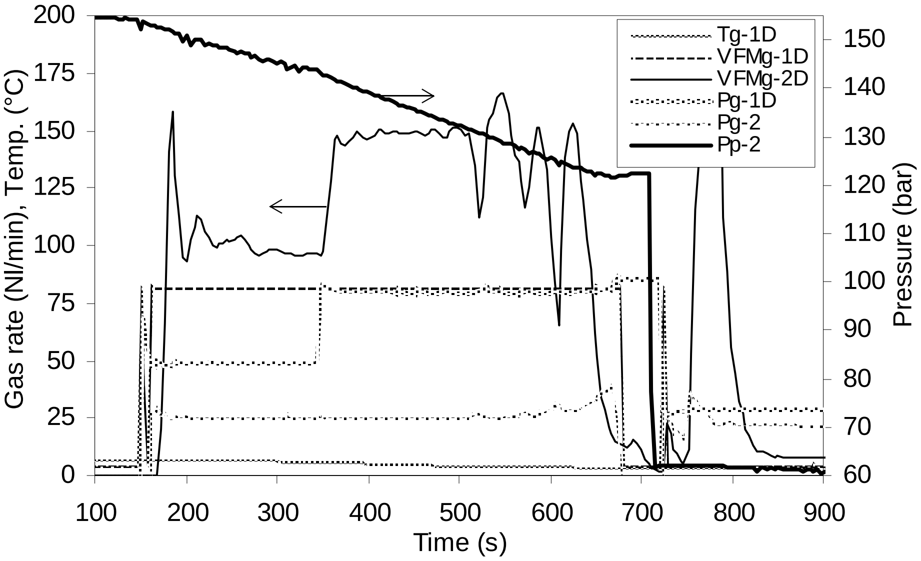

Figure A.2 Gas bottle pressure (Pp-2) and gas vent rate (VFMg-2D) during experiment 7a. Tg-1D was gas injection temperature and VFMg-1D was gas injection rate measured with a gas flow meter. The measured injection rate was constant because the flow meter VFMg-1D had reached its saturation value. Pg-1D was gas pressure at the inlet of the reactor.

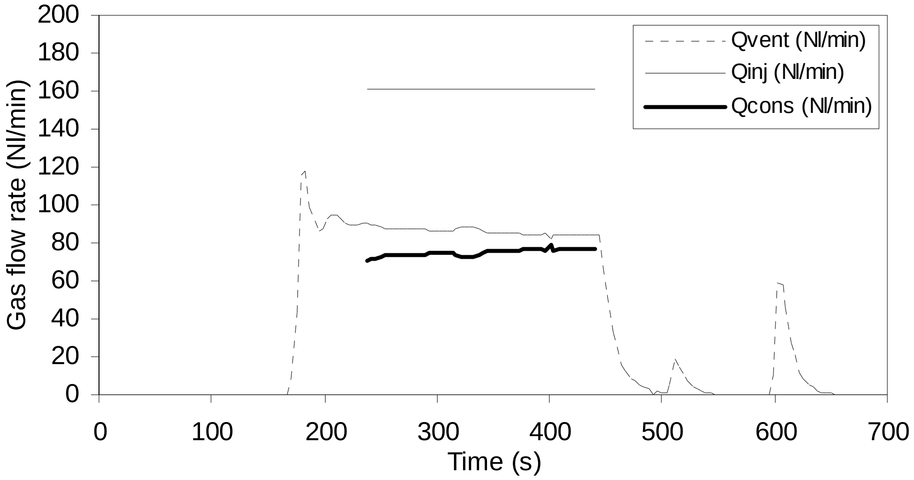

Average Qinj (Nl/min)	Average Qvent (Nl/min)	Average Qcons (Nl/min)	Average reactor temperature (°C)
161.0±10.8	86.0±2.0	74.9±12.8	7.1

Figure A.3 Experiment 1a.

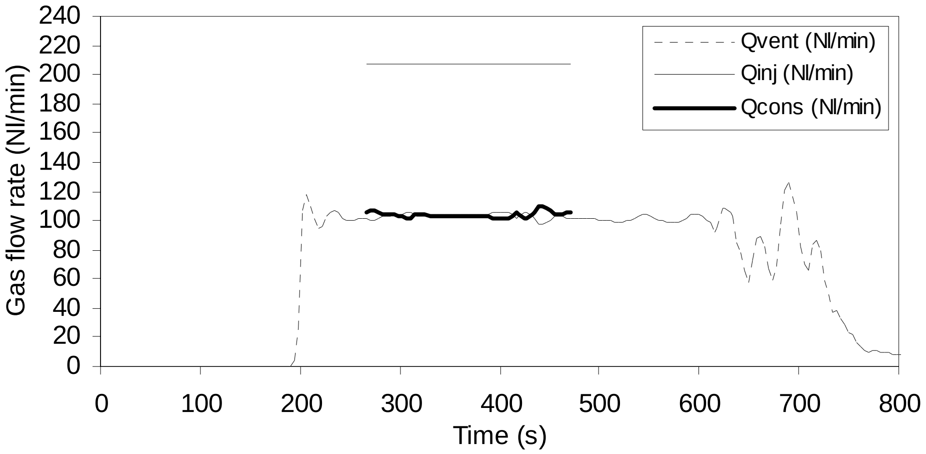

Average Qinj (Nl/min)	Average Qvent (Nl/min)	Average Qcons (Nl/min)	Average reactor temperature (°C)
207.2±11.6	101.4±2.3	103.8±14.0	7.5

Figure A.4 Experiment 2a.

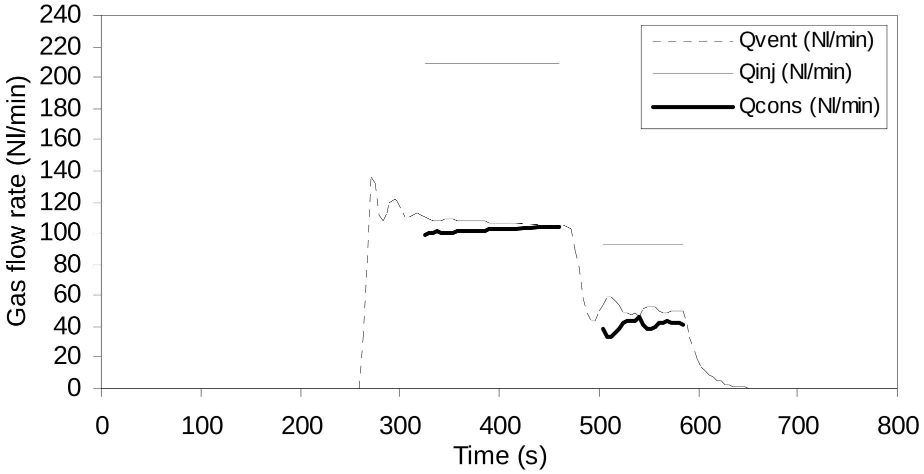

Average Qinj (Nl/min)	Average Qvent (Nl/min)	Average Qcons (Nl/min)	Average reactor tempeature (°C)
209.1±13.7 92.1±7.9	105.3±2.4 50.4±1.8	101.8±16.1 40.7±9.7	7.2 7.2

Figure A.5 Experiment 3a.

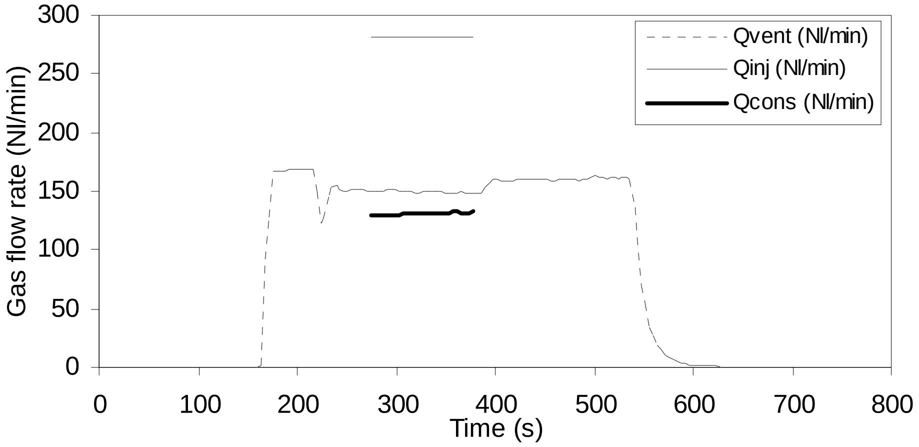

Average Qinj (Nl/min)	Average Qvent (Nl/min)	Average Qcons (Nl/min)	Average reactor tempeature (°C)
280.7±18.8	147.2±3.2	130.9±21.9	7.5

Figure A.6 Experiment 4a.

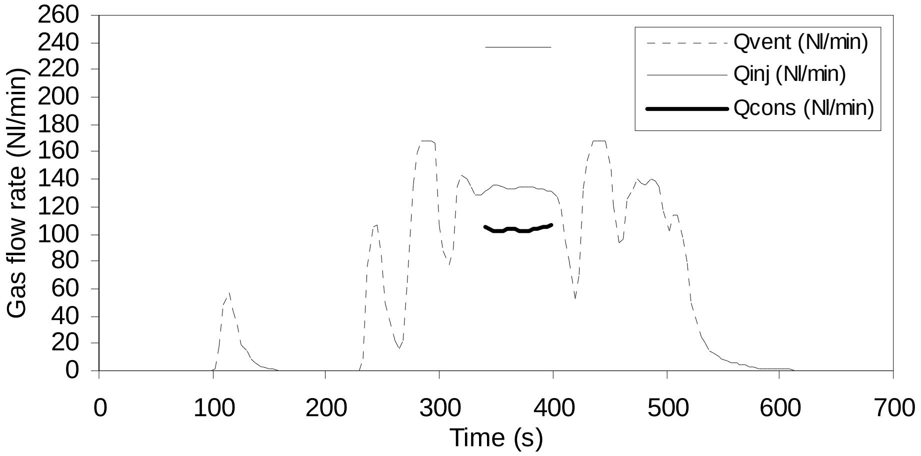

Average Qinj (Nl/min)	Average Qvent (Nl/min)	Average Qcons (Nl/min)	Average reactor tempeature (°C)
237.1±16.0	131.1±3.0	103.6±19.0	7.4

Figure A.7 Experiment 5a.

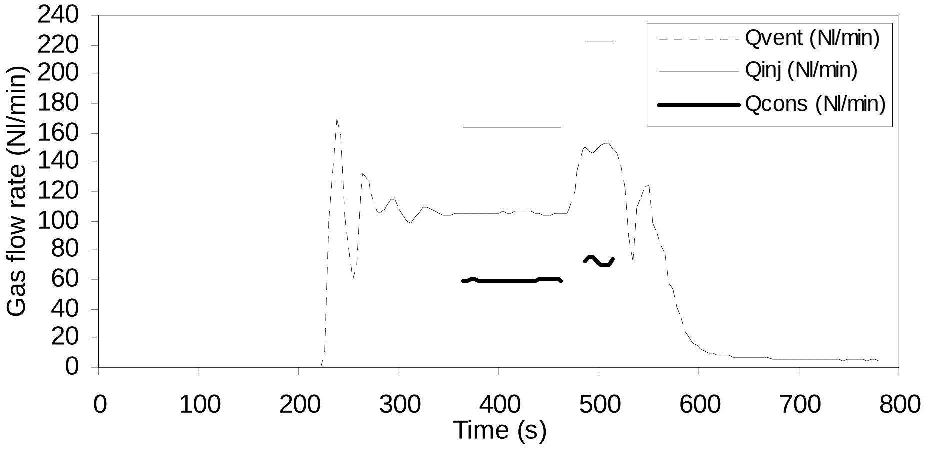

Average Qinj (Nl/min)	Average Qvent (Nl/min)	Average Qcons (Nl/min)	Average reactor tempeature (°C)
164.2±11.8 221.9±20.1	103.4±2.2 147.0±3.9	59.0±14.1 72.3±23.9	7.4 7.5

Figure A.8 Experiment 6a.

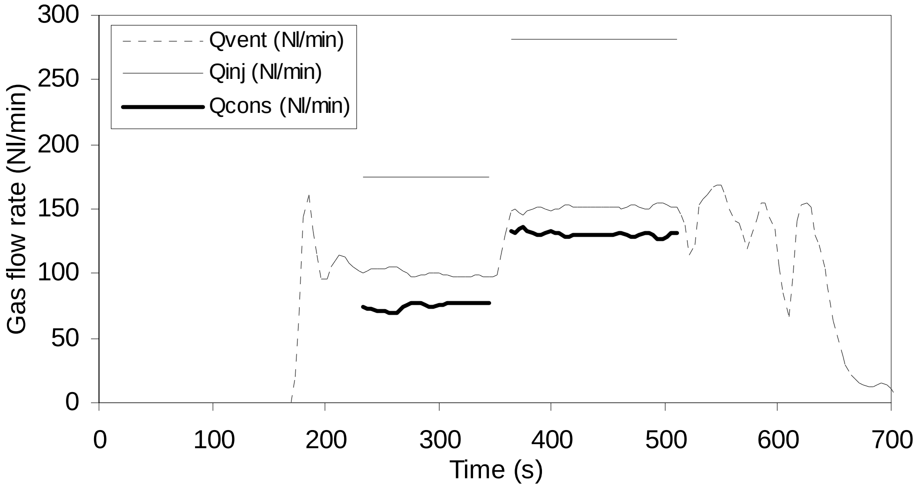

Average Qinj (Nl/min)	Average Qvent (Nl/min)	Average Qcons (Nl/min)	Average reactor tempeature (°C)
175.1±12.6 281.7±16.5	98.5±2.5 148.5±3.3	74.8±15.2 130.5±19.8	7.6 7.7

Figure A.9 Experiment 7a.

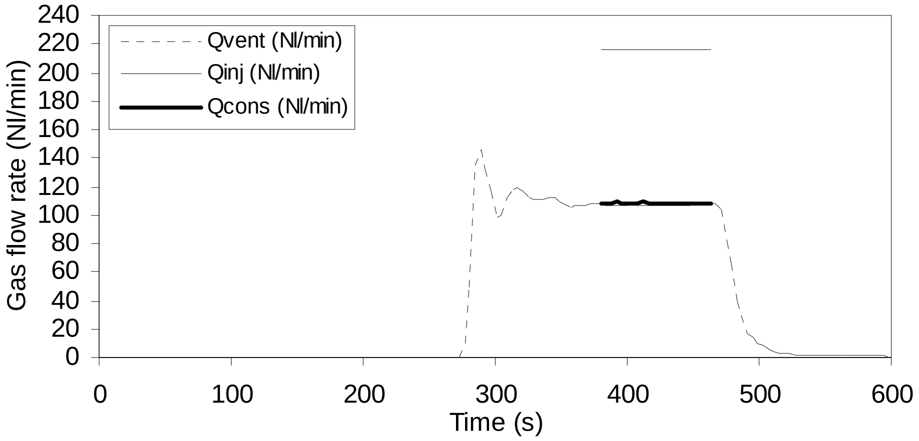

Average Qinj (Nl/min)	Average Qvent (Nl/min)	Average Qcons (Nl/min)	Average reactor tempeature (°C)
215.6±14.0	109.7±2.3	108.4±16.3	7.4

Figure A.10 Experiment 8a.

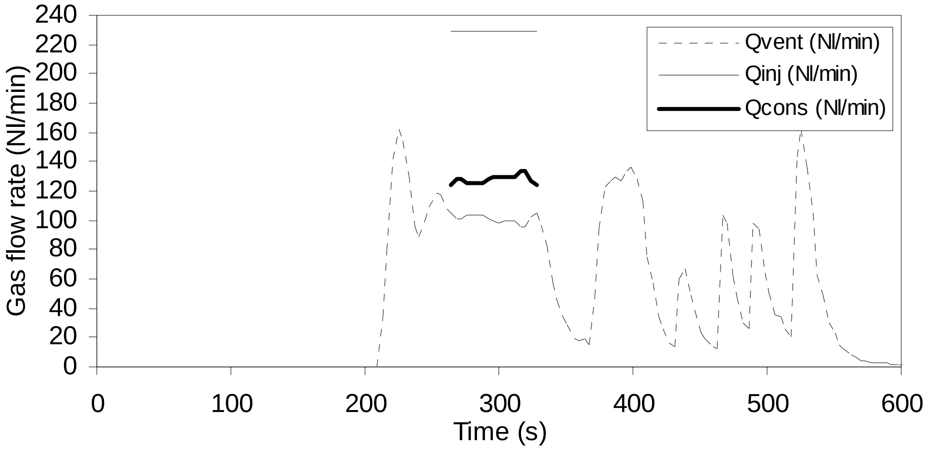

Average Qinj (Nl/min)	Average Qvent (Nl/min)	Average Qcons (Nl/min)	Average reactor tempeature (°C)
228.8±15.3	103.1±2.8	127.9±18.1	7.6

Figure A.11 Experiment 9a.

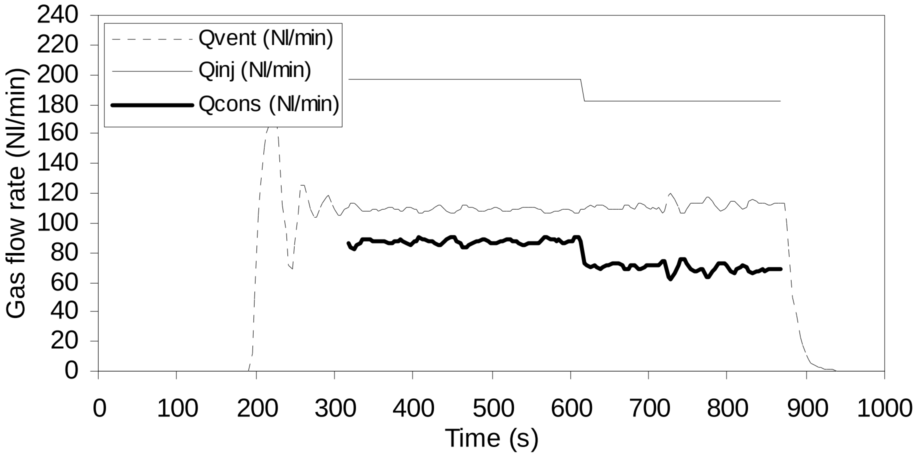

Average Qinj (Nl/min)	Average Qvent (Nl/min)	Average Qcons (Nl/min)	Average reactor tempeature (°C)
196.4±12.4 181.5±11.6	107.1±2.4 109.8±2.6	87.3±14.8 (400 RPM) 69.7±14.2 (600 RPM)	7.2 7.2

Figure A.12 Experiment 10a.

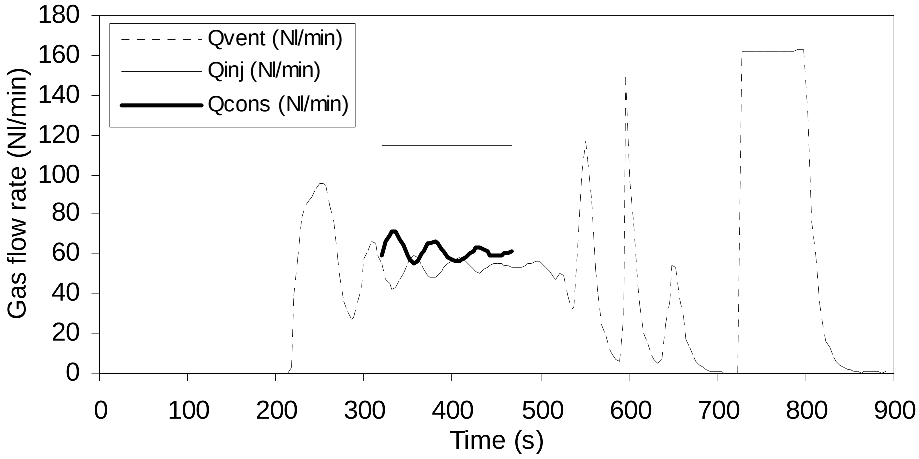

Average Qinj (Nl/min)	Average Qvent (Nl/min)	Average Qcons (Nl/min)	Average reactor tempeature (°C)
114.4±8.2	53.9±1.8	61.6±10.0	7.2

Figure A.13 Experiment 11a.

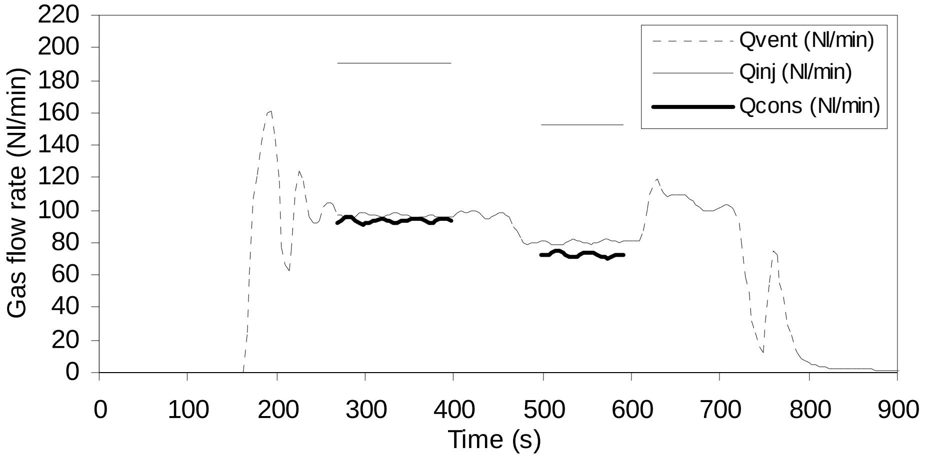

Average Qinj (Nl/min)	Average Qvent (Nl/min)	Average Qcons (Nl/min)	Average reactor tempeature (°C)
190.1±13.1 153.0±11.6	98.8±2.2 82.2±1.9	93.5±15.3 72.6±13.5	7.2 7.6

Figure A.14 Experiment 12a.

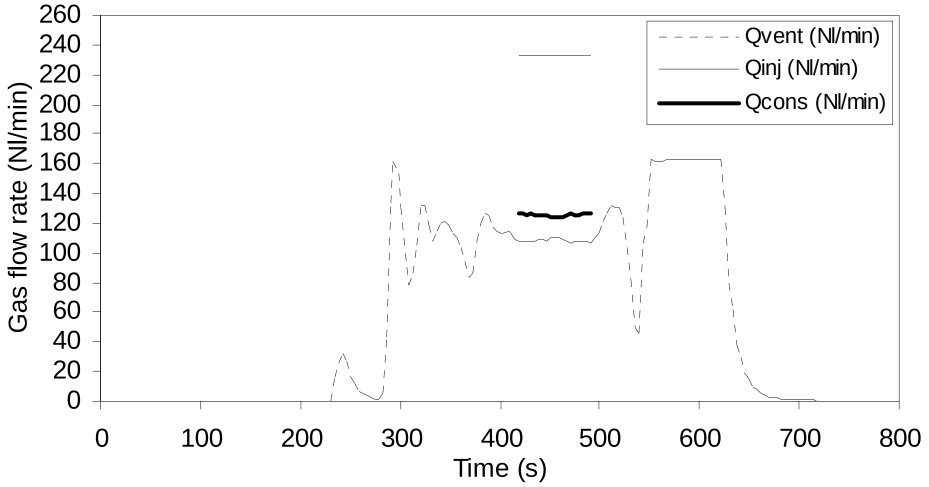

Average Qinj (Nl/min)	Average Qvent (Nl/min)	Average Qcons (Nl/min)	Average reactor tempeature (°C)
233.6±15.1	110.6±2.5	125.4±17.6	8.3

Figure A.15 Experiment 13a.

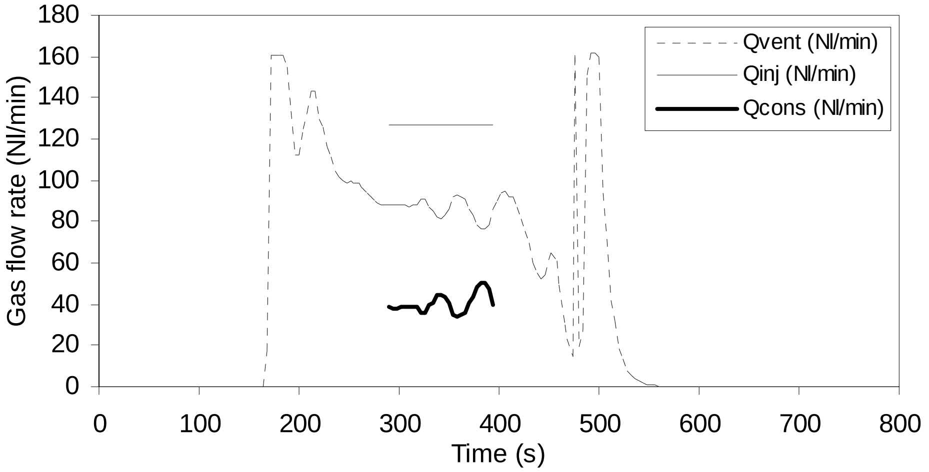

Average Qinj (Nl/min)	Average Qvent (Nl/min)	Average Qcons (Nl/min)	Average reactor tempeature (°C)
126.6±9.0	87.8±2.7	40.5±11.7	7.1

Figure A.16 Experiment 14a.

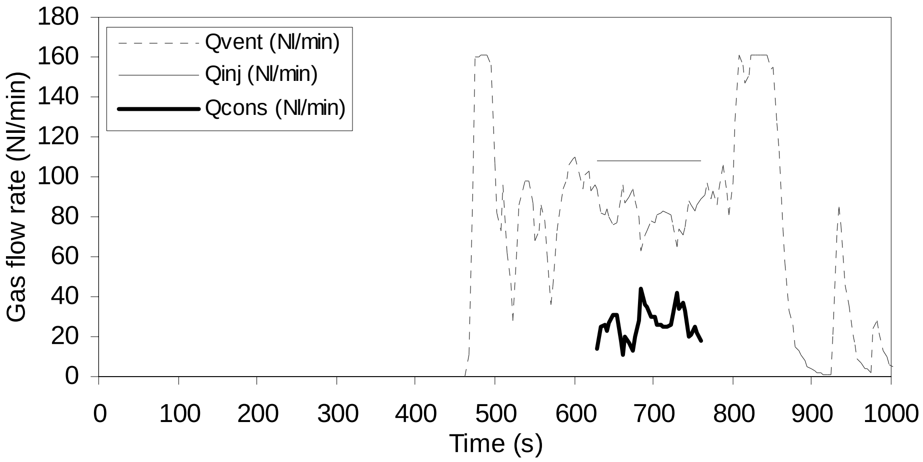

Average Qinj (Nl/min)	Average Qvent (Nl/min)	Average Qcons (Nl/min)	Average reactor tempeature (°C)
107.6±7.4	83.1±3.1	26.3±10.4	7.6

Figure A.17 Experiment 15a.

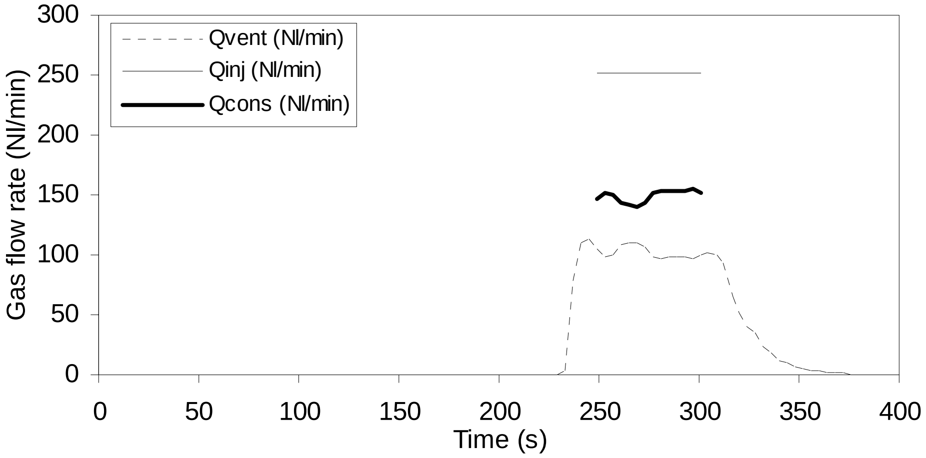

Average Qinj (Nl/min)	Average Qvent (Nl/min)	Average Qcons (Nl/min)	Average reactor tempeature (°C)
251.0±18.2	103.9±3.5	149.1±21.7	7.0

Figure A.18 Experiment 16a.

URN:NBN:no-3342

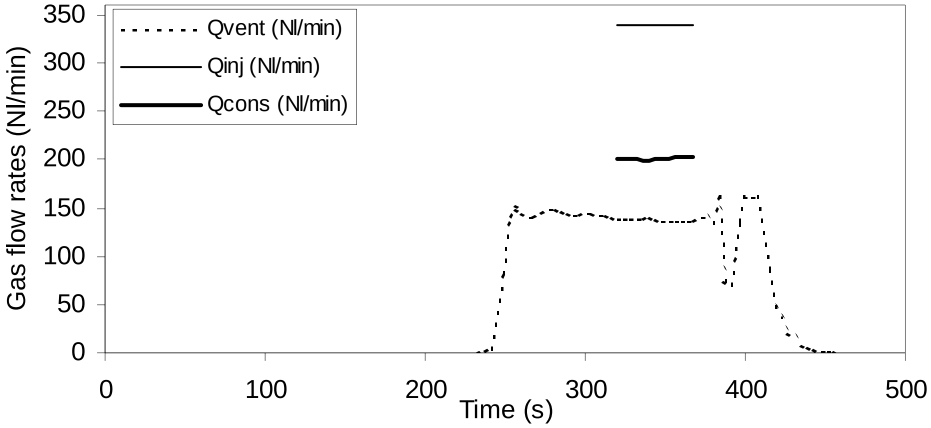

Average Qinj (Nl/min)	Average Qvent (Nl/min)	Average Qcons (Nl/min)	Average reactor tempeature (°C)
339.0±24.3	141.1±3.2	200.8±27.5	7.0

Figure A.19 Experiment 17a.

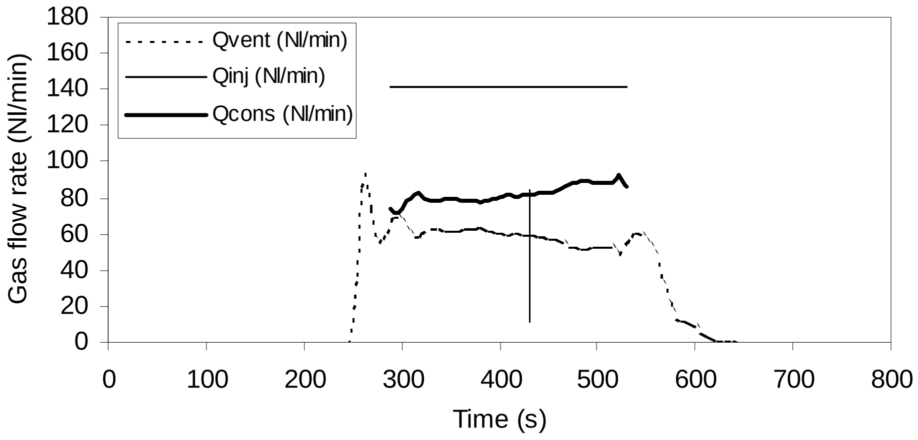

Average Qinj (Nl/min)	Average Qvent (Nl/min)	Average Qcons (Nl/min)	Average reactor tempeature (°C)
141.2±8.9 141.2±8.9	63.6±1.7 53.7±1.2	79.0±10.6 (400 RPM) 88.7±10.1 (800 RPM)	7.0 7.0

Figure A.20 Experiment 18a.

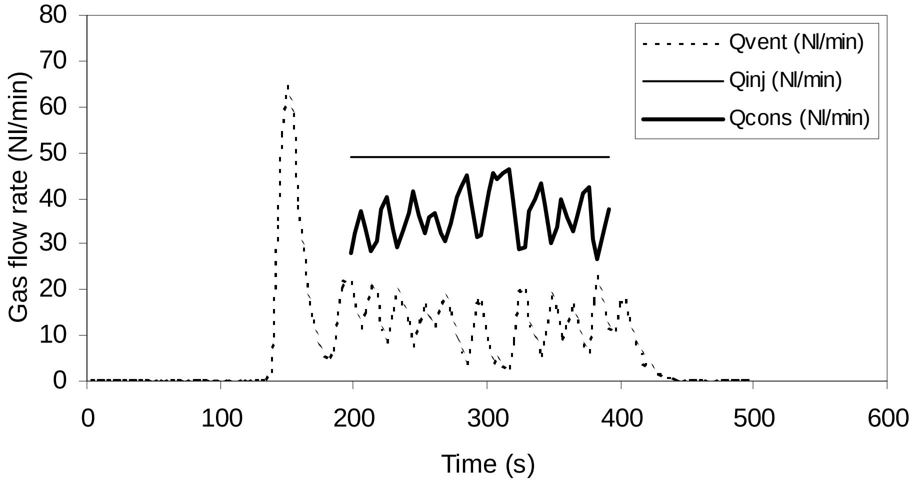

Average Qinj (Nl/min)	Average Qvent (Nl/min)	Average Qcons (Nl/min)	Average reactor tempeature (°C)
49.1±4.1	13.1±1.0	36.2±5.1	7.4

Figure A.21 Experiment 19a.

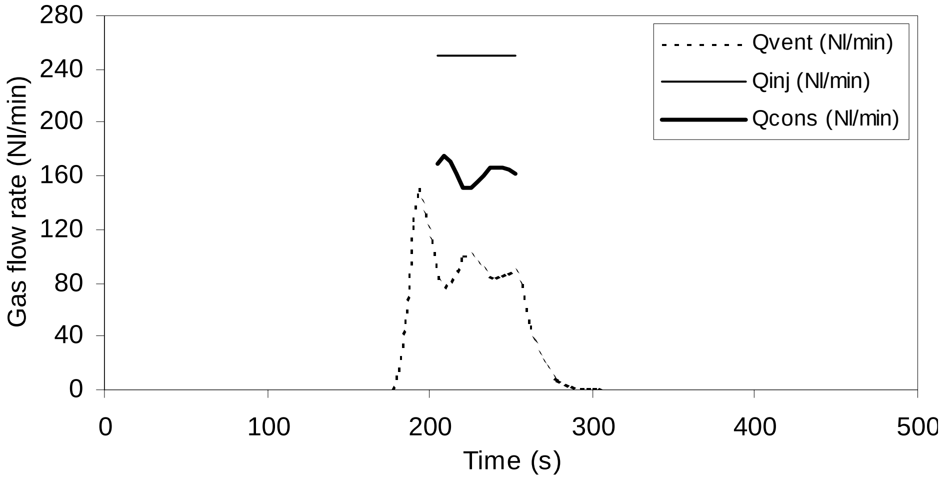

Average Qinj (Nl/min)	Average Qvent (Nl/min)	Average Qcons (Nl/min)	Average reactor tempeature (°C)
250.7±18.2	89.5±3.9	163.0±22.1	7.2

Figure A.22 Experiment 20a.

URN:NBN:no-3342

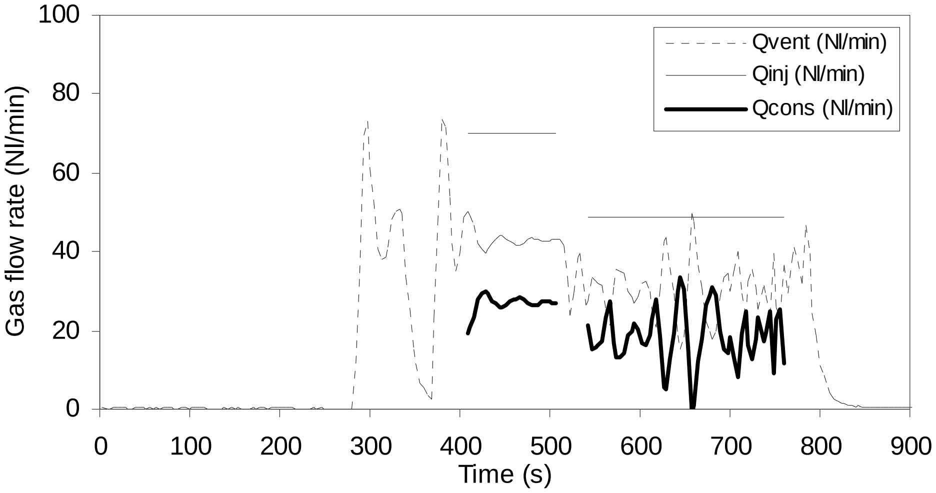

Average Qinj (Nl/min)	Average Qvent (Nl/min)	Average Qcons (Nl/min)	Average reactor tempeature (°C)
69.9±6.8 48.6±3.7	43.2±1.4 30.3±1.7	26.7±8.2 18.4±5.3	12.7 12.6

Figure A.23 Experiment 1b.

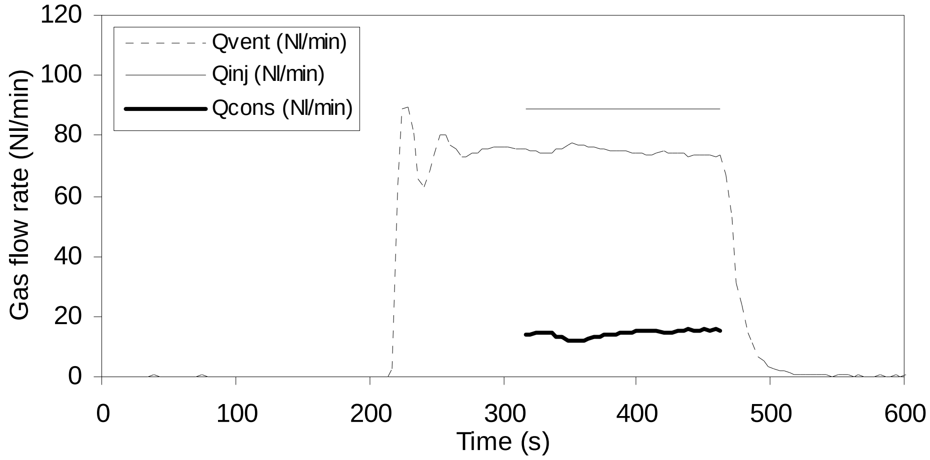

Average Qinj (Nl/min)	Average Qvent (Nl/min)	Average Qcons (Nl/min)	Average reactor tempeature (°C)
89.1±7.6	74.7±1.7	14.3±9.3	12.7

Figure A.24 Experiment 2b.

URN:NBN:no-3342

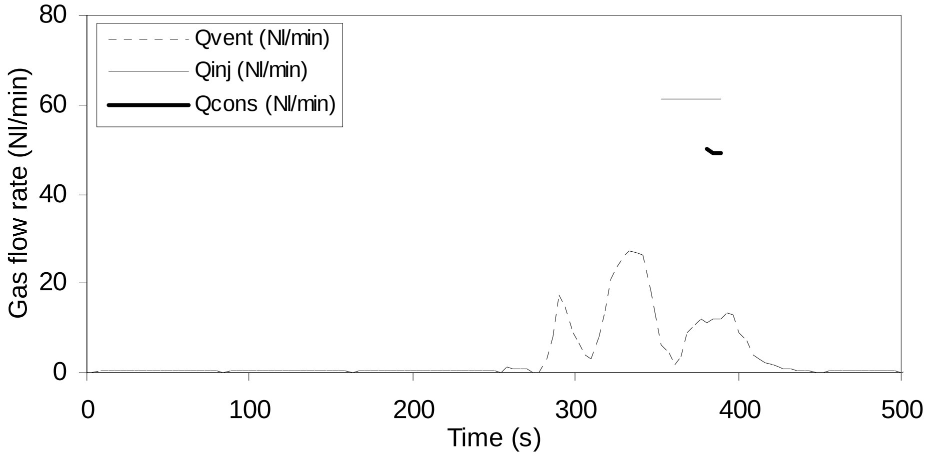

Average Qinj (Nl/min)	Average Qvent (Nl/min)	Average Qcons (Nl/min)	Average reactor tempeature (°C)
61.1±10.5	11.9±0.68	49.3±11.2	14.6

Figure A.25 Experiment 3b.

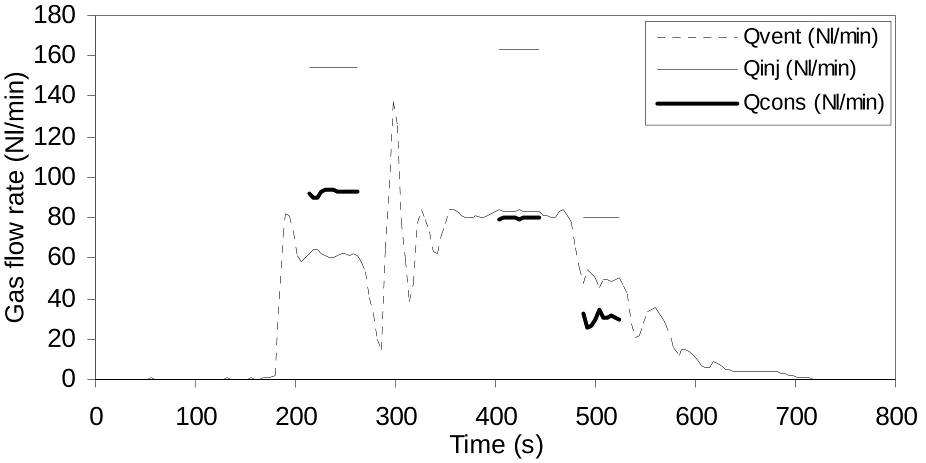

Average Qinj (Nl/min)	Average Qvent (Nl/min)	Average Qcons (Nl/min)	Average reactor tempeature (°C)
154.5±15.4 163.1±16.8 79.9±12.1	61.9±1.7 83.3±1.9 49.7±.1.9	92.6±17.1 79.8±18.7 30.2±14.0	14.4 14.3 14.3

Figure A.26 Experiment 4b.

URN:NBN:no-3342

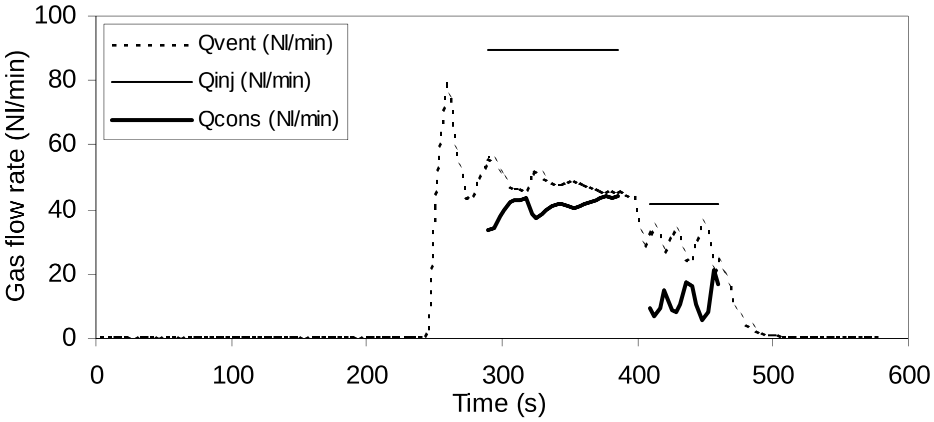

Average Qinj (Nl/min)	Average Qvent (Nl/min)	Average Qcons (Nl/min)	Average reactor tempeature (°C)
89.5±8.7 41.4±6.9	48.7±1.6 29.6±2.0	40.8±10.4 11.8±8.9	14.4 14.4

Figure A.27 Experiment 5b.

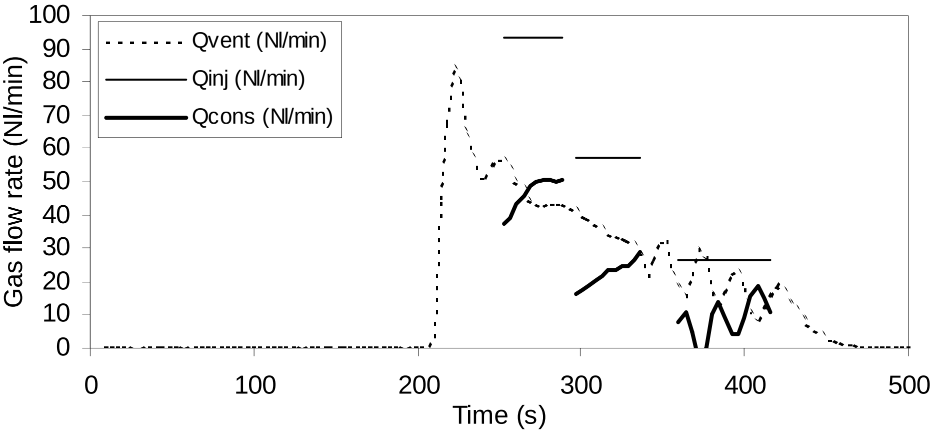

Average Qinj (Nl/min)	Average Qvent (Nl/min)	Average Qcons (Nl/min)	Average reactor tempeature (°C)
93.6±11.6 57.5±8.7 26.6±6.1	47.0±2.8 35.2±2.1 17.9±2.0	46.6±14.4 22.3±10.8 8.7±8.1	14.7 14.6 14.6

Figure A.28 Experiment 6b.

URN:NBN:no-3342

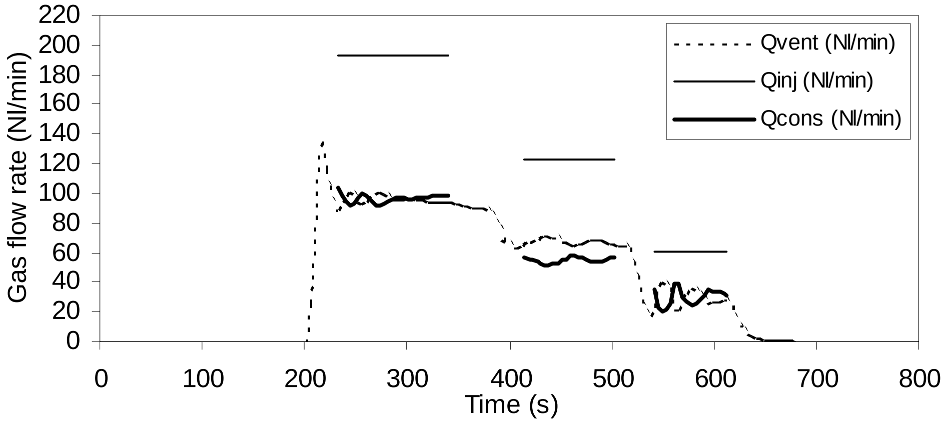

Average Qinj (Nl/min)	Average Qvent (Nl/min)	Average Qcons (Nl/min)	Average reactor tempeature (°C)
192.9±15.6 122.9±11.0 60.5±7.6	96.3±2.6 67.9±1.9 30.5±2.0	96.6±18.2 55.0±12.9 29.9±9.6	14.6 14.6 14.6

Figure A.29 Experiment 7b.

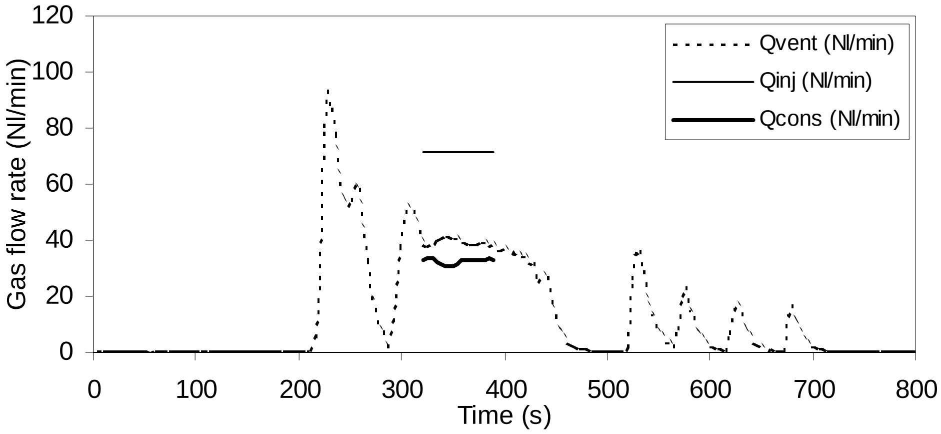

Average Qinj (Nl/min)	Average Qvent (Nl/min)	Average Qcons (Nl/min)	Average reactor tempeature (°C)
71.7±8.3	39.4±1.1	32.3±9.4	14.4

Figure A.30 Experiment 8b.

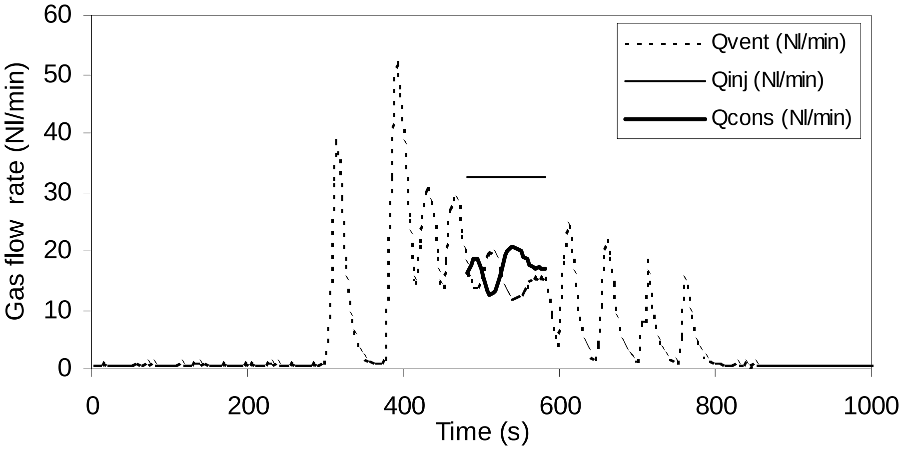

Average Qinj (Nl/min)	Average Qvent (Nl/min)	Average Qcons (Nl/min)	Average reactor tempeature (°C)
32.5±4.5	15.2±0.8	17.3±5.3	14.7

Figure A.31 Experiment 9b.

Appendix B

Error analysis of gas consumption rate

Both measurement errors and errors from calculations affected the overall error in the gas consumption rate. Errors in measured and calculated variables were assumed to have normal distribution and to be statistically independent. Generally, the absolute error in a dependent variable can be found from (Doebelin, 1990):

$$\varepsilon_a = \left|\Delta u_1 \cdot \frac{\partial f}{\partial u_1}\right| + \left|\Delta u_2 \cdot \frac{\partial f}{\partial u_2}\right| + \ldots + \left|\Delta u_n \cdot \frac{\partial f}{\partial u_n}\right| \qquad \text{(B.1)}$$

where the overall error ε_a is in terms of the dependent variable itself.

The gas consumption rate was the difference beween gas injection rate and gas vent rate:

$$Q_{cons} = Q_{inj} - Q_{vent} \qquad \text{(B.2)}$$

The gas injection rate was calculated from PVT data in a gas bottle using the Fortran-program Bottle by Parlaktuna (1998). The gas vent rate was measured with a gas flow meter. These two methods were independent, and therefore, the error in gas consumption rate was the sum of the errors in injection and vent rates:

$$\Delta Q_{cons} = \left|\frac{\partial Q_{cons}}{\partial Q_{inj}} \cdot \Delta Q_{inj}\right| + \left|\frac{\partial Q_{cons}}{\partial Q_{vent}} \cdot \Delta Q_{vent}\right| = \Delta Q_{inj} + \Delta Q_{vent} \qquad \text{(B.3)}$$

URN:NBN:no-3342

B.1 Error in gas injection rate

Bottle (Parlaktuna, 1998) calculated the volume of gas leaving the gas bottle from the inital and final pressure and temperature, the bottle volume and the composition of the gas. The program used the Lee-Kessler equation of state to calculate the z-factor. Assuming no error in recorded time interval, the gas injection rate and its error were:

$$\begin{aligned} Q_{inj} &= \frac{V_{nc}}{t_2 - t_1} \\ \Delta Q_{inj} &= \left| \frac{\partial Q_{inj}}{\partial V_{nc}} \cdot \Delta V_{nc} \right| = \frac{\Delta V_{nc}}{t_2 - t_1} \end{aligned} \tag{B.4}$$

The gas volume V_{nc} at normal conditions (1 atm, 0 °C) and the error in the gas volume were found from:

$$\begin{aligned} V_{nc} &= \frac{n_{diff} R T_{nc}}{p_{nc}} \\ \Delta V_{nc} &= \frac{\Delta n_{diff} R T_{nc}}{p_{nc}} \end{aligned} \tag{B.5}$$

The difference in the amount of gas in the bottle n_{diff} at initial (1) and final (2) conditions was:

$$n_{diff} = n_1 - n_2 \tag{B.6}$$

where

$$n_i = \frac{p_i V_b}{z_i R T_i} \tag{B.7}$$

The bottle temperature was measured before and after the experiment, and the average value was used as input to the program. Thus, T_1 was equal to T_2, and n_{diff} became:

$$n_{diff} = \frac{p_1 V_b}{z_1 R T_1} - \frac{p_2 V_b}{z_2 R T_2} = \frac{V_b}{RT}\left(\frac{p_1}{z_1} - \frac{p_2}{z_2}\right) \tag{B.8}$$

Then, the overall error in n_{diff} was found from:

$$\Delta n_{diff} = \left|\frac{\partial n_{diff}}{\partial V_b}\cdot\Delta V_b\right| + \left|\frac{\partial n_{diff}}{\partial T}\cdot\Delta T\right| + \left|\frac{\partial n_{diff}}{\partial p_1}\cdot\Delta p_1\right| + \left|\frac{\partial n_{diff}}{\partial z_1}\cdot\Delta z_1\right| \quad \text{(B.9)}$$

$$+ \left|\frac{\partial n_{diff}}{\partial p_2}\cdot\Delta p_2\right| + \left|\frac{\partial n_{diff}}{\partial z_2}\cdot\Delta z_2\right|$$

$$= \frac{1}{RT}\left(\frac{p_1}{z_1}-\frac{p_2}{z_2}\right)\Delta V_b + \frac{V_b}{RT^2}\left(\frac{p_1}{z_1}-\frac{p_2}{z_2}\right)\Delta T + \frac{V_b}{RT}\left(\frac{1}{z_1}+\frac{1}{z_2}\right)\Delta p$$

$$+ \frac{p_1 V_b}{z_1^2 RT}\Delta z_1 + \frac{p_2 V_b}{z_2^2 RT}\Delta z_2$$

The error in the z-factor from the Lee-Kessler equation of state was maximum 2% (Reid, Prausnitz and Poling, 1987). Compared to the SRK-Peneloux equation of state (PVTsim, 2001), the Lee-Kessler equation of state underestimated the z-factor at the present pressure and temperature conditions. Therefore, to avoid a systematic error in Δn_{diff}, Δz_1 and Δz_2 were decomposed into a systematic and a random error. The two terms in Equation B.9 containing Δz_1 and Δz_2 changed into:

$$\frac{p_1 V_b}{z_1^2 RT}\Delta z_1 + \frac{p_2 V_b}{z_2^2 RT}\Delta z_2 = \frac{p_1 V_b}{z_1^2 RT}(\Delta z_s + \Delta z_{r1}) + \frac{p_2 V_b}{z_2^2 RT}(-\Delta z_s + \Delta z_{r2}) \quad \text{(B.10)}$$

Assuming a systematic error of 2 % and random error of 0, Equation B.9 became:

$$\Delta n_{diff} = \frac{1}{RT}\left(\frac{p_1}{z_1}-\frac{p_2}{z_2}\right)\Delta V_b + \frac{V_b}{RT^2}\left(\frac{p_1}{z_1}-\frac{p_2}{z_2}\right)\Delta T \quad \text{(B.11)}$$

$$+ \frac{V_b}{RT}\left(\frac{1}{z_1}+\frac{1}{z_2}\right)\Delta p + \frac{V_b}{RT}\left(\frac{p_1}{z_1^2}-\frac{p_2}{z_2^2}\right)\Delta z_s$$

The gas constant was $R = 0.0821$ atm m^3 kg^{-1} K^{-1}. Measurement error in the pressure transducer was ±0.0269 bar (from calibration data). The temperature was measured with ±0.05 °C accuracy.

The volume of the gas bottles was 50 litre with an error of maximum 5 % (Henriksen, 2001). To obtain a more accurate bottle volume V_b, all the bottles were weighed and the pressure and the temperature in the bottles were measured. The gas bottle volume was found by weighing the bottle before use, m_{b1}, which was the weight of the bottle and the gas in the bottle. Pressure and temperature were measured. The bottle, with atmospheric pressure, was weighed again after use, m_{b2}, to find the weight of the bottle itself. Temperature was measured. The mass of the empty bottle was corrected for the weight of gas in the bottle at atmospheric pressure, m_{g2}. The gas bottle volume was calculated from:

$$V_b = \frac{z_1 m_g R T_1}{p_1 M} \tag{B.12}$$

where the mass of gas in the bottle m_g was found from:

$$m_g = m_{b1} - m_{b2} + m_{g2} \tag{B.13}$$

The weight of the bottle was measured on a balance with accuracy ±0.05 kg. Neglecting the error introduced when calculating the mass of the gas in the bottle at atmospheric pressure m_{g2}, the overall error in m_g was ±0.1 kg. The overall error in the calculated gas bottle volume became:

$$\begin{aligned} \Delta V_b &= \left|\frac{\partial V_b}{\partial z_1} \cdot \Delta z_1\right| + \left|\frac{\partial V_b}{\partial m_g} \cdot \Delta m_g\right| + \left|\frac{\partial V_b}{\partial T_1} \cdot \Delta T_1\right| + \left|\frac{\partial V_b}{\partial p_1} \cdot \Delta p_1\right| \\ &= \frac{z_1 m_g R T_1}{p_1 M}\left[\frac{\Delta z_1}{z_1} + \frac{\Delta m_g}{m_g} + \frac{\Delta T_1}{T_1} + \frac{\Delta p_1}{p_1}\right] \end{aligned} \tag{B.14}$$

Maximum error in z-factor, calculated using the SRK-Peneloux equation of state (PVTsim, 2001), was assumed 2 %. The inaccuracies in the pressure and temperature measurements were the same as in the above calculation of error in gas injection rate.

By weighing the gas bottles, the error in the gas bottle volumes decreased from 5 % to about 3.2 % for methane gas bottles. Unfortunately, for natural gas mixture bottles, the maximum pressure was only about 100 bar resulting in a less accurate calculation of the gas bottle volumes. The error in these bottle volumes was aproximately 4.0 %.

B.2 Error in gas vent rate

The gas vent rate was found by averaging the gas flow rate measurements from VFMg-2D over time. Three different errors were included in the average gas vent rate:

- error in measured gas flow rate from calibration of instrument (Q_{meas})
- error in correction factor for other conditions than calibration conditions (c)
- error when averaging the gas vent rate over time

The error in the calibration was ±0.032 Nl/min (calibration from manufacturer), calculated from the standard deviation multiplied by three. The correction factor was calculated using Flow Calculations (FLUIDAT) (1994). The supplier of FLUIDAT could not give any accuracy for the correction factor, so the error in the correction factor was assumed to be maximum ±2 %. The measured gas vent rate Q_{vent} and the error in measured gas vent rate became:

$$Q_{vent} = Q_{meas} \cdot c$$

$$\Delta Q_{vent} = \left|\frac{\partial Q_{vent}}{\partial Q_{meas}} \cdot \Delta Q_{meas}\right| + \left|\frac{\partial Q_{vent}}{\partial c} \cdot \Delta c\right| = c\Delta Q_{meas} + Q_{meas}\Delta c \tag{B.15}$$

The error introduced when averaging the gas flow rate was found from the standard deviation routine in MS Excel. The standard deviation of the average measured gas vent rate depended on the number of sampled flow rates and was found from (Doebelin, 1990):

$$s_{vent} = \frac{s_{Q_{vent}}}{\sqrt{n_{i,\,vent} - 1}} \tag{B.16}$$

Thus, the overall error in the gas vent rate was the sum of ΔQ_{vent} and s_{vent}.

URN:NBN:no-3342

Appendix C
Calculation of solubility from Henry's law

The mole fraction solubility was calculated using Henry's law. Assuming an infinitely dilute solution where activity approaches unity (Cramer, 1984, Kobayashi and Katz, 1953), Henry's law applied:

$$f_i = Hx_i \tag{C.1}$$

where the fugacity of gas component *i* in the vapor phase is given by

$$f_i = \phi_i y_i p \tag{C.2}$$

where p is the total pressure and y_i is the mole fraction of the component in the vapor phase. The vapor pressure of water is neglected, and hence for a gas mixture, the total pressure was the sum of the partial pressures of the gas mixture components.

The fugacity coefficient ϕ_i was predicted using the SRK equation of state. A modified version of the computer program SRKH&S.f by Sloan (1998) including equation A.3 in Sloan's book (1998) for the fugacity coefficient was applied for the calculation. Given the type of gas, its mole fraction, pressure and temperature, the program calculated the fugacity coefficient for that gas. For a gas mixture of methane, ethane and propane, fugacity coefficients for each of the three components were calculated. Mixing rules were included in the program,

URN:NBN:no-3342

however, for the mixture of methane, ethane and propane, the binary interaction parameters were set to zero (Sloan, 1998).

Henry’s law constants for methane and ethane were found in Perry’s Chemical Engineer’s Handbook (Perry and Green, 1984), where values of Henry’s law constants are tabulated for temperatures from 0 to 100 °C. Tabulated values from 0 to 40 °C were used to correlate Henry’s law constants to temperature (Figure C.1 a, b). Similarly, Henry’s law constants reported by Kobayashi and Katz (1953) were used for propane (Figure C.1 c).

Himmelblau (1960) has reported that each gaseous component in nitrogen-oxygen and nitrogen-hydrogen mixtures acts independently of the others in the pressure

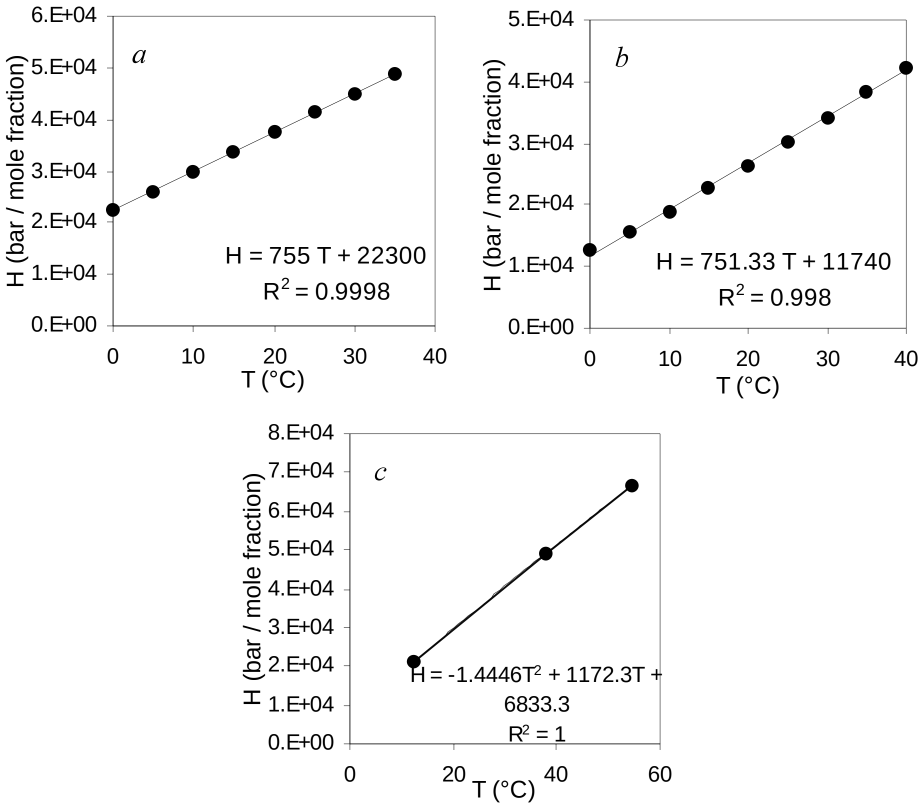

Figure C.1 Henry’s law constants for methane (a) and ethane (b) solubility in water (Perry and Green, 1984) and propane (c) solubility in water (Kobayashi and Katz, 1953).

range where Henry’s law holds. Based on this finding and that the interaction parameters between the three components were zero, it was assumed that the solubility of a mixture of methane, ethane and propane could be calculated as the weighed sum of the components’ solubilities:

$$x_{\text{mixture}} = \sum_{i=1}^{n} y_i x_i \tag{C.3}$$

The solubility of component *i* was found from Equation C.1, and the fugacity of the component in the mixture was found from Equation C.2.

Appendix D
Mass- and energy balance

The reactor can be modeled as a continuous stirred tank reactor (CSTR) by assuming that the reactor operates at perfectly mixed conditions. The characteristic of a CSTR is that the conditions in the outlet stream are equal to the conditions in the reactor. Mass and heat are perfectly distributed in the reactor volume by the impeller.

In the present reactor, water was pumped into the reactor near the bottom while the gas was injected through two non-return valves at the bottom. Hydrates were formed and a mixture of hydrates, water and gas flowed out near the top of the reactor. In the reactor, pressure and temperature were measured continuously, thus giving the conditions of the outlet flow of the reactor. The reactor was situated in a temperature controlled room meaning that little or no heat was exchanged with the surroundings. Heat of hydrate formation was removed in a heat exchanger downstream the reactor and the separator.

The purpose of establishing the mass- and energy balance for the reactor is to investigate if the simulated results correspond with the measurements. Also, such balances are useful for calculation of reactor volume and cooling requirement. The development of the following mass- and energy balance is based on the book by Fogler (1999).

URN:NBN:no-3342

D.1 Mass balance

The general mole balance for a component *i* in a reactor of volume *V* is given by:

$$F_{i0} - F_i + \int_V r_i dV = \frac{dn_i}{dt} \tag{D.1}$$

where F_{i0} and F_i are the molar flow rates of component *i* in and out of the reactor, respectively, and n_i is the number of moles of *i* in the reactor. Assuming a perfectly mixed reactor operated at steady-state conditions, such as the CSTR, the mole balance develops into the design equation for a CSTR:

$$V = \frac{F_{i0} - F_i}{(-r_i)_{out}} = \frac{F_{i0}X}{(-r_i)_{out}} \tag{D.2}$$

where $(-r_i)_{out}$ is the rate of reaction with respect to the reacting component *i* evaluated at the outlet conditions, and *X* is the conversion of component *i*.

For the present reactor, the reaction rate with respect to the gas phase was given by the bubble-to-crystal model in Equation 8.6 and the converged values in Table 8.2. The conversion *X* was indicated by the gas consumption rate in proportion to the gas injection rate, which for methane gas at 70 bar was given by the slope of Equation 5.1. The slope for methane gas at 90 bar was 0.562 (Equation 5.2). Based on the experimental conditions for several experiments, reactor volumes were calculated (Table D.1). Note that the reactor volumes were found by solving Equation D.2 and the model Equation 8.6 simultaneously since the reactor volume was also included in Equation 8.6. The reactor volumes should preferably be close to 9.5 litre, however, since the bubble-to-crystal model calculated the rates of hydrate formation within 30 % (Figure 8.8), ±30 % deviation from the actual reactor volume was expected.

The design equation may be used, with caution, for determination of the reactor volume at process plant conditions by assuming that the bubble-to-crystal model holds for the chosen conditions. For example, given a superficial gas velocity of 0.05 m/s, which is recommended for industrial reactors (Cropper, 1998), assuming

Table D.1. Calculated reactor volumes based on Equation D.2.

Experi -ment	Pressure (bar)	Superficial gas velocity (m/s)	Gassed power consumption (W)	Conver -sion (-)	**Reactor volume (m^3)**	Dev. from 9.5 l (%)
6a	70	$1.38 \cdot 10^{-3}$	3.20	0.443	**0.0119**	25
7a	70	$2.37 \cdot 10^{-3}$	2.80	0.443	**0.0133**	40
13a	90	$1.48 \cdot 10^{-3}$	3.16	0.562	**0.0113**	19
19a	90	$0.310 \cdot 10^{-3}$	29.5	0.562	**0.00670**	29
5[a]	70	$0.255 \cdot 10^{-3}$	3.65	0.443	**0.00877**	7.7

---

[a] Parlaktuna and Gudmundsson (1998b)

Table D.2. Example of prediction of reactor volume

Parameter	Value
Superficial gas velocity	0.05 m/s
Pressure	90 bar
Temperature	7 °C
Stirring rate	800 RPM
Gassed power consumption	6.76 W
Concentration driving force	17.53 mol/m^3
Gas consumption rate $(-r_i)_{out}$	309.9 mol/m^3s
Molar flow rate F_{i0}	5.80 mol/s
Conversion X	0.562
Reactor volume V	**0.00387 m^3**

that a stirring rate of 800 RPM was sufficient to efficiently disperse the gas, and assuming a pressure of 90 bar and a temperature of 7°C, the resulting reactor volume became 3.9 litre. The calculated parameters are given in Table D.2. Increasing the superficial gas velocity by one to two orders of magnitude gave about 50 % reduction in the reactor volume and an increase in hydrate formation rate of about two orders of magnitude compared to the experimental conditions in Table D.1. Since both the gas consumption rate r_i and the molar gas injection rate F_{i0} were proportional to the superficial gas velocity (Equation D.2), the superficial gas velocity mainly influenced the gassed power consumption in the gas consumption rate term.

D.2 Energy balance

The unsteady-state energy balance for an open system, illustrated in Figure D.1, that has n components entering and leaving at its respective molar flow rates F_i and with respective energy E_i is:

$$\frac{dE_{sys}}{dt} = \dot{Q} - \dot{W} + \sum_{i=1}^{n} F_i E_i \big|_{in} - \sum_{i=1}^{n} F_i E_i \big|_{out} \tag{D.3}$$

where $\dot{Q}$ is the heat flow to the system and $\dot{W}$ is the work done by the system. The energy term E_i consists of internal, kinetic and potential energy where the internal energy is dominating. Separating the work term into shaft work and flow work, and combining the flow work term with the internal energy, the following energy balance emerges:

$$\frac{dE_{sys}}{dt} = \dot{Q} - \dot{W}_s + \sum_{i=1}^{n} F_{i0} H_{i0} - \sum_{i=1}^{n} F_i H_i \tag{D.4}$$

where H_i is the enthalpy of the stream and the subscript “0” represents the inlet conditions. The formation of gas hydrates can be considered as:

$$C_{(g)} + n_h H_2O_{(l)} \rightarrow C \cdot n_h H_2O_{(s)} \tag{D.5}$$

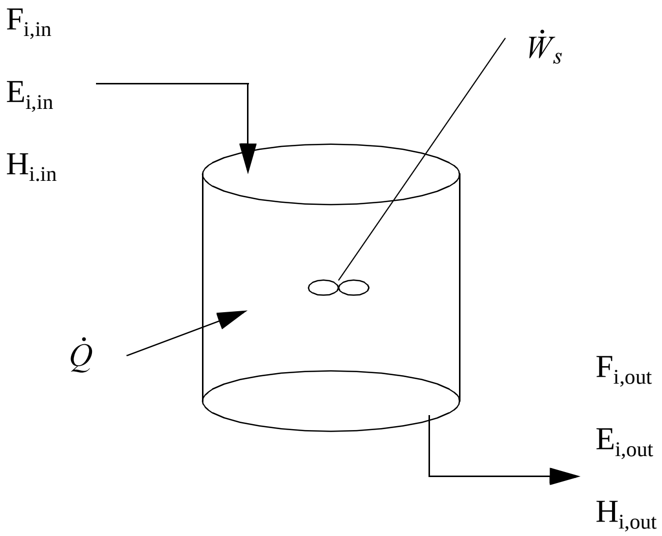

Figure D.1 Schematic energy balance for an open system

where C is the gas molecule and n_h is the hydration number. For the hydrate formation process, the enthalpy terms are written out as follows:

$$\begin{aligned} \sum H_{i0}F_{i0} &= H_{g0}F_{g0} + H_{w0}F_{w0} \\ \sum H_i F_i &= H_h F_h + H_g F_g + H_w F_w \end{aligned} \qquad \text{(D.6)}$$

where g, w and h refer to the gas, water and hydrate phases, respectively. With respect to the inlet molar flow rate of gas, the outlet flow rates of gas, water and hydrate are:

$$\begin{aligned} F_g &= F_{g0}(1-X) \\ F_w &= F_{g0}\left(\frac{F_{w0}}{F_{g0}} - n_h X\right) \\ F_h &= F_{g0}\left(\frac{F_{h0}}{F_{g0}} + X\right) = F_{g0}X \end{aligned} \qquad \text{(D.7)}$$

The enthalpy terms in Equation D.6 become:

$$\begin{aligned}\sum H_{i0}F_{i0} - \sum H_i F_i &= F_{g0}\left[(H_{g0}-H_g) + \frac{F_{w0}}{F_{g0}}(H_{w0}-H_w)\right] \\ &\quad -(H_h - nH_w - H_g)F_{g0}X \qquad \text{(D.8)} \\ &= F_{g0}\left[(H_{g0}-H_g) + \frac{F_{w0}}{F_{g0}}(H_{w0}-H_w)\right] - \Delta H_{Rx}F_{g0}X\end{aligned}$$

where ΔH_{Rx} is the enthalpy (heat) of formation at the outlet temperature. Assuming a limited temperature change from inlet to outlet, meaning constant heat capacities and no phase change, the energy balance for a hydrate producing CSTR becomes:

$$\begin{aligned}\frac{dE_{sys}}{dt} &= \dot{Q} - \dot{W}_s - F_{g0}\left[c_{pg}(T-T_{g0}) + \frac{F_{w0}}{F_{g0}}c_{pw}(T-T_{w0})\right] \qquad \text{(D.9)} \\ &\quad -\Delta H_{Rx}F_{g0}X\end{aligned}$$

where c_{pg} and c_{pw} are the heat capacities of gas and water, respectively, T is the reactor temperature and T_{g0} and T_{w0} are the inlet gas and water temperatures, respectively.

The CSTR was considered to operate at steady-state conditions. The reactor was situated in a temperature controlled room, and a reasonable assumption was therefore that the reactor operated adiabatically. Thus, using the energy balance in Equation D.9, the outlet temperature of the reactor was determined by the enthalpy of formation, the shaft work and the specific heat capacities and the inlet temperatures of the flow rates of gas and water:

$$T = \frac{F_{g0}\,c_{pg}T_{g0} + F_{w0}\,c_{pw}T_{w0} - \dot{W}_s - \Delta H_{Rx}F_{g0}X}{F_{g0}c_{pg} + F_{w0}c_{pw}} \qquad \text{(D.10)}$$

The shaft work term was defined as work done by the system on the surroundings and the enthalpy of formation term was negative because hydrate formation is an exothermic process.

In the following, the specific heat capacities and the enthalpy of formation of methane and natural gas mixture hydrates are determined. Two examples are given where calculated outlet temperatures are compared with measured outlet temperatures when the shaft work, the molar flow rates and the conversion are found from the experimental data.

Specific heat capacities. The specific heat capacities of methane gas and natural gas mixture were found using PVTsim 11.0 (2001). The specific heat capacity of water at 1 bar in the range 0-20 °C is given in Table D.3.

Table D.3. Specific heat capacity of water at 1 bar (Lide, 1990).

T (°C)	0	10	20
c_p ($\mathrm{Jmol^{-1}K^{-1}}$)	76.0	75.5	75.4

Enthalpies of formation. In the literature, enthalpies of dissociation have been measured and correlated. The enthalpy of formation used in the present calculations is based on the enthalpy of dissociation. Levik (2000) reviewed models and correlations for the dissociation enthalpy of methane and natural gas hydrates and pointed out the lack of experimental data for natural gas hydrate.

Holder, Zetts and Pradhan (1988) developed a correlation based on literature data for the enthalpy of dissociation for different hydrates of pure components. For methane, the proposed correlation is:

$$\Delta H_{diss} = 4.18(13500 - 4T) \tag{D.11}$$

for temperatures from 0 to 25 °C. Note that the correlation yields the enthalpy of dissociation at the hydrate equilibrium pressure and that the temperature must be in Kelvin.

Maximov (1996) reviewed several Russian studies and reported measurements of the enthalpies of dissociation for natural gas hydrates. Handa (1986) measured the dissociation enthalpy of methane, ethane, propane and isobutane hydrates by calorimetry.

Levik (2000) described how the enthalpy of dissociation can be found by using the Clausius-Clapeyron equation. For the natural gas mixture used in the present work, he calculated the enthalpy of dissociation around 1 atm to be 73.0 kJ/mol. He compared different results for methane and natural gas hydrates, and found that the Clausius-Clapeyron equation overestimates the enthalpy of dissociation

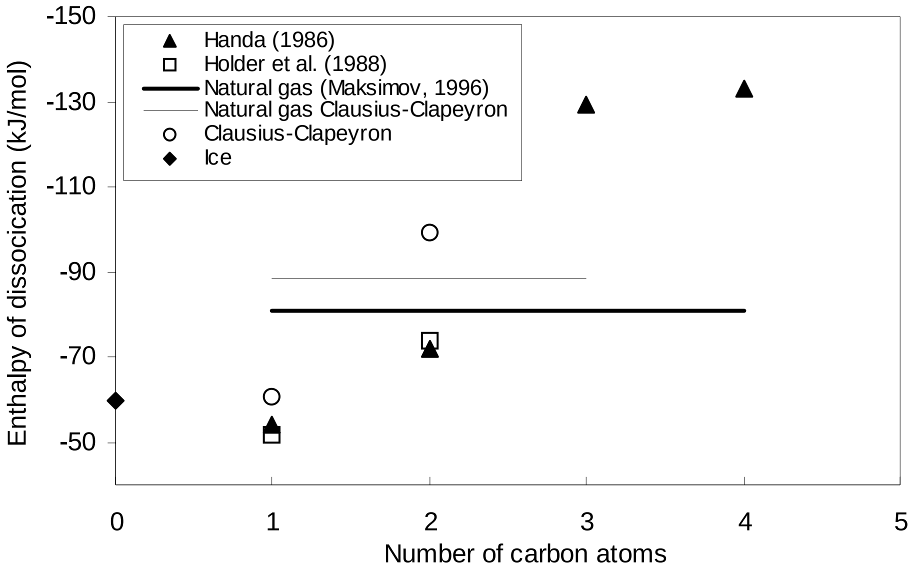

Figure D.2 Enthalpy of dissociation for ice (0), methane (1), ethane (2), propane (3), isobutane (4) and two natural gases.

compared to the correlation of Holder *et al.* (1988) and underestimates the enthalpy of dissociation compared to the calorimetric measurements by Handa (1986).

Dissociation enthalpies of hydrates from natural gas components are compared in Figure D.2. Handa's results were reported at 0 °C and 1 atm. Enthalpies of dissociation of methane and ethane hydrates from the correlation of Holder *et al.* were calculated for 70 bar. Hydrate equilibrium temperatures of 10.1 and 16.5 °C (CSMhyd, 1998) for methane and ethane hydrates, respectively, were used. Maksimov reported the enthalpy of dissociation for a natural gas hydrate containing methane, ethane, propane, isobutane, oxygen and nitrogen. The enthalpy of dissociation in Figure D.2 is at 0 °C and 11 bar. The enthalpy of dissociation of ice was taken from steam tables (Moran and Shapiro, 1993).

Using the Clausius-Clapeyron equation with a correction for non-ideal gas, the dissociation enthalpy for natural gas mixture hydrates was calculated at 70 bar from:

$$\Delta H_{diss} = -zsR \qquad \text{(D.12)}$$

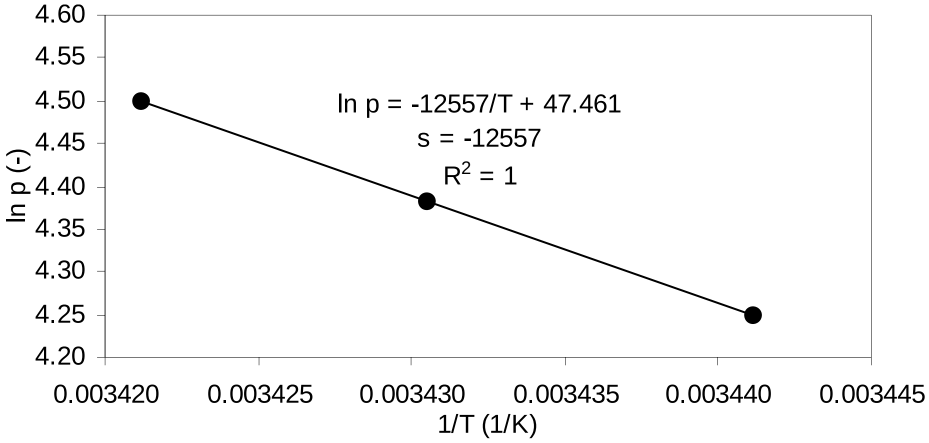

Figure D.3 Clausius-Clapeyron plot for hydrate equilibrium from 70 to 90 bar. The hydrate equilibrium data for the natural gas mixture were obtained from CSMhyd (1998).

where s is the slope of a straight line plot of $\ln p$ versus $1/T$, z is the z-factor in real gas law and R is the universal gas constant. The plot for the natural gas mixture in the 70 to 90 bar range is shown in Figure D.3. The plot indicated that the dissociation enthalpy was a weak function of pressure so that the slope could be used for calculation of the enthalpy of dissociation in the selected pressure range. Comparing this slope with the slope reported by Levik (2000) at around 1 atm, it is seen that the slope increased with pressure. As the slope increased, the dependence of the temperature became less significant. This means that the enthalpy of dissociation was also a weak function of temperature at the present conditions. The calculated dissociation enthalpy is compared with the literature data in Figure D.2 (Natural gas Clausius-Clapeyron).

The dissociation enthalpies for methane and ethane hydrates were also found using the Clausius-Clapeyron method (Clausius-Clapeyron data in Figure D.2). The equilibrium data for methane and ethane from 70 to 90 bar were calculated using CSMhyd (1998). Similar calculations of the dissociation enthalpies for propane and isobutane hydrates gave high dissociation enthalpies that were considered unrealistic compared to the experimental results by Handa (1986).

The comparison in Figure D.2 shows that the enthalpy of dissociation increases (in negative sign) with the number of carbon atoms in the gas molecule. Also, the enthalpy of dissociation shifts to a higher level between ethane and propane, that is, between sI and sII hydrates. The enthalpies from the Clausius-Clapeyron method diverge from the enthalpies measured by Handa (1986), however, the enthalpies from the Clausius-Clapeyron method were for a higher pressure. Maksimov (1996) reported that the enthalpy of dissociation depends on the temperature and the pressure. In Figure D.2, the two enthalpies for natural gas hydrates have different compositions and are measured and calculated at different conditions. Summarized, there is a considerably discrepancy between measurements at standard conditions and predictions by Clausius-Clapeyron at elevated pressures. The discrepancy may be due to the difference in pressure, however, this is not confirmed by any measurements. Levik (2000) found that the deviations for natural gas hydrates between measurements reported by Maximov and predictions using the Clausius-Clapeyron method, were up to 17 %. In prediction of the heat of formation in the energy balance, considerably inaccuracy must be expected.

The heat of formation can be calculated in terms of kJ/kg by assuming a hydration number (Section 2.1) and applying the molar mass of the feed gas. Assuming that 150 Sm^3 gas forms 1 m^3 hydrate, the hydration number for both methane and natural gas mixture hydrate is approximately 7. The molar mass of methane gas is 16.04 g/mol. Assuming that fractionation is suppressed by producing at high subcooling, so that the composition is similar to the feed gas composition (Levik, 2000), the molar mass of natural gas mixture is close to 17.58 g/mol. To obtain the heat of formation in terms of kJ/kg, the enthalphy of dissociation (J/mol) is multiplied with $1/(M_g + 18.02n_h)$ where M_g is the molar mass of the gas and n_h is the hydration number (Levik, 2000). It should be noted that the driving force has an impact on the heat of formation in terms of kJ/kg through the molar mass and the hydration number.

Example 1. The reactor outlet temperature in experiment 1a was simulated using the energy balance (Equation D.10). The experimental conditions are listed in Table D.4. Derived molar flow rates, heat capacities and enthalpy of formation are given in Table D.5.

Table D.4. Experimental conditions in experiment 1a.

Parameter	Value
Pressure p	70 bar
Reactor temperature T	7.1 °C
Hydrate equilibrium temperature T_{eq}	10.1 °C
Power consumption P_g	-3.209 W
Superficial gas velocity v_{sg}	$1.35 \cdot 10^{-3}$ m/s
Liquid flow rate	20 litre/min
z-factor (PVTsim 11.0, 2001)	0.861
Conversion X (from Equation 5.1)	0.443

Table D.5. Derived parameters for Equation D.10.

Parameter	Value
F_{g0}	0.1178 mol/s
F_{w0}	18.50 mol/s
c_{pg} (PVTsim 11.0, 2001)	49.39 J/molK
c_{pw} (interpolation from Table D.3)	75.65 J/molK
ΔH_{Rx} (Equation D.11 with T=10.1 °C)	-51694.1 J/mol

For the present conditions, Equation D.10 became:

$$T = \frac{5.817\, T_{g0} + 1399.53 T_{w0} + 3.209 + 2697.17}{1405.19} \tag{D.13}$$

The inlet gas and water temperatures were found from the experimental data shown in Figure D.4. The inlet gas temperature was measured with sensor Tg-1D and the inlet water temperature with sensor Tw-7D. For the time interval from 238 to 440 seconds, the average inlet gas temperature T_{g0} was 5.178 °C and the average inlet water temperature T_{w0} was 6.365 °C. Using Equation D.13, the

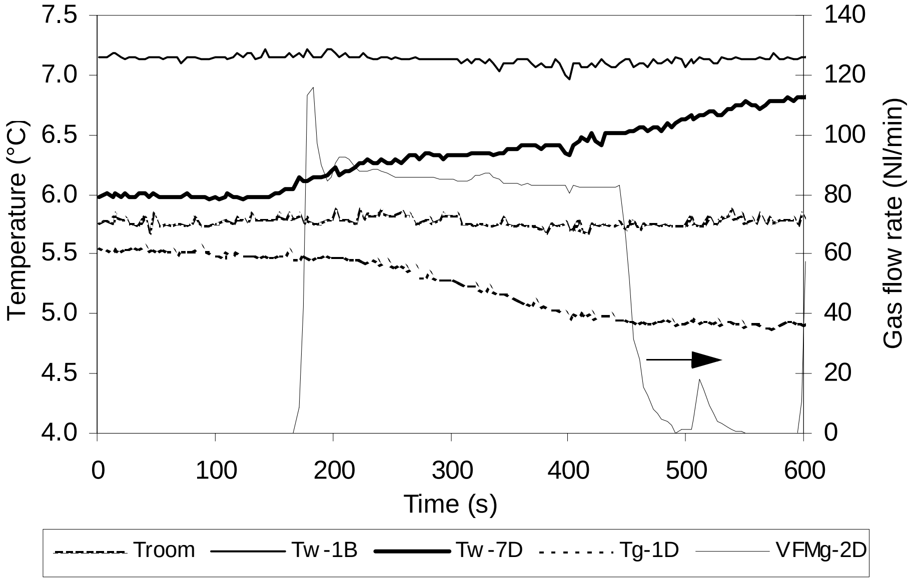

Figure D.4 Temperature profiles and gas vent rate in experiment 1a. Tw-1B is the reactor temperature, Tw-7D is the reactor inlet temperature, Tg-1D is the gas inlet temperature and Troom is the ambient temperature. The experimental flow rates were averaged between 238 and 440 seconds, VFMg-2D gives an indication of the time interval where steady-state operation was emphasized.

calculated reactor outlet temperature became 8.31 °C. According to the definition of a CSTR, the outlet temperature is considered equal to the reactor temperature, Tw-1B. The measured average reactor temperature, Tw-1B, was 7.10 °C, which was 1.21 °C lower than calculated.

This example shows that only a slight increase in temperature should be expected, which was also confirmed by the experimental data. This means that most of the heat released during hydrate formation, the enthalpy of formation, was consumed as sensible heat in the liquid phase. According to Equation D.13, the energy supplied from the impeller was insignificant compared to the heat of formation.

According to the steady-state adiabatic energy balance, the predicted outlet temperature was higher than the measured outlet temperature. A cooling rate at about 1700 W, which would have required a very high heat transfer coefficient, had to be applied to obtain an outlet temperature at about 7.10 °C. Thus, it is more

URN:NBN:no-3342

likely that the discrepancy was caused by errors in the temperature measurements, in which the energy balance is sensitive to.

Example 2. Also, the energy balance was applied to experiment 5b using the same procedure as described in Example 1. The Clausius-Clapeyron method in Equation D.12 was used to predict the enthalpy of formation for the natural gas mixture at the experimental pressure. The predicted outlet temperature was 15.46 °C while the measured reactor temperature was 14.44 °C. The liquid inlet temperature was 13.21 °C.

Appendix E
Publications

- Mork, M. and Gudmundsson, J.S., Hydrate formation rate in a continuous stirred tank reactor: experimental results and bubble-to-crystal model, *Proceedings of The Fourth International Conference on Gas Hydrates*, Yokohama, Japan, May 19-23, 2002.
- Gudmundsson, J.S., Mork, M. and Graff, O.F., Hydrate non-pipeline technology, *Proceedings of The Fourth International Conference on Gas Hydrates*, Yokohama, Japan, May 19-23, 2002.
- Mork, M. and Gudmundsson, J.S., Rate of hydrate formation, experimental results and empirical correlation, *13th International Oil Field Chemistry Symposium*, Geilo, Norway, March 17-20, 2002.
- Mork, M., Gudmundsson, J.S. and Parlaktuna, M., Hydrate formation rate in a continuous stirred tank reactor, *2001 International Gas Research Conference*, Amsterdam, the Netherlands, November 5-8, 2001.
- Gudmundsson, J.S. and Mork, M., Stranded gas to hydrate for storage and transport, *2001 International Gas Research Conference*, Amsterdam, the Netherlands, November 5-8, 2001.
- Mork, M. and Gudmundsson, J.S., Rate of hydrate formation in subsea pipelines, correlation based on reactor experiments, *12th International Oil Field Chemistry Symposium*, Geilo, Norway, April 1-4, 2001.

URN:NBN:no-3342

- Mork, M., *Stirred tank reactors, Overview of basic concepts*, Technical report, Department of Petroleum Engineering and Applied Geophysics, NTNU, 78 pp., December, 2000.
- Gudmundsson, J.S., Andersson, V., Levik, O.I., Mork, M., Hydrate technology for capturing stranded gas, *Annals of the New York Academy of Sciences*, **912**, 403-410, 2000.
- Mork, M., *Hydrate formation, Literature study of the kinetics of nucleation and growth*, Technical report, Department of Petroleum Engineering and Applied Geophysics, NTNU, 19 pp., April, 2000.
- Mork, M., *Crude oil properties, Study of crude oils for transport at low temperature*, Technical report, Department of Petroleum Engineering and Applied Geophysics, NTNU, 37 pp., December, 1999.
- Gudmundsson, J.S., Andersson, V., Durgut, I., Levik, O.I., Mork, M., NGH on FPSO - slurry process and cost estimate, *SPE Annual Technical Conference and Exhibition*, SPE paper 56629, Houston, USA, October 3-6, 1999.

URN:NBN:no-3342